

## *r*-Process Radioisotopes from Near-Earth Supernovae and Kilonovae

XILU WANG,<sup>1,2,3</sup> ADAM M. CLARK,<sup>2</sup> JOHN ELLIS,<sup>4,5</sup> ADRIENNE F. ERTEL,<sup>6,7</sup> BRIAN D. FIELDS,<sup>6,8,7</sup> ZHENGHAI LIU,<sup>6,7</sup>  
JESSE A. MILLER,<sup>6,7</sup> AND REBECCA SURMAN<sup>2,3</sup>

<sup>1</sup>*Department of Physics, University of California, Berkeley, CA 94720, USA*

<sup>2</sup>*Department of Physics, University of Notre Dame, Notre Dame, IN 46556, USA*

<sup>3</sup>*N3A3 Collaboration*

<sup>4</sup>*Theoretical Physics and Cosmology Group, Department of Physics, King's College London, London WC2R 2LS, UK*

<sup>5</sup>*NICPB, R vala pst. 10, 10143 Tallinn, Estonia; Theoretical Physics Department, CERN, CH-1211 Geneva 23, Switzerland*

<sup>6</sup>*Department of Astronomy, University of Illinois, Urbana, IL 61801, USA*

<sup>7</sup>*Illinois Center for the Advanced Study of the Universe, University of Illinois, Urbana IL 61820*

<sup>8</sup>*Department of Physics, University of Illinois, Urbana, IL 61801, USA*

### ABSTRACT

The astrophysical sites where *r*-process elements are synthesized remain mysterious: it is clear that neutron-star mergers (kilonovae, KNe) contribute, and some classes of core-collapse supernovae (SNe) are also likely sources of at least the lighter *r*-process species. The discovery of the live isotope <sup>60</sup>Fe on the Earth and Moon implies that one or more astrophysical explosions occurred near the Earth within the last few Myr, probably a SN. Intriguingly, several groups have reported evidence for deposits of <sup>244</sup>Pu, some overlapping with the <sup>60</sup>Fe pulse. However, the putative <sup>244</sup>Pu flux appears to extend to at least 12 Myr ago, pointing to a different origin. Motivated by this observation, we propose that ejecta from a KN enriched the giant molecular cloud that gave rise to the Local Bubble in which the Sun resides. Accelerator Mass Spectrometry (AMS) measurements of <sup>244</sup>Pu and searches for other live isotopes could probe the origins of the *r*-process and the history of the solar neighborhood, including triggers for mass extinctions, e.g., at the end of the Devonian epoch, motivating the calculations of the abundances of live *r*-process radioisotopes produced in SNe and KNe that we present here. Given the presence of <sup>244</sup>Pu, other *r*-process species such as <sup>93</sup>Zr, <sup>107</sup>Pd, <sup>129</sup>I, <sup>135</sup>Cs, <sup>182</sup>Hf, <sup>236</sup>U, <sup>237</sup>Np and <sup>247</sup>Cm should be present. Their abundances could distinguish between SN and KN scenarios, and we discuss prospects for their detection in deep-ocean deposits and the lunar regolith. We show that AMS <sup>129</sup>I measurements in Fe-Mn crusts already constrain a possible nearby KN scenario.

KCL-PH-TH/2021-03, CERN-TH-2021-014, N3AS-21-007

*Keywords:* Kilonovae; Supernovae; Nucleosynthesis; *r*-Process; Nuclear Abundances; Accelerator Mass Spectrometry

### 1. INTRODUCTION

Astrophysical explosions such as supernovae (SNe) within  $\mathcal{O}(10)$  pc would be close enough to endanger life on Earth (Ruderman 1974; Ellis & Schramm 1995), and SN explosions within  $\mathcal{O}(100)$  pc would have been close enough to deposit detectable amounts of live (undecayed) radioactive isotopes (Ellis et al. 1996). Over the past two decades, many experiments have detected live <sup>60</sup>Fe in deep-ocean sediments and ferromanganese (Fe-Mn) crusts (Knie et al. 1999, 2004; Fitoussi et al. 2008; Wallner et al. 2016; Ludwig et al. 2016; Wallner et al. 2020), in the lunar regolith (Fimiani et al. 2016), in cosmic rays (Binns et al. 2016) and in Antarctic snow (Koll et al. 2019). The <sup>60</sup>Fe is best understood as evidence for explosion of one or more nearby and recent SNe, and the deep-ocean data point to an epoch  $\sim 3$  Myr ago (Mya) and distance  $\lesssim 120$  pc away (Fields & Ellis 1999; Fields et al. 2005; Fry et al. 2015). This interpretation

is supported by recent evidence for  $^{53}\text{Mn}$  in Fe-Mn crusts (Korschinek et al. 2020). The wealth and variety of  $^{60}\text{Fe}$  detections establish that near-Earth explosions indeed occurred in the geological past. These results bring home the environmental hazards facing citizens of star-forming galaxies such as ours.

Intriguingly, there also have been several reports of non-anthropogenic  $^{244}\text{Pu}$  in deep-ocean deposits during the past 25 Myr (Paul et al. 2001; Wallner et al. 2004; Raisbeck et al. 2007; Wallner et al. 2015), which are of particular interest because  $^{244}\text{Pu}$  originates in the astrophysical  $r$ -process. While the  $^{244}\text{Pu}$  detections are tentative, it is worthwhile to consider the profound implications if they are real and represent injection from an extrasolar explosion. Therefore, in this paper we study potential near-Earth  $r$ -process events: their astrophysical sources, means of delivery to Earth, and radioisotope signatures. On the other hand, we also discuss the implications if the  $^{244}\text{Pu}$  indications are not confirmed in future work.

The most important sites for the  $r$ -process are currently a subject of debate (Cowan et al. 2021). Certainly neutron star mergers (kilonovae, KNe) sites are inevitable sites, and the recent observation of a KN associated with the GW190521 gravitational-wave signal (Abbott et al. 2017a,b) suggests encouraging prospects for more detailed studies of similar events in the future (Zhu et al. 2018, 2021; Barnes et al. 2020; Korobkin et al. 2020; Wang et al. 2020b). However, neutron-star mergers may be only partially responsible for the Galactic tally of  $r$ -process elements (Côté et al. 2019; Kobayashi et al. 2020; Yamazaki et al. 2021), and a variety of other sites have been proposed, including both standard and rare types of core-collapse SNe, see, e.g., Hoffman et al. (1997); Wanajo (2006); Fujimoto et al. (2008); Winteler et al. (2012); Mösta et al. (2018a); Siegel et al. (2019); Miller et al. (2020); Choplin et al. (2020); Reichert et al. (2021); Fujimoto & Nagakura (2021). The radioisotopes produced by various  $r$ -process sites have also been studied: see, e.g., early work by Seeger & Schramm (1970) and Blake & Schramm (1973); Meyer (1993) on pre-solar abundances; Goriely & Janka (2016) on SN neutrino driven winds;  $^{244}\text{Pu}$  yields and ratios in Tsujimoto et al. (2017); and recent work by Beniamini & Hotokezaka (2020) and Côté et al. (2021).

We have therefore been motivated to calculate the possible yields of other  $r$ -process nuclei in both SN and KN sites and compare their abundances relative to  $^{244}\text{Pu}$ . These may be measurable in both deep-ocean deposits and the lunar regolith, where  $^{60}\text{Fe}$  has already been detected (Fimiani et al. 2016). Layers of age  $\sim 2.5$  Myr where there is a peak in the deep-ocean  $^{60}\text{Fe}$  signal are of particular interest, as discovery of one or more  $r$ -process isotopes there would confirm that at least one SN was an  $r$ -process site. However, other layers are also of interest, particularly because there is evidence for deep-ocean  $^{244}\text{Pu}$  atoms deposited outside the  $^{60}\text{Fe}$  peak, which points to one or more other sources of unknown astrophysical origin. Another motivation is the possibility that one or more other astrophysical explosions may have occurred at closer distances in the more distant past. Specifically, it has been suggested (Fields et al. 2020) that one of more extinction events towards the end of the Devonian  $\sim 360$  Mya might have been caused by SN explosions. These events probably occurred too long ago to have left detectable deposits of  $^{60}\text{Fe}$ , in view of its relatively short half-life  $\sim 2.5$  Myr, but might have left detectable deposits of longer-lived  $r$ -process isotopes such as  $^{244}\text{Pu}$  (half-life 80 Myr).

In order to lay a basis for a systematic study of possible live isotope studies of possible nearby astrophysical explosions and  $r$ -process sites, we survey all the nuclear isotopes with half-lives between 1 Myr and 1 Gyr, identifying the nucleosynthesis processes that might produce them and commenting on the results of previous searches on the Earth and Moon and the prospects for their future detection.

Three timescales are of particular interest. First, the widespread detection of live  $^{60}\text{Fe}$  shows that at least one nearby supernova injected  $^{60}\text{Fe}$  into the interstellar medium at a time

$$t_{\text{Plio}} \simeq 3.2 \text{ Mya}, \quad (1)$$

as derived from the sediment data of Wallner et al. (2016) and Ludwig et al. (2016), where core 4953 of Wallner et al. (2016) is the earliest  $^{60}\text{Fe}$  detection. The peak of the  $^{60}\text{Fe}$  deposition on Earth due to this event was  $\sim 2.5$  Mya, around the end of the Pliocene epoch, and a linkage to a coincident mass extinction has been proposed in Melott et al. (2019). We note also that the ferromanganese crust data from Wallner et al. (2016) provides evidence of a potential second peak at about 7 Mya that has yet to be confirmed in sediment data or in other studies.

Secondly, geological indications of live  $^{244}\text{Pu}$  imply a flux on Earth that stretches farther back, with the earliest detection in a layer 10–25 Mya. It is thus of interest to consider an event at least this long ago. We will see in Section 5.6 that existing  $^{244}\text{Pu}$  and  $^{129}\text{I}$  data suggest a timescale of

$$t_{\text{KN}} = \mathcal{O}(50) \text{ Mya} \quad (2)$$

for this event.

Finally, [Marshall et al. \(2020\)](#) have recently found evidence of a dramatic loss of stratospheric ozone 359 Myr ago in the so-called Hangenberg crisis, the last of several poorly understood mass extinction events that punctuated the end of the Devonian period. This raises the possibility that one or more nearby supernovae were responsible for the Hangenberg event and possibly others as well ([Fields et al. 2020](#)), roughly at

$$t_{\text{Devo}} \simeq 360 \text{ Mya} . \quad (3)$$

We highlight in the following the yields and isotope ratios at these epochs. We note also that other extinction events may be connected to astrophysical explosions. For example, [Melott et al. \(2004\)](#) have suggested a gamma-ray burst origin for the late Ordovician mass extinction  $\sim 440$  Myr ago.

The layout of our paper is as follows. In Section 2 we survey the radioisotopes with half-lives between 1 Myr and 5 Gyr that are candidates to provide interesting signatures of nearby astrophysical explosions due to SNe and/or KNe. In Section 3, we describe how we estimate the possible yields of these radioisotopes using several models of the *r*-process in SNe and KNe that fit the data on isotope abundances of representative metal-poor stars and also match solar abundances. Then, in Section 4 we present detailed calculations of the ratios of abundances of live isotopes and their time evolution in these models. In light of these results, we discuss in Section 5 the observability of *r*-process isotopes in deep-ocean sediments and crusts and on the Moon. Finally, in Section 6 we discuss the prospects for terrestrial and lunar searches for live isotopes, and how they might cast light on *r*-process sites and the history of the solar neighborhood, and we summarize our conclusions and suggest directions for future work in Section 7.

## 2. A SURVEY OF RADIOISOTOPE SIGNATURES OF ASTROPHYSICAL EXPLOSIONS

A SN or KN within  $\mathcal{O}(10)$  pc would be near enough to pose a threat to life on Earth. Fortunately, however, SN explosions within  $\mathcal{O}(10)$  pc of Earth are expected to occur only on intervals of a billion years or so, and nearby KN explosions are thought to be even rarer. However, SNe are estimated to occur within  $\mathcal{O}(100)$  pc every few million years, and it was suggested in [Ellis et al. \(1996\)](#) that live radioisotopes would be the premier signatures of such events. The detection of such signatures can cast light on the history of the local Galactic bubble and SN nucleosynthesis mechanisms, refine estimates of the SN threat to life on Earth and possibly serve as markers of past SN effects on the biosphere.

Consider an explosion at distance  $r$  and time  $t$  in the past. If the explosion is isotropic, the time-integrated flux, i.e., the fluence, of radioisotope  $i$  at the Sun's interstellar location is

$$\mathcal{F}_i^{\text{interstellar}} = f_i \frac{M_{\text{ej},i}/A_i m_u}{4\pi r^2} e^{-t/\tau_i} \quad (4)$$

where the radioactive decay factor includes all decay in the interval  $t$  between the explosion to the present time  $t$ , i.e., including both travel time and the duration since arrival. Here the isotope mass number is  $A_i$ , its mean life is  $\tau_i$ , and  $m_u \approx m_p$  is the atomic mass unit. Also  $M_{\text{ej},i}$  is the yield at the time of the explosion, i.e., the total mass of isotope  $i$  ejected, the total mass of isotopes ejected at explosion time is  $M_{\text{ej}} = \sum_i M_{\text{ej},i}$ , and  $f_i \leq 1$  is the fraction of atoms of  $i$  that are incorporated into dust particles that arrive at Earth ([Athanassiadou & Fields 2011](#); [Fry et al. 2016](#)).

After fallout onto the Earth and accumulation into natural archives such as deep-ocean sediments and crusts, the present-day surface density is ([Ellis et al. 1996](#); [Fry et al. 2015](#))

$$N_i = \frac{U_i \mathcal{F}_i}{4} = U_i f_i \frac{M_{\text{ej},i}/A_i m_u}{16\pi r^2} e^{-t/\tau_i} , \quad (5)$$

where the factor of 4 accounts for the ratio of the Earth's cross section to its surface area and we have included a decay factor. Here the uptake factor  $U_i$  measures the fraction of incident atoms of  $i$  that are incorporated into the sample. [Fry et al. \(2016\)](#) note that the fallout will not be uniform over the Earth, favoring mid-latitudes at the expense of the poles and equator. Thus the effective uptake can be different at different sites for this reason alone, in addition to variations in geological conditions.

If multiple radioactive species are measured for the same explosive event, their *isotope ratios* depend on fewer factors. For radioisotopes  $i$  and  $j$ , their surface density ratios in a sample are

$$\frac{N_i}{N_j} = \frac{U_i f_i A_j M_{\text{ej},i}}{U_j f_j A_i M_{\text{ej},j}} \exp [-(\tau_i^{-1} - \tau_j^{-1})t] = \frac{U_i f_i A_j M_i(t)}{U_j f_j A_i M_j(t)} = \frac{U_i f_i Y_i(t)}{U_j f_j Y_j(t)} , \quad (6)$$

where the mass of a radioisotope  $i$  at time  $t$  is  $M_i(t) = M_{\text{ej},i}e^{-t/\tau_i}$ , the mass fraction is  $X_i(t) = M_i(t)/M(t) = M_i(t)/\sum_i M_i(t) = M_i(t)/M_{\text{ej}}$ , as the total mass is conserved in the  $r$ -process ejecta, and thus the abundance at time  $t$  is  $Y_i(t) = X_i(t)/A_i$ , which we obtain from the nucleosynthesis calculations described in Section 3. Physically, Eq. (6) is simply the ratio of number yields, corrected for decay, transport, and uptake. Note that the distance drops out of the expression, but that its derivation implicitly assumed isotropy, in that we took the bulk yield ratios as appropriate approximations in all directions. However, Eq. (6) would still be correct if the angular distributions of the isotopes were similar, even if they were not isotropic.

One of the isotopes proposed for study in Ellis et al. (1996) was  $^{60}\text{Fe}$ , and there have been many subsequent detections of  $^{60}\text{Fe}$  deposits in deep-ocean sediments and ferromanganese crusts (Knie et al. 1999, 2004; Fitoussi et al. 2008; Wallner et al. 2016; Ludwig et al. 2016; Wallner et al. 2020), in the lunar regolith (Fimiani et al. 2016), in cosmic rays (Binns et al. 2016)<sup>1</sup> and in Antarctic ice (Koll et al. 2019). There have also been reported detections in deep-ocean deposits of two other live isotopes considered in Ellis et al. (1996), namely  $^{244}\text{Pu}$  (Wallner et al. 2015) and  $^{53}\text{Mn}$  (Korschinek et al. 2020). These are particularly interesting because they are thought to be produced by different nucleosynthesis mechanisms from  $^{60}\text{Fe}$ : whereas the dominant mechanism for  $^{60}\text{Fe}$  production is neutron capture, that for  $^{53}\text{Mn}$  is thought to be explosive Si burning and nuclear statistical equilibrium (NSE), and that for  $^{244}\text{Pu}$  would be the  $r$ -process.

The deposition of the terrestrial  $^{60}\text{Fe}$  signal started about 3 Mya, peaking around 2.5 Mya, and is interpreted as being due to one or more SNe at a distance  $\mathcal{O}(100)$  pc. The age of the possible  $^{53}\text{Mn}$  signal is similar. In addition, as we have mentioned, there have also been detections of  $^{60}\text{Fe}$  deposits at times outside this peak, in both more recently-deposited Antarctic snow Korschinek et al. (2020)<sup>2</sup> and also in earlier deep-ocean sediments Wallner et al. (2016). Moreover,  $^{244}\text{Pu}$  events have been detected outside the SN  $^{60}\text{Fe}$  peak, and it was argued in Wallner et al. (2015) that the level of  $^{244}\text{Pu}$  deposition is lower than would have been expected if it was due to SN explosions, while being consistent with that expected from the less-frequent KNe.

The existence of the  $^{60}\text{Fe}$  peak focuses interest on the search for other live isotopes deposited around 3 Mya, but there is also interest in looking for earlier radioisotope deposits, e.g., from the epochs of mass extinctions, many examples of which are known in the fossil record. The famous K-T extinction that included the demise of the dinosaurs was triggered by a different type of astrophysical event, namely an asteroid impact, whereas the end-Permian extinction is thought to be due to large-scale volcanism. However, there are other events in the fossil record whose origins are unknown as yet, and detection of coincident radioisotope signatures could provide evidence for any astrophysical origins. Candidate extinctions whose origins could be explored in this way include those at the end of the Devonian epoch  $\sim 360$  Mya (Fields et al. 2020).

In view of the timings of these target events, radioisotopes of interest are those with half-lives between 1 Myr and 1 Gyr. We have therefore identified all nuclides with half-lives from  $t_{1/2} = 1$  Myr to 5 Gyr. We display in Figs. 1 and 2 scatter plots of all radioisotopes with half-lives  $> 10^3$  yr. In Fig. 1 they are ordered by their half-lives, and in Fig. 2 they are ordered by their atomic weights  $A$ , separated in both cases by their respective dominant nucleosynthesis mechanisms. More relevant information about these isotopes is given in Table 1, including their half-lives,  $t_{1/2}$ , their dominant decay modes, the nucleosynthesis mechanisms dominating their production, and comments on the prospects for their detectability, which we develop in more detail later in this paper. The half-lives are from the NUBASE2016 evaluation (Audi et al. 2017) and, unless otherwise noted, the nucleosynthesis processes are from Lugaro et al. (2018) and the AMS detection information is from Kutschera (2013).

We now discuss relevant features of various isotopes listed in Table 1. As noted, there is a large background of  $^{10}\text{Be}$  production by cosmic-ray interactions, so this is not a promising signature of a nearby astrophysical explosion. There is expected to be copious ejection of  $^{53}\text{Mn}$  and  $^{60}\text{Fe}$  by SNe, though production is largely not via the  $r$ -process, and these isotopes are not expected to be prominent in KN debris. The main mechanism for producing the proton-rich isotopes  $^{92}\text{Nb}$  and  $^{97,98}\text{Tc}$  is expected to be the  $p$ -process,<sup>3</sup> while there may be  $p$ -,  $r$ - and  $s$ -process contributions to  $^{93}\text{Zr}$  production. Most of the heavier isotopes with  $A > 100$  are expected to be produced mainly via the  $r$ -process,

<sup>1</sup> We note also an interpretation (Boschini et al. 2021) of recent data from the AMS-02 experiment (Aguilar et al. 2021) that reports an excess of low-energy iron in the cosmic-ray spectrum matching the discoveries of radioactive  $^{60}\text{Fe}$  deposits, and we recall that evidence for a recent SN in cosmic-ray spectra has also been presented by Kachelrieß et al. (2018).

<sup>2</sup> We note that stratigraphically discontinuous Antarctic ice dating back to 2.7 Mya has been recovered (Yan et al. 2019): this overlaps with the  $^{60}\text{Fe}$  pulse discovered in deep-ocean deposits, and it would be interesting to search for live isotopes in ice samples of this age.

<sup>3</sup> As mentioned in Table 1,  $^{97,98}\text{Tc}$  may be produced by SN neutrino interactions in molybdenum, via the reactions  $\nu_e + ^{98}\text{Mo} \rightarrow ^{97}\text{Tc} + e^- + n$  and  $\nu_e + ^{97}\text{Mo} \rightarrow ^{97,98}\text{Tc} + e^-$ . Searches for  $^{97,98}\text{Tc}$  in molybdenum ore could be interesting complementary ways to search for evidence of recent nearby SN explosions (Haxton & Johnson 1988; McGary & Johnson 2007; Lazauskas et al. 2009).

**Table 1.** Radioisotopes with Half-Lives  $t_{1/2} \sim 1$  Myr to 1 Gyr: Astrophysical Production and Geological Detection

Isotope	Half-Life [Myr]	Decay Mode	Nucleosynthesis Process [Lug18]	AMS [Kut13]	Background Measured	Notes on Extrasolar Evidence and Terrestrial Backgrounds [Section 5]
<sup>10</sup> Be	1.51*	$\beta^-$	CR [Gos01]	yes	yes	used as chronometer
<sup>26</sup> Al	0.717	EC	<i>p</i> capture	yes	yes	searches in Fe-Mn crusts
<sup>53</sup> Mn	3.74	EC	NSE	yes	yes	evidence in Fe-Mn crusts [Kor20]
<sup>60</sup> Fe	2.62	$\beta^-$	<i>n</i> capture	yes	no	detected in Fe-Mn crusts and nodules, deep-ocean sediments, Antarctic snow, lunar regolith, cosmic rays
<sup>92</sup> Nb	34.7	$\beta^+$	<i>s</i> , <i>p</i> , $\gamma$ , $\nu$	yes [Guo13]	no	
<sup>93</sup> Zr	1.61	$\beta^-$	<i>p</i> , <i>r</i> , <i>s</i> ? [She20]	yes	no	
<sup>97</sup> Tc	4.2	EC	<i>p</i> [Nis18] <i>n</i> capture, $\gamma$	no	no	possible SN $\nu$ production in Mo ore [Hax88,Ngu05]
<sup>98</sup> Tc	4.2	$\beta^-$	$\gamma$ , <i>p</i> [Nis18], $\nu$ [Hay18]	no	no	possible SN $\nu$ production in Mo ore [Hax88,Ngu05]
<sup>107</sup> Pd	6.5	$\beta^-$	<i>r</i> , <i>n</i> capture	yes	no	
<sup>129</sup> I	15.7*	$\beta^-$	<i>r</i> [Dil08,Dav19] <i>n</i> capture	yes	yes	pre-anthropogenic background seen in Fe-Mn crusts
<sup>135</sup> Cs	1.33	$\beta^-$	<i>n</i> capture, <i>r</i> , <i>s</i>	yes	no	
<sup>146</sup> Sm	68	$\alpha$	<i>p</i> [Nis18]	yes	no	
<sup>150</sup> Gd	1.8	$\alpha$	<i>p</i> [How93]	no	no	
<sup>154</sup> Dy	3.0	$\alpha$	<i>p</i>	no	no	
<sup>182</sup> Hf	8.9	$\beta^-$	<i>r</i> [Voc04], <i>s</i> , <i>n</i>	yes	no	
<sup>205</sup> Pb	17	EC	<i>s</i> , <i>n</i> , <i>p</i>	yes	no	
<sup>235</sup> U	704	$\alpha$	<i>r</i>	yes	yes	high natural background
<sup>236</sup> U	23.4	$\alpha$	<i>r</i>	yes	yes	natural and anthropogenic background
<sup>237</sup> Np	2.14	$\alpha$	<i>r</i>	yes	yes	anthropogenic background seen
<sup>244</sup> Pu	80*	$\alpha$	<i>r</i>	yes	yes	anthropogenic signature from global fallout [Ste13], non-anthropogenic evidence in Fe-Mn crusts
<sup>247</sup> Cm	15.6	$\alpha$	<i>r</i>	yes	no	possible anthropogenic background

*Notes:*

Our calculations use half-lives from NUBASE2016 (Audi et al. 2017) as implemented in Mumpower et al. (2018); Sprouse et al. (2020). As indicated by asterisks, the recent NUBASE2020 update (Kondev et al. 2021) has small changes to some values, including the *r*-process species <sup>129</sup>I and <sup>244</sup>Pu.

Decay mode:  $\beta^-$  =  $\beta$  decay,  $\beta^+$  = positron emission, EC = electron capture,  $\alpha$  = decay by  $\alpha$  emission.

Nucleosynthesis process: CR = cosmic-ray spallation, *s* = *s*-process, *p* = *p*-process,  $\nu$  =  $\nu$ -process, *r* = *r*-process,  $\gamma$  =  $\gamma$ -process.

AMS: accelerator mass spectrometry demonstrated for this isotope.

Background measured: natural or anthropogenic levels detected.

*References:* [Dav19] Davila et al. (2019), [Dil08] Dillmann (2008), [Gos01] Gosse & Phillips (2001), [Guo13] Guozhu et al. (2013), [Hax88] Haxton & Johnson (1988), [Hay18] Hayakawa et al. (2018), [How93] Howard (1993), [Kor20] Korschinek et al. (2020), [Kut13] Kutschera (2013), [Lug18] Lugaro et al. (2018), [Ngu05] McGary & Johnson (2007), [Nis18] Nishimura et al. (2018), [She20] Shetye et al. (2020), [Ste13] Steier et al. (2013), [Voc04] Vockenhuber et al. (2004).

exceptions being <sup>146</sup>Sm, <sup>150</sup>Gd, <sup>154</sup>Dy and <sup>205</sup>Pb. <sup>4</sup> In the cases of the actinide isotopes, one must be mindful of the possible presence of terrestrial anthropogenic contamination by nuclear accidents or bomb debris, which was an issue for the analysis of <sup>236</sup>U and <sup>237</sup>Np in *Apollo* lunar regolith samples (Fields et al. 1972, 1976). The ambient terrestrial level of <sup>244</sup>Pu has been measured in Winkler et al. (2004), and the detection of <sup>244</sup>Pu in deep-ocean deposits by Wallner et al. (2015) is thought to be free of this background.

We focus in the following on the *r*-process isotopes listed in Table 1 and their production by SNe and KNe.

<sup>4</sup> We do not include in Table 1 or our subsequent considerations the long-lived state <sup>210</sup>Bi\*, an excitation lying 271 keV above the ground state, which is expected to have a low production rate in all the models studied.

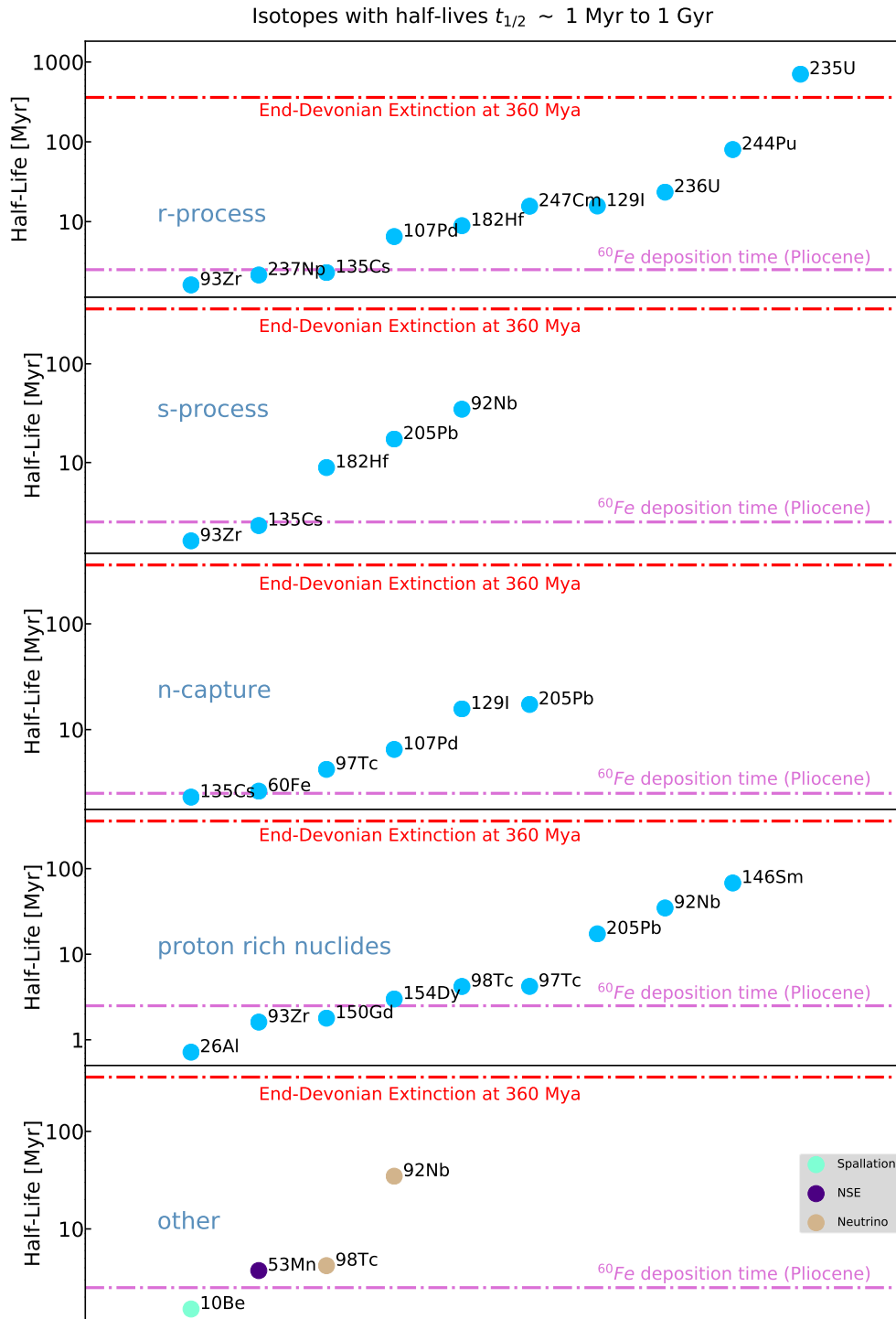


**Figure 1.** Radioisotopes with half-lives of interest to searches for nearby supernova and kilonova explosions. The horizontal lines indicate the age of the supernova explosion  $\sim 3 \text{ Mya}$  attested by discoveries of deposits of  $^{60}\text{Fe}$  (orchid). The horizontal red line marks the end-Devonian time scale. These five panels represent different nucleosynthesis channels, with the proton-rich nuclides panel including both p-process and  $\gamma$ -process isotopes. The isotopes are ordered by increasing half-life.

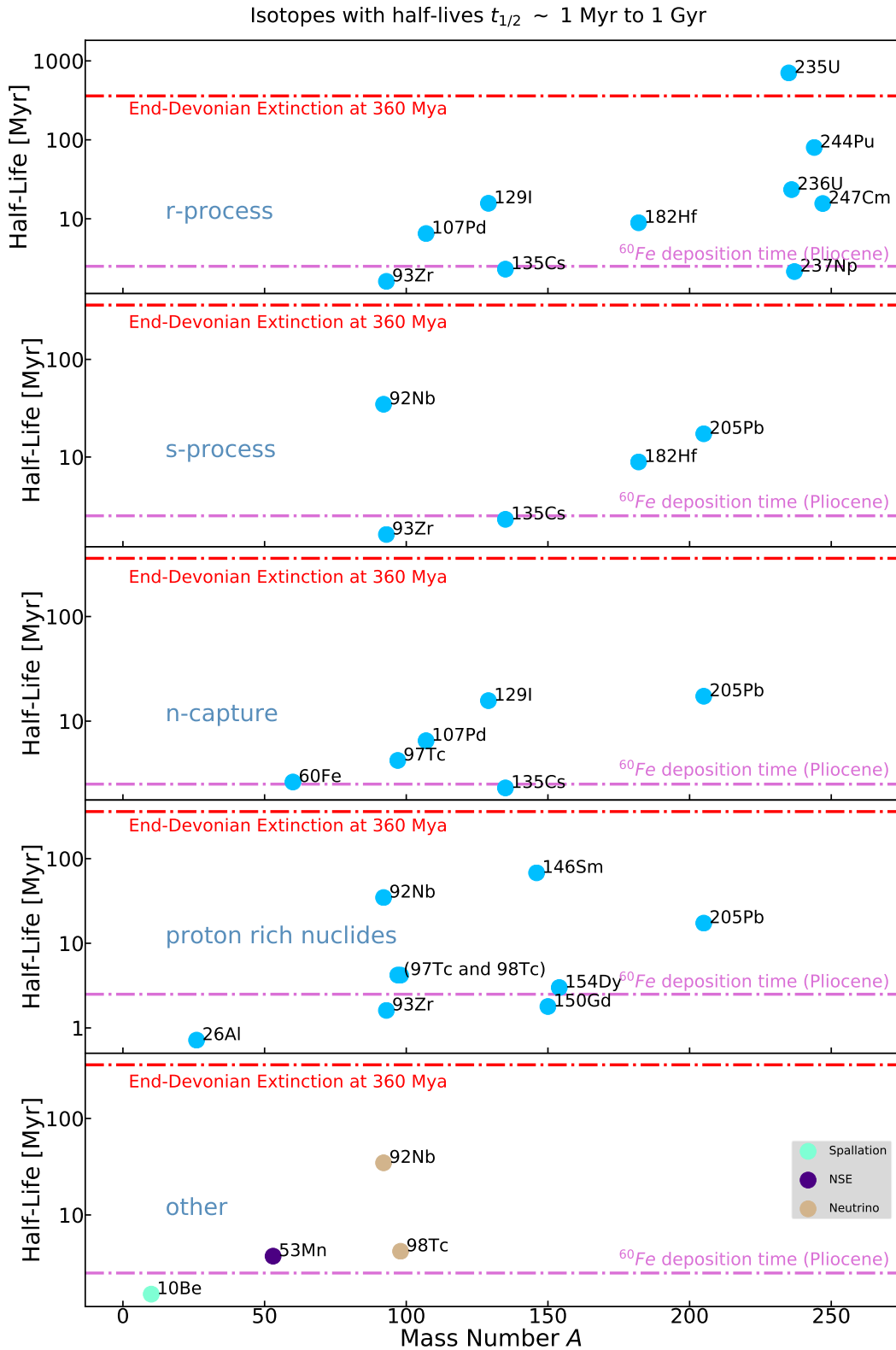


Figure 2. As in Fig. 1, but with the isotopes ordered by isotope mass number A.

### 3. MODELING $r$ -PROCESS PRODUCTION IN SUPERNOVAE AND KILONOVAE

Production ratios of radioactive isotopes resulting from an  $r$ -process event can be estimated by the extraction and post-processing of ejected matter trajectories from astrophysical simulations of the event. The trajectories contain the time history of  $(\rho, T, Y_e)$ , where  $\rho$  is the density,  $T$  is the temperature, and the electron fraction  $Y_e = n_e/n_B = \langle Z/A \rangle$  measures the neutron richness  $Y_n = 1 - Y_e = \langle N/A \rangle$ . The evolution of the nuclear material along this trajectory is then calculated using a network of the relevant nuclear reactions. This procedure brings with it significant challenges, starting from the identification and characterization of the appropriate nucleosynthetic sites within the candidate event.

While neutron star mergers have been confirmed to produce  $r$ -process elements (Abbott et al. 2017; Abbott et al. 2017; Cowperthwaite et al. 2017; Kasen et al. 2017), exactly how, where, and how much has yet to be definitively worked out (see reviews Cowan et al. 1991; Arnould et al. 2007; Kajino et al. 2019; Cowan et al. 2021, and references therein). Possible nucleosynthetic environments within a merger include the prompt ejecta—cold, very neutron-rich tidal tails and/or shock-heated ejecta from the neutron star contact interface (Bauswein et al. 2013; Hotokezaka et al. 2013; Rosswog et al. 2013; Endrizzi et al. 2016; Lehner et al. 2016; Sekiguchi et al. 2016; Rosswog et al. 2017)—and magnetic, viscous, and/or neutrino-driven outflows from the resulting accretion disk (Chen & Beloborodov 2007; Surman et al. 2008; Dessart et al. 2009; Wanajo et al. 2014; Perego et al. 2014; Martin et al. 2015; Just et al. 2015; Siegel & Metzger 2018). The composition and relative contributions of each type of mass ejection depend on quantities such as the physical parameters of the merging system and the still-unknown microphysics of dense matter and its neutrino emission (see, e.g., Caballero et al. 2012; Foucart et al. 2015; Malkus et al. 2016; Kyutoku et al. 2018).

Supernovae were the first type of event suggested for  $r$ -process production (Burbidge et al. 1957), and for many decades the core-collapse SN neutrino-driven wind was considered the leading candidate site. However, modern simulations show that the neutrino-driven wind is unlikely to be sufficiently neutron-rich to synthesize the actinides (Fischer et al. 2010; Hudepohl et al. 2010; Arcones & Thielemann 2013), though it may produce  $A \sim 80$ -100 species through a weak  $r$ -process (Bliss et al. 2018) or a  $\nu p$ -process (Fröhlich et al. 2006). The ultimate extent of nucleosynthesis in this environment depends on neutrino physics that is not fully understood (Balantekin & Yüksel 2005; Duan et al. 2011; Johns et al. 2020; Xiong et al. 2020). Rare types of core-collapse events may also generate neutron-rich outflows, with promising candidates including magnetorotational supernovae (MHD SNe) (Winteler et al. 2012; Mösta et al. 2018a; Reichert et al. 2021) and collapsars (Pruet et al. 2003; Surman et al. 2006; Fujimoto et al. 2008; Siegel et al. 2019). Studies of galactic chemical evolution suggest that, whilst collapsars might have been important early in the history of the Universe during the epoch of Population-III stars, they have been less relevant during the epochs of interest for this study. For this reason, and given the uncertainty in how robust collapsar  $r$ -process calculations might be (Miller et al. 2020), we do not consider them further in this paper.<sup>5</sup>

Here we calculate isotopic production ratios for four example  $r$ -process model combinations, using trajectories from: a *modified* SN neutrino-driven wind scenario (SA), an MHD SN model (SB), and two NSM disk and dynamical ejecta combinations (KA and KB). We use the isotope abundances measured from the metal-poor star HD160617, for which all three  $r$ -process peaks elements have been detected (Roederer & Lawler 2012), and J0954+5246, which is the most actinide-boosted star ever detected (Holmbeck et al. 2018), to constrain our predictions from these models, since the  $r$ -process enrichments in such stars are most likely from one (or at most a few)  $r$ -process events. We use a variety of  $r$ -process species to normalize our estimates, including platinum, tellurium, cadmium and zirconium. The details of each model combination and constraint are described below and summarized in Table 2. The total mass of the  $r$ -process ejecta for each model is normalized to unity.

Our nucleosynthesis calculations are made with the nuclear reaction network code Portable Routines for Integrated nucleoSynthesis Modeling (PRISM) (Mumpower et al. 2018; Sprouse et al. 2020), implemented as in Wang et al. (2020b) for the baseline calculation. We note that isotopic ratio estimates are shaped in addition by the nuclear physics properties of the thousands of exotic nuclei that participate in an  $r$ -process. Thus for each model we explore variations in the nuclear inputs for quantities for which experimental values are unavailable (masses from Goriely et al. (2009) (HFB), or  $\beta$ -decay rates from Marketin et al. (2016) (MKT) for both SN and KN models, and fission yields from Kodama & Takahashi (1975) for KN models), as in Wang et al. (2020a). Additionally, because of the general limitation of the network code for timestep evolution at times  $\gtrsim$  Myr, which results in large timesteps comparable to

<sup>5</sup> We note the suggestion that core-collapse SNe driven by the quark-hadron transition might also be rare  $r$ -process sites (Fischer et al. 2020), but also do not discuss this possibility here.

the half-lives of radioisotopes of interest in this work such as  $^{93}\text{Zr}$ , we use PRISM to generate *r*-process abundance yields until 1 kyr for  $^{182}\text{Hf}$  and lighter radioisotopes, and until 1 Myr for actinides (except for  $^{248}\text{Cm}$  and  $^{245}\text{Cm}$ , for which we run until 0.1 Myr), and then switch to a pure radioactive decay calculation for these radioisotopes. These calculations provide the relative abundance yields for the radioisotopes, i.e., the  $Y_i(t)$  in Eq. (6).

As commented above, the SN neutrino-driven wind scenario has fallen out of favor as a primary *r*-process site because modern simulations do not show sufficiently neutron-rich conditions to reproduce the solar *r*-process pattern (Fischer et al. 2010; Hüpdepohl et al. 2010; Arcones & Thielemann 2013). Indeed, no actinides are produced at all. We are however motivated by the intriguing possibility of coincident identifications of  $^{60}\text{Fe}$  and  $^{244}\text{Pu}$  to consider here a *modified* neutrino-driven wind scenario, denoted below by ‘ $\nu\star$  wind’. We start with the neutrino-driven wind simulations of Arcones et al. (2007); Arcones & Janka (2011) and modify the initial  $Y_e$  in order to produce different *r*-process yields. The upper panel of Fig. 3 shows the final abundance pattern results at  $t \sim 10$  Gyr for four values of  $Y_e = 0.31$  (blue), 0.35 (yellow), 0.42 (green) and 0.48 (pink). We have found that results for  $Y_e \leq 0.31$ , following different trajectories, and using different nuclear networks, make qualitatively similar predictions for substantial production of isotopes with atomic numbers  $A \gtrsim 130$ , up to and including the actinides. On the other hand, simulations with  $Y_e \geq 0.38$  yield much less production of isotopes with  $A \gtrsim 130$ , as exemplified by the results shown in green and pink. The results shown in red are for a mixture (model SA) of the simulations for SN *modified* neutrino-driven wind with four different values of  $Y_e$  (see Table 2), whose relative normalizations are scaled to fit data on the abundances of platinum, tellurium, cadmium and zirconium in the metal-poor star HD160617 (Roederer & Lawler 2012). These and other abundances are shown in grey in the upper panel of Fig. 3, and we see in the lower panel of Fig. 3 that model SA also matches the solar abundance data very well.

	Supernova (SN) Models		Kilonova (KN) Models	
Label	SA ( $\nu\star$ )	SB (MHD)	KA	KB
Simulations	SN <i>modified</i> neutrino-driven wind: 4 trajectories from Arcones et al. (2007); Arcones & Janka (2011) with modified $Y_e = 0.31, 0.35, 0.42, 0.48$	MHD SN: 2 trajectories from Mösta et al. (2018b)	KN dynamical ejecta: 2 trajectories from Bovard et al. (2017)	diskwind: 2 trajectories from Just et al. (2015)
Scaling	HD160617: Pt, Te, Cd and Zr	HD160617: Pt and Zr	HD160617: Pt and Zr	J0954+5246: Pt and Zr

**Table 2.** Combinations of SN modified neutrino-driven models (Arcones et al. 2007; Arcones & Janka 2011) and MHD models (Mösta et al. 2018b) constrained by the observations of the metal-poor star HD160617 (Roederer & Lawler 2012) (SA and SB, respectively), and combinations of KN dynamical ejecta models (Bovard et al. 2017) with disk neutrino-driven wind models from Just et al. (2015), constrained by observations of HD160617 (KA) or the actinide-boost star J0954+5246 (Holmbeck et al. 2018) (KB).

Fig. 4 shows analogous results using the Mösta et al. (2018b) MHD supernova model. In the upper panel, we show the abundance predictions of two trajectories (blue and green) and a combination (SB, red) fitted to the abundances of platinum and zirconium measured in the metal-poor star HD160617 (Roederer & Lawler 2012) (see Table 2). These and other abundances are shown in grey in the upper panel of Fig. 4, and we see in the lower panel of Fig. 4 that this mixture of simulations also matches the solar abundance data quite well in general, though it overestimates the structure seen in the solar data for  $A \sim 130$ , and falls off more rapidly for  $A \gtrsim 190$ .

The upper panel of Fig. 5 shows results from representative simulations of the abundances of nuclei produced by the *r*-process (at  $t \sim 10$  Gyr) in KN dynamical ejecta based on the work of Bovard et al. (2017) (blue), and of KN disk neutrino-driven wind based on the work of Just et al. (2015) (green). Also shown is a combination of these simulations (KA, red) fitted to the abundances of platinum and zirconium in the metal-poor star HD160617 (Roederer & Lawler 2012) (see Table 2). These and other abundances are shown in grey in the upper panel of Fig. 5, and we see in the lower panel of Fig. 5 that the KA model also matches the solar abundance data quite well, though with some deviations for  $A \sim 140$ .

Similarly to Fig. 5, Fig. 6 shows analogous results obtained using the KN dynamical model with a relatively more neutron-rich trajectory from Bovard et al. (2017) (blue), and the disk neutrino-driven wind model of Just et al. (2015). Also shown are the prediction of a combination (KB, red) fitted to the abundances of platinum and zirconium measured in the actinide-boost star J0954+5346 (Holmbeck et al. 2018). These and other abundances are shown in grey in the upper panel of Fig. 6, and we see in the lower panel of Fig. 6 that it also matches the solar abundance data quite well in general, though with some deviations from the solar data for  $A \sim 120$  and  $A \sim 135$ . The KA and KB models

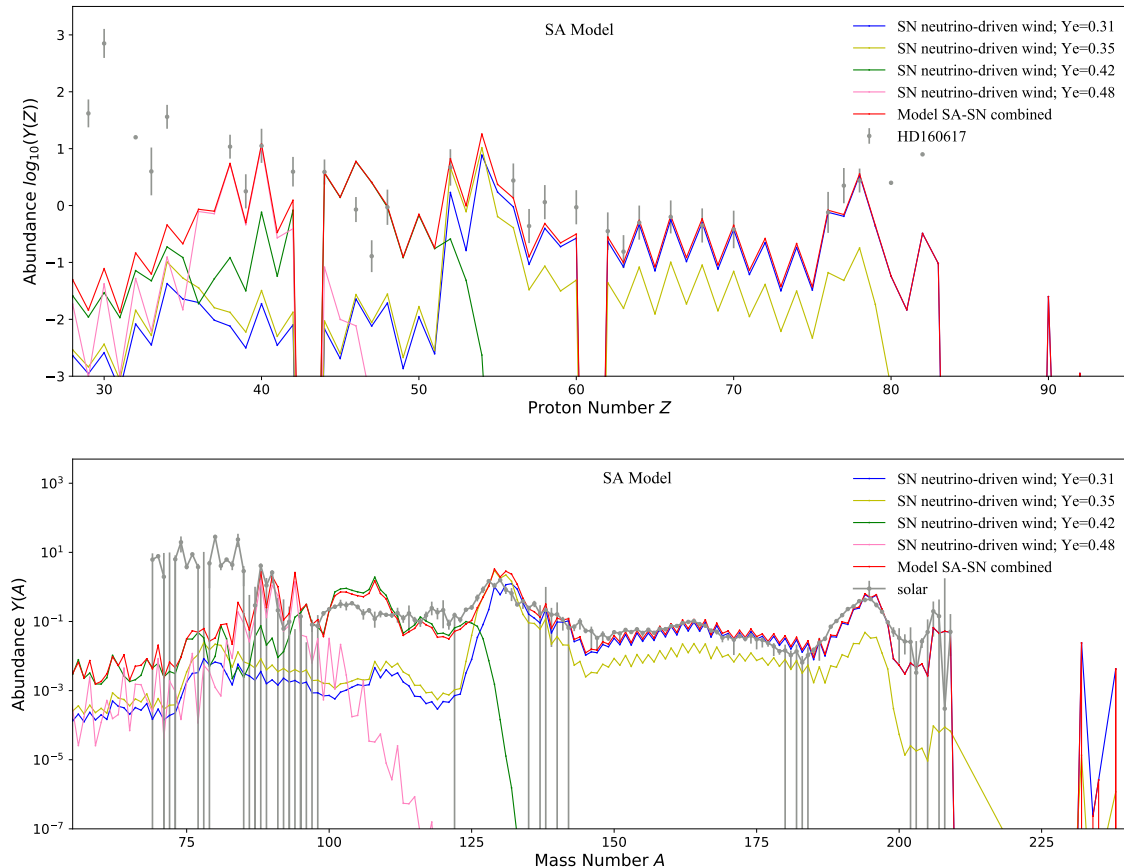


**Figure 3.** Upper panel: The abundances at  $t \sim 10$  Gyr of  $r$ -process nuclei produced in supernova modified neutrino-driven wind simulations from Arcones et al. (2007); Arcones & Janka (2011) with the electron fractions  $Y_e = 0.31$  (blue), 0.35 (yellow), 0.42 (green) and 0.48 (pink), and a combination (SA, red) fitted to abundances measured in the metal-poor star HD160617 (Roederer & Lawler 2012), plotted as functions of the atomic number  $Z$ . Lower panel: A comparison with the corresponding solar abundance data (Arnould et al. 2007), plotted as functions of the atomic weight  $A$ .

both exhibit robust production of actinides that subsequently fission, so fission yields play important roles in shaping the second peak in these models (Eichler et al. 2015; Vassh et al. 2019, 2020; Giuliani et al. 2020). The fission yields of most neutron-rich actinides have not been experimentally determined, so in addition to the simple symmetric split fission yields adopted in the baseline calculation, we also implement the wide Gaussian fission yields from Kodama & Takahashi (1975) to estimate the uncertainty range. We find that the fission yields from Kodama & Takahashi (1975) would bring a small boost to the left and right side of the second peak ( $A \sim 120$  and  $A \sim 133$ ) for the KA model, while leaving the yields of the interesting  $r$ -process radioisotopes listed in Table 4 largely unchanged. For the KB model with boosted actinide production, fission deposition could potentially fill the gap around  $A \sim 120$  and lower the bump around  $A \sim 133$  to bring the abundance pattern closer to the solar pattern, thus resulting in a smaller  $^{135}\text{Cs}$  yield.

#### 4. R-PROCESS RADIOISOTOPE RATIOS AND TIME EVOLUTION

We have already seen in Figs. 3, 4, 5 and 6 that the abundances of different  $r$ -process radioisotopes depend sensitively on the model of the supernova or kilonova that is adopted. The same holds for actinide isotopes even when attention is focused on hybrid models whose parameters are adjusted to yield ratios of the radioisotopes with  $A \lesssim 200$  that are similar to those measured for the metal-poor star HD160617 or the actinide-boost star J0954+5346. Table 3 shows the production ratios for  $r$ -process isotopes of interest after  $10^5$  ya (i.e., after the decays of short-lived isotopes) calculated from the SN and KN models studied in the previous Section 3, expressed as the abundance ratios relative to  $^{244}\text{Pu}$ . Included here are the production ratios for several  $r$ -process isotopes with half-lives  $> 500$  Myr, namely  $^{232}\text{Th}$ ,  $^{235}\text{U}$ , and  $^{238}\text{U}$ . In view of the backgrounds from astrophysical processes before the formation of the solar system, we do

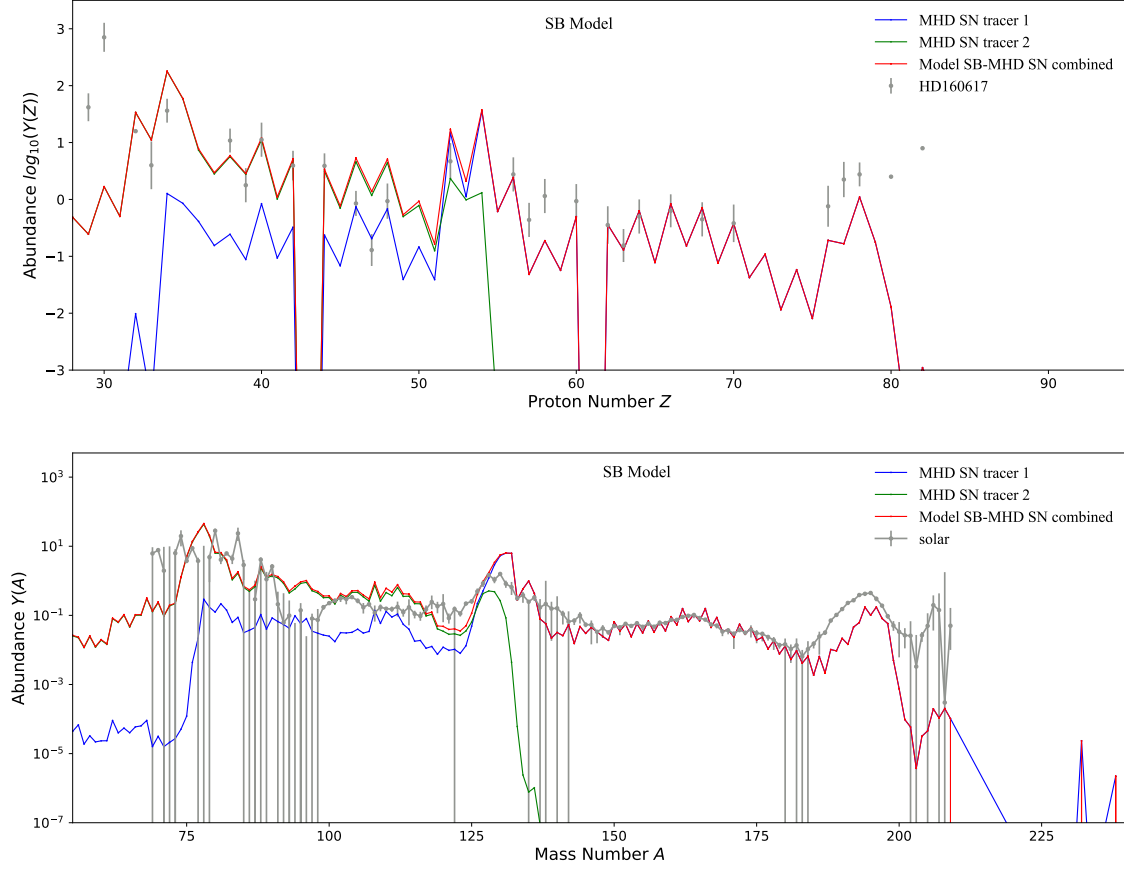


**Figure 4.** Upper panel: The abundances at  $t \sim 10$  Gyr of  $r$ -process nuclei produced in magneto-rotational (MHD) SN simulations from M $\ddot{o}$ sta et al. (2018b) with two different tracers 1 (blue) and 2 (green) and a combination (SB, red) fitted to the abundances of platinum and zirconium measured in the metal-poor star HD160617 (Roederer & Lawler 2012), plotted as functions of the atomic number  $Z$ . Lower panel: A comparison with the corresponding solar abundance data (Arnould et al. 2007), plotted as functions of the atomic weight  $A$ .

not consider further these isotopes. Also, we note that SNe in general produce  $^{60}\text{Fe}$  by other nuclear mechanisms in addition to the  $r$ -process, so the  $^{60}\text{Fe}/^{244}\text{Pu}$  ratios for SN models SA and SB in this and subsequent Tables are in general underestimates and could be viewed as a lower limit of the actual ratio. If the ratio of the  $^{60}\text{Fe}$  synthesized through the  $r$ -process to the total  $^{60}\text{Fe}$  produced in a SN is  $\sim f(^{60}\text{Fe}, r)$ , then the  $^{60}\text{Fe}/^{244}\text{Pu}$  ratio for the SN model is boosted to  $Y(^{60}\text{Fe})/(f(^{60}\text{Fe}, r)Y(^{244}\text{Pu}))$ . Additionally, our SN models provide the estimates per  $r$ -process event  $Y_i(\text{SN}, r)$ , implicitly assuming that all SNe are similar  $r$ -process sites. As only a small fraction of SNe may be  $r$ -process sites, we may account for supernova heterogeneity by assuming, in the crudest picture, that the  $r$ -process occurs in only a fraction  $f_{\text{SN}, r}$  of SNe. In this case, the probability that a given SN will eject  $r$ -process material is  $f_{\text{SN}, r}$ , implying that, for the  $r$ -process yield per SN event  $Y_i(\text{SN})$  must be lower, i.e.,  $Y_i(\text{SN}) = f_{\text{SN}, r} Y_i(\text{SN}, r)$ .

Fig. 7 displays the subsequent time evolution of several radionuclides of interest ( $^{60}\text{Fe}$ ,  $^{93}\text{Zr}$ ,  $^{107}\text{Pd}$ ,  $^{129}\text{I}$ ,  $^{135}\text{Cs}$ ,  $^{182}\text{Hf}$ ,  $^{244}\text{Pu}$  and  $^{247}\text{Cm}$ ) as calculated using the SN and KN models discussed in the previous Section. The solid lines were obtained using our baseline  $r$ -process calculation, and the shaded bands are the ranges due to uncertainties resulting from the adoption of different nuclear data in this calculation. Also shown as vertical lines are three time scales of interest, namely the age of the well-attested supernova explosion  $\sim 3$  Mya, an age of 50 Mya comparable with the half-life of  $^{244}\text{Pu}$ , and the age of the end-Devonian extinction(s)  $\sim 360$  Mya. We see that there are substantial differences between the abundances of the radioisotopes calculated in different models. Note that the relative production rates of light (second peak and lighter) and heavy (third peak and higher)  $r$ -process nuclei depend strongly on the astrophysical conditions of the  $r$ -process sites. On the other hand, the relative ratios of the actinides themselves are largely insensitive to the site and thus have less discriminating power. The uncertainties in the relative yields of the actinides are dominated by large nuclear physics uncertainties in this region, so their yields depend sensitively on the choice of

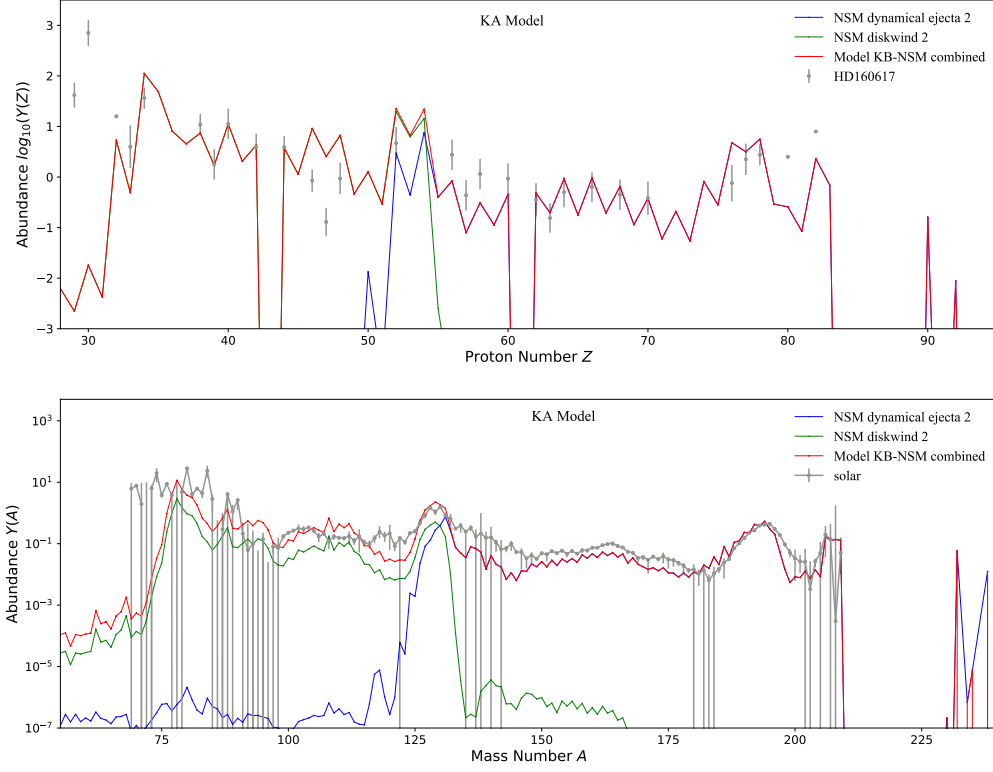


**Figure 5.** Upper panel: The abundances at  $t \sim 10$  Gyr of  $r$ -process nuclei produced in simulations of KN dynamical ejecta from *Bovard et al. (2017)* (blue) and of disk neutrino-driven wind from *Just et al. (2015)* (green), and a mixture (KA, red) fitted to measurements of the metal-poor star HD160617 (*Roederer & Lawler 2012*), plotted as functions of the atomic number  $Z$ . Lower panel: The corresponding abundance pattern of model KA compared with solar abundance data (*Arnould et al. 2007*), plotted as functions of the atomic weight  $A$ .

**Table 3.**  $r$ -Process Isotope Production Ratios after  $10^5$  yr

Radioisotope Ratio	Supernova Model		Kilonova Model	
	SA	SB	KA	KB
$^{60}\text{Fe}/^{244}\text{Pu}$	0.39	$2.5 \times 10^4$	$8.6 \times 10^{-3}$	$4.5 \times 10^{-5}$
$^{93}\text{Zr}/^{244}\text{Pu}$	35	$6.4 \times 10^5$	28	1.1
$^{107}\text{Pd}/^{244}\text{Pu}$	$1.4 \times 10^2$	$3.9 \times 10^5$	18	1.8
$^{129}\text{I}/^{244}\text{Pu}$	$7.1 \times 10^2$	$4.5 \times 10^6$	$1.8 \times 10^2$	41
$^{135}\text{Cs}/^{244}\text{Pu}$	48	$1.2 \times 10^6$	2.6	13
$^{182}\text{Hf}/^{244}\text{Pu}$	7.5	$1.2 \times 10^4$	1.5	0.28
$^{232}\text{Th}/^{244}\text{Pu}$	2.7	24	1.7	0.65
$^{235}\text{U}/^{244}\text{Pu}$	2.9	15	3.1	1.7
$^{236}\text{U}/^{244}\text{Pu}$	3.8	23	3.7	2.4
$^{238}\text{U}/^{244}\text{Pu}$	2.2	9.6	2.4	1.5
$^{237}\text{Np}/^{244}\text{Pu}$	3.3	8.9	3.4	2.6
$^{242}\text{Pu}/^{244}\text{Pu}$	1.9	2.6	1.9	1.9
$^{247}\text{Cm}/^{244}\text{Pu}$	1.1	1.2	0.97	1.0
$^{248}\text{Cm}/^{244}\text{Pu}$	1.1	1.5	0.86	1.1

nuclear data adopted (as seen in Figure 7). Therefore measurements of radioisotope ratios, especially the ratios of

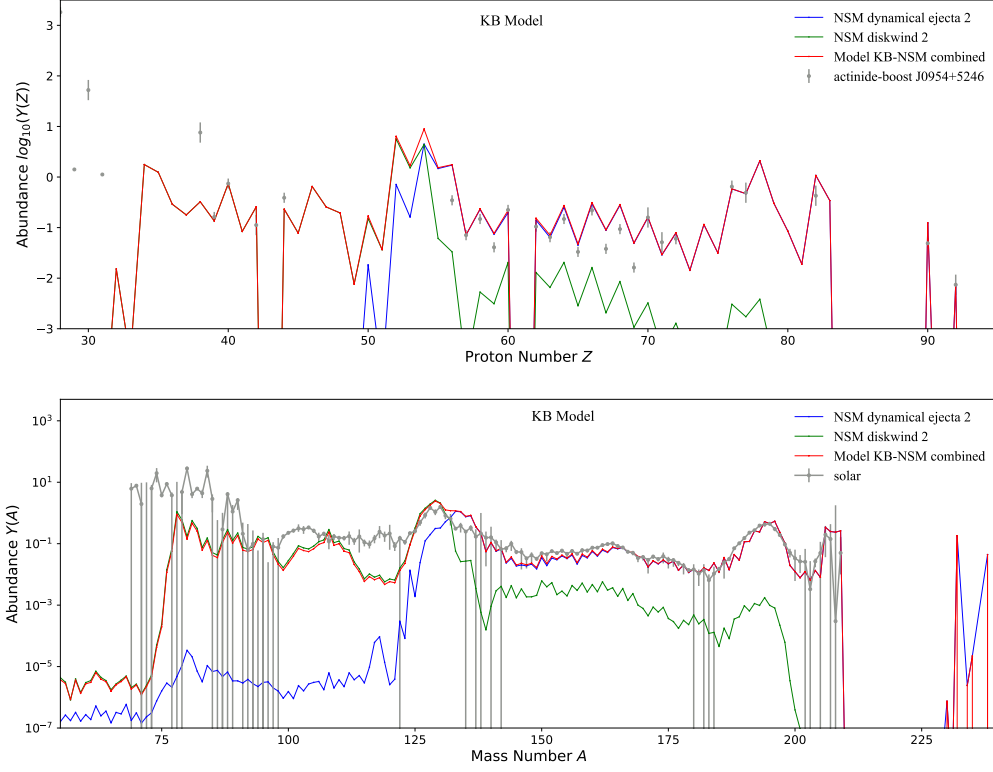


**Figure 6.** Upper panel: The abundances (at  $t \sim 10\text{Gyr}$ ) of *r*-process nuclei produced in simulations of KN more neutron rich dynamical ejecta from Bovard et al. (2017) (blue) and of disk neutrino-driven wind from Just et al. (2015) (green), and a mixture (KB, red) fitted to the measurements of the actinide-boost star J0954+5346 (Holmbeck et al. 2018), plotted as functions of the atomic number  $Z$ . Lower panel: The corresponding abundance pattern of model KB compared with solar abundance data (Arnould et al. 2007), plotted as functions of the atomic weight  $A$ .

light *r*-process nuclei to actinides, could provide useful diagnostic tools for the nature of any astrophysical explosion that occurred near Earth within the last few hundred million years.

As we have already discussed, measurements of terrestrial  $^{60}\text{Fe}$  deposits indicate that at least one such explosion took place within  $\sim 100$  Pc of Earth about 3 Mya, and there have been several reports of the detection of  $^{244}\text{Pu}$  deposited on Earth within the past 25 Myr. If confirmed, the presence of  $^{244}\text{Pu}$  would indicate that there has been at least one active *r*-process site close to Earth within the past 80 Myr or so. In the following, we treat the  $^{244}\text{Pu}$  abundance as our reference, and predict the relative abundances of other *r*-process radioisotopes under different hypotheses about the nature(s) of this (these) site(s) and its (their) timing.

For this purpose, we follow the evolution of interesting radioisotopes over  $\sim \text{Gy}$ , using the calculations of the previous Section as starting points and taking account of the possible production of the radioisotopes via the decays of heavier isotopes as well as their own decays. The left panels of Fig. 8 illustrate the abundances of the radioisotopes of principal interest, while the right panels show ratios to  $^{244}\text{Pu}$ . The upper panels show results calculated in supernova model SA, and the lower panels show results in model SB. Most of the radioisotopes exhibit simple decay curves, but the effects of feed-through from decays of heavier isotopes are visible in  $^{244}\text{Pu}$ , which is made in  $\alpha$  decays of  $^{248}\text{Cm}$ , and  $^{236}\text{U}$ , which is a decay product of  $^{244}\text{Pu}$ . We have included the *r*-process production of  $^{60}\text{Fe}$  in these plots, although the *r*-process is not expected to dominate its production, at least in core-collapse supernovae. Hence the  $^{60}\text{Fe}$  curves should be regarded as (very) conservative lower bounds on the  $^{60}\text{Fe}$  yields and ratios to  $^{244}\text{Pu}$  production.

The vertical lines in Fig. 8 are at 3 Myr, corresponding to the time since the event that gave rise to the well-attested deep-ocean  $^{60}\text{Fe}$  deposition, 50 Myr comparable with the half-life of  $^{244}\text{Pu}$ , and 360 Myr, corresponding to the time since the end-Devonian extinction(s). If the reported  $^{244}\text{Pu}$  signal is associated with the same event as the  $^{60}\text{Fe}$  signal from 3 Mya, all radioisotopes with yields  $Y \gtrsim Y(^{244}\text{Pu})$  would be interesting targets for searches in the layers containing the  $^{60}\text{Fe}$  signal. Depending on the model, these may include  $^{93}\text{Zr}$ ,  $^{107}\text{Pd}$ ,  $^{129}\text{I}$ ,  $^{135}\text{Cs}$ ,  $^{182}\text{Hf}$ ,  $^{236}\text{U}$ ,  $^{237}\text{Np}$

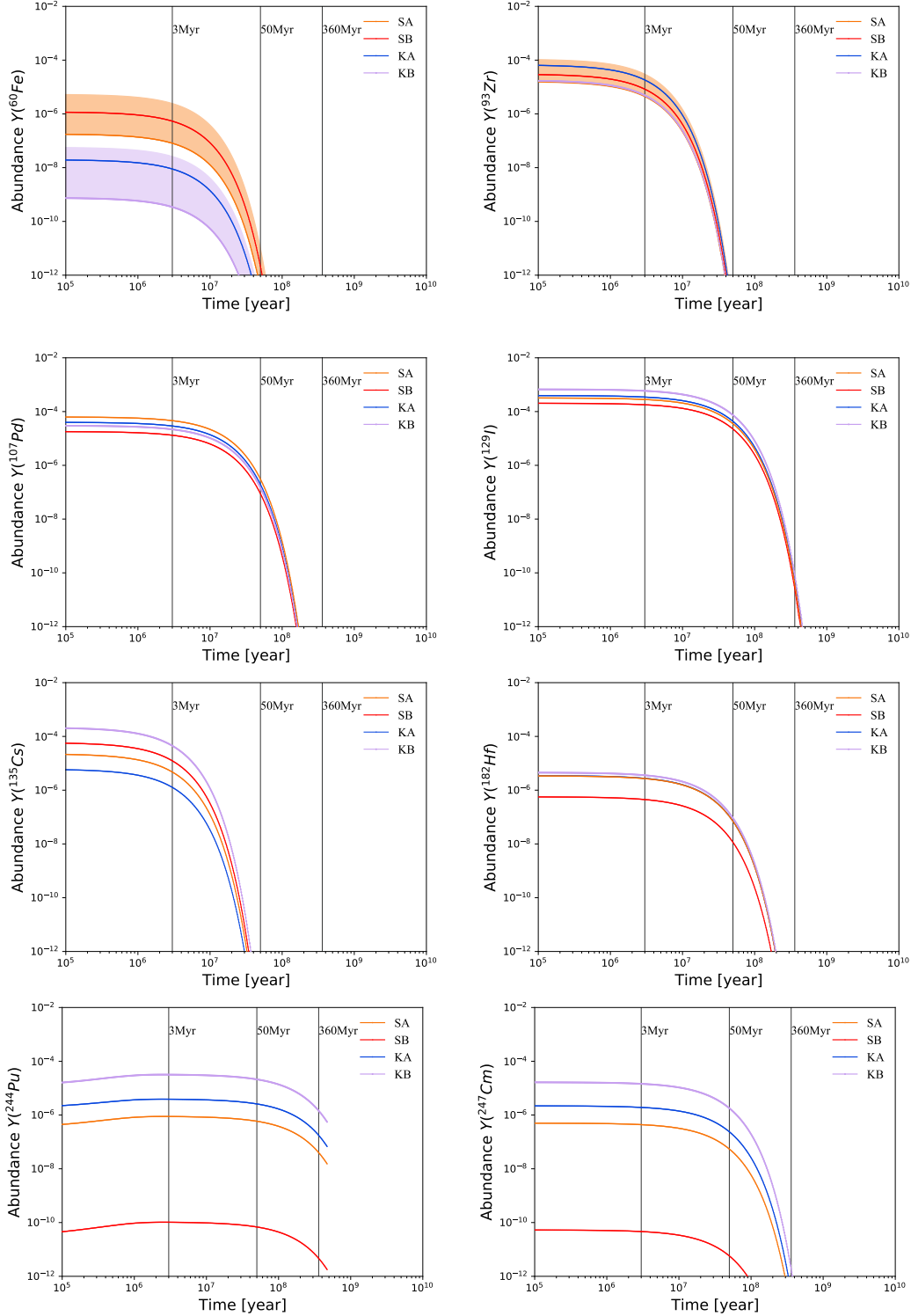


**Figure 7.** The time evolutions of the relative abundances of  $^{60}\text{Fe}$ ,  $^{93}\text{Zr}$ ,  $^{107}\text{Pd}$ ,  $^{129}\text{I}$ ,  $^{135}\text{Cs}$ ,  $^{182}\text{Hf}$ ,  $^{244}\text{Pu}$ , and  $^{247}\text{Cm}$  as calculated with the different astrophysical models described in Table 2, with the total mass of r-process species normalized to unity for each model. The solid lines were obtained using our baseline r-process calculation, and the shaded bands are the ranges due to uncertainties resulting from the adoption of different nuclear data (HFB masses from Goriely et al. (2009) or  $\beta$ -decay rates from Marketin et al. (2016) for both SN and KN models, or fission yields from Kodama & Takahashi (1975) for KN models, in addition to the baseline nuclear data) in this calculation (orange: uncertainties for SN models; light purple: uncertainties for KN models). The vertical lines indicate the age of the supernova explosion  $\sim 3$  Mya attested by discoveries of deposits of  $^{60}\text{Fe}$ , an age of 50 Mya comparable with the half-life of  $^{244}\text{Pu}$ , and the age of the end-Devonian extinction(s)  $\sim 360$  Mya.

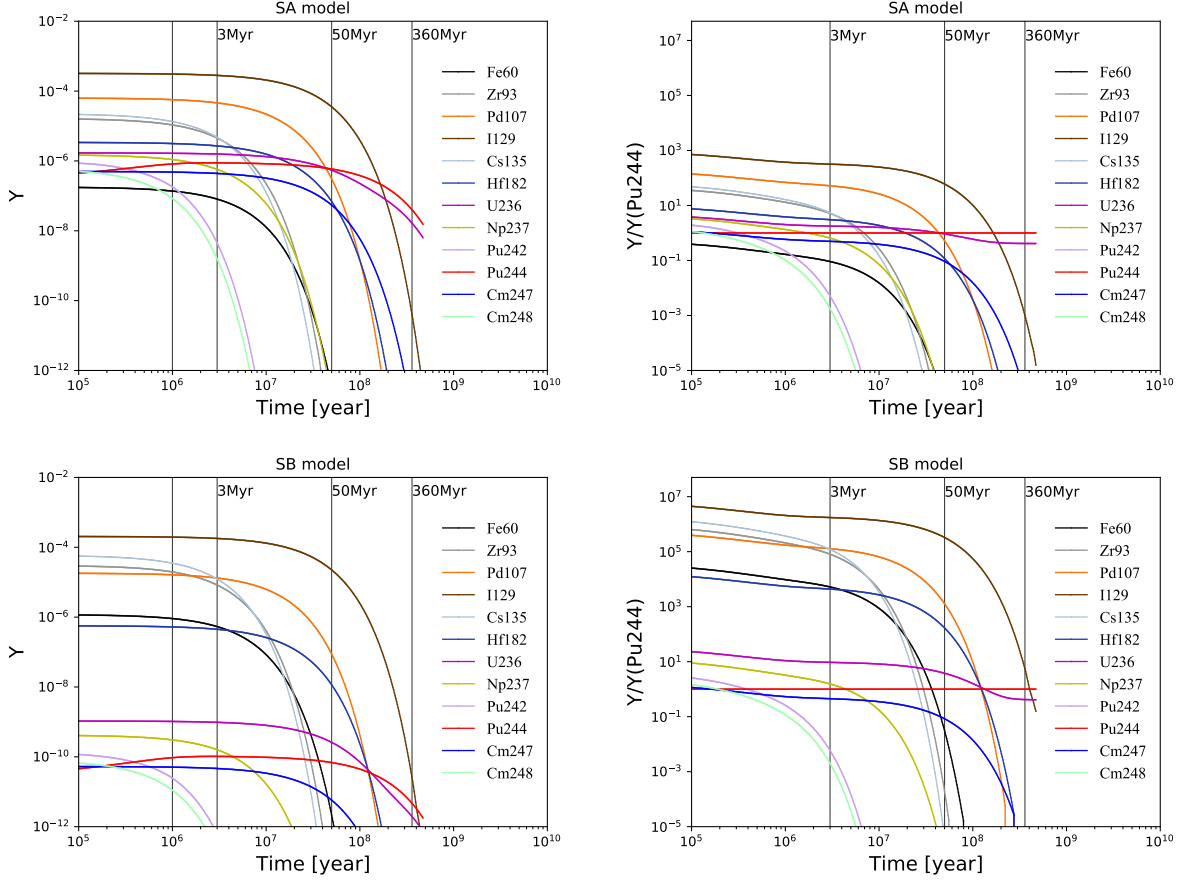


**Figure 8.** The time evolution of the abundances  $Y$  (left) and ratios  $Y/Y(^{244}\text{Pu})$  (right) of *r*-process nuclei of interest from supernova model SA (top panels) and MHD supernova model SB (bottom panels). The vertical lines indicate the age of the supernova explosion  $\sim 3$  Mya attested by discoveries of deposits of  $^{60}\text{Fe}$ , 50 Mya comparable with the half-life of  $^{244}\text{Pu}$ , and the ages of the end-Devonian extinction(s)  $\sim 360$  Mya.

and  $^{244}\text{Pu}$ , and the abundance of  $^{247}\text{Cm}$  may not be much smaller than that of  $^{244}\text{Pu}$ , as seen in the right panels of Fig. 8 and in Table 4. The ratios  $^{93}\text{Zr}/^{244}\text{Pu}$ ,  $^{107}\text{Pd}/^{244}\text{Pu}$ ,  $^{129}\text{I}/^{244}\text{Pu}$ ,  $^{135}\text{Cs}/^{244}\text{Pu}$  and  $^{182}\text{Hf}/^{244}\text{Pu}$  could be particularly useful for discriminating between models, followed by  $^{236}\text{U}/^{244}\text{Pu}$  and  $^{237}\text{Np}/^{244}\text{Pu}$ .

We do, however, note that there are considerable variations in the isotope ratios calculated using different nuclear models. In making comparisons, we have used the  $\beta$ -decay rates from Marketin et al. (2016), and the HFB model from Goriely et al. (2009), which assumes different nuclear masses, in addition to the baseline calculation. We have noted in brackets in Table 4 the ranges of isotope ratios  $\sigma$  found in all the models SA, SB, KA and KB.<sup>6</sup> The absolute abundances of  $^{129}\text{I}$  and lighter isotopes are relatively insensitive to the model used, so the uncertainties in their ratios to  $^{244}\text{Pu}$  are largely due to those in the  $^{244}\text{Pu}$  yield, and hence correlated. Likewise, the abundances of the isotopes heavier than  $^{236}\text{U}$  relative to that of  $^{244}\text{Pu}$  vary over ranges similar to that quoted in Table 4 for  $^{236}\text{U}/^{244}\text{Pu}$ .

We recall also that only a fraction of the reported  $^{244}\text{Pu}$  may be associated with the  $^{60}\text{Fe}$  deposition peak, with the remainder being due to one or more earlier astrophysical events. In this case it is natural to compare abundances on a time-scale of  $\sim 50$  Myr that is comparable with the half-life of  $^{244}\text{Pu}$ , corresponding to the central vertical lines in the right panels of Fig. 8. On this time scale, as seen in this Figure and in Table 5, the most interesting remaining isotopes are  $^{107}\text{Pd}$ ,  $^{129}\text{I}$ ,  $^{182}\text{Hf}$ ,  $^{236}\text{U}$  and  $^{244}\text{Pu}$ , with the first three providing the greatest discriminating power, albeit with similar nuclear model uncertainties to those discussed above (not shown).

Finally, after 360 Mya, corresponding to the age of the end-Devonian mass extinctions, the  $^{244}\text{Pu}$  abundance would have decreased by an order of magnitude, relatively few radioisotopes would have survived, and only uranium isotopes,

<sup>6</sup> There are similar uncertainties fractions in the abundance ratios at later times after  $\sim 1$  Myr, which are omitted for clarity in the corresponding Tables.

**Table 4.**  $r$ -process isotope ratios after 3 Myr, corresponding to an event near the end of the Pliocene era, together with their uncertainty ranges  $\sigma$  due to the different nuclear models adopted (HFB masses from [Goriely et al. \(2009\)](#) and  $\beta$ -decay rates from [Marketin et al. \(2016\)](#) for both SN and KN models, as well as fission yields from [Kodama & Takahashi \(1975\)](#) for KN models), in addition to the baseline calculations in the  $r$ -process simulations.

Radioisotope Ratio	Supernova Model		Kilonova Model	
	SA	SB	KA	KB
$^{60}\text{Fe}/^{244}\text{Pu}$	$9.2 \times 10^{-2}$	$5.3 \times 10^3$	$2.3 \times 10^{-3}$	$1.1 \times 10^{-5}$
$\sigma(^{60}\text{Fe}/^{244}\text{Pu})$	$9.2 \times 10^{-2} - 5.6 \times 10^2$	$25 - 3.5 \times 10^5$	$1.4 \times 10^{-3} - 1.3 \times 10^{-2}$	$(1.1 - 4.0) \times 10^{-5}$
$^{93}\text{Zr}/^{244}\text{Pu}$	5.2	$8.2 \times 10^4$	4.8	0.15
$\sigma(^{93}\text{Zr}/^{244}\text{Pu})$	$5.2 - 2.4 \times 10^4$	$93 - 4.3 \times 10^6$	0.59 - 14	0.15 - 0.97
$^{107}\text{Pd}/^{244}\text{Pu}$	52	$1.3 \times 10^5$	7.5	0.69
$\sigma(^{107}\text{Pd}/^{244}\text{Pu})$	$50 - 2.0 \times 10^5$	$3.4 \times 10^2 - 1.7 \times 10^6$	2.4 - 7.5	0.69 - 1.5
$^{129}\text{I}/^{244}\text{Pu}$	$3.2 \times 10^2$	$1.7 \times 10^6$	89	19
$\sigma(^{129}\text{I}/^{244}\text{Pu})$	$2.8 \times 10^2 - 7.3 \times 10^5$	$3.8 \times 10^3 - 2.4 \times 10^7$	46 - 89	19 - 38
$^{135}\text{Cs}/^{244}\text{Pu}$	5.4	$1.2 \times 10^5$	0.33	1.4
$\sigma(^{135}\text{Cs}/^{244}\text{Pu})$	$5.4 - 1.9 \times 10^4$	$1.2 \times 10^2 - 4.1 \times 10^6$	0.33 - 1.4	0.30 - 3.9
$^{182}\text{Hf}/^{244}\text{Pu}$	3.1	$4.4 \times 10^3$	0.71	0.11
$\sigma(^{182}\text{Hf}/^{244}\text{Pu})$	$3.1 - 2.6 \times 10^4$	$8.7 - 6.8 \times 10^4$	0.71 - 9.0	0.11 - 2.3
$^{232}\text{Th}/^{244}\text{Pu}$	1.5	11	1.2	0.43
$\sigma(^{232}\text{Th}/^{244}\text{Pu})$	0.23 - 6.0	0.31 - 16	0.36 - 1.2	0.27 - 0.63
$^{235}\text{U}/^{244}\text{Pu}$	1.6	7.0	1.9	0.99
$\sigma(^{235}\text{U}/^{244}\text{Pu})$	1.2 - 7.2	2.0 - 21	1.4 - 4.6	0.99 - 1.7
$^{236}\text{U}/^{244}\text{Pu}$	1.8	9.5	2.0	1.1
$\sigma(^{236}\text{U}/^{244}\text{Pu})$	1.2 - 4.1	2.0 - 9.5	1.2 - 2.5	0.79 - 1.1
$^{238}\text{U}/^{244}\text{Pu}$	2.1	5.4	2.5	1.8
$\sigma(^{238}\text{U}/^{244}\text{Pu})$	2.1 - 3.2	3.2 - 6.9	2.0 - 2.7	1.7 - 1.8
$^{237}\text{Np}/^{244}\text{Pu}$	0.66	1.6	0.78	0.53
$\sigma(^{237}\text{Np}/^{244}\text{Pu})$	0.66 - 1.9	1.0 - 2.6	0.78 - 1.9	0.53 - 2.0
$^{242}\text{Pu}/^{244}\text{Pu}$	$5.3 \times 10^{-3}$	$6.2 \times 10^{-3}$	$6.0 \times 10^{-3}$	$5.2 \times 10^{-3}$
$\sigma(^{242}\text{Pu}/^{244}\text{Pu})$	$(5.3 - 6.7) \times 10^{-3}$	$(6.2 - 8.8) \times 10^{-3}$	$(5.0 - 6.1) \times 10^{-3}$	$(5.0 - 5.6) \times 10^{-3}$
$^{247}\text{Cm}/^{244}\text{Pu}$	0.50	0.45	0.50	0.46
$\sigma(^{247}\text{Cm}/^{244}\text{Pu})$	0.48 - 0.87	0.24 - 0.90	0.62 - 1.2	0.46 - 1.4
$^{248}\text{Cm}/^{244}\text{Pu}$	$1.9 \times 10^{-3}$	$2.1 \times 10^{-3}$	$1.6 \times 10^{-3}$	$1.9 \times 10^{-3}$
$\sigma(^{248}\text{Cm}/^{244}\text{Pu})$	$(1.3 - 1.9) \times 10^{-3}$	$(1.0 - 2.1) \times 10^{-3}$	$(1.5 - 2.3) \times 10^{-3}$	$(1.9 - 2.2) \times 10^{-3}$

$^{232}\text{Th}$  and  $^{129}\text{I}$  might have abundances comparable to  $^{244}\text{Pu}$ , as seen in Table 6. Measurements of  $^{129}\text{I}$  should be able to distinguish between supernova models, but not other radioisotopes.

The results of analogous calculations for the kilonova models KA and KB are shown in the upper and lower panels of Fig. 9, respectively, with yields  $Y$  in the left panels and the ratios  $Y/Y(^{244}\text{Pu})$  in the right panels. As seen in this Figure and in Table 4, the radioisotopes  $^{93}\text{Zr}$ ,  $^{107}\text{Pd}$ ,  $^{129}\text{I}$ ,  $^{135}\text{Cs}$ ,  $^{182}\text{Hf}$ ,  $^{236}\text{U}$ ,  $^{237}\text{Np}$ ,  $^{244}\text{Pu}$  and  $^{247}\text{Cm}$  are again the most promising potential signatures after 3 Myr, with  $^{93}\text{Zr}$ ,  $^{107}\text{Pd}$ ,  $^{129}\text{I}$  and  $^{182}\text{Hf}$  offering the greatest discriminating power between kilonova models, and also between them and the supernova models. After 50 Myr, as seen in Table 5, the most promising radioisotopes for detection are  $^{129}\text{I}$  and  $^{236}\text{U}$ . However,  $^{236}\text{U}$  offers little discriminating power between the different kilonova models, nor between the supernova and kilonova models. After 360 Myr, as also seen in Fig. 9 and in Table 6, the best prospects for detection are again offered by  $^{236}\text{U}$ , which does not discriminate among the KN and SN models. We do not consider  $^{232}\text{Th}$  and  $^{238}\text{U}$  to be promising search targets, in view of their long half-lives and the consequent large backgrounds from events before the formation of the Solar System.

The results of our calculations of interesting abundances after 100 kyr, 3 Myr and 7 Myr (also 50 Myr for KN models) for the different astrophysical  $r$ -process models described in Table 2 are summarized in Fig. 10, which shows scatter

**Table 5.** *r*-Process Isotope Ratios after 50 Myr

Radioisotope Ratio	Supernova Model		Kilonova Model	
	SA	SB	KA	KB
$^{60}\text{Fe}/^{244}\text{Pu}$	$5.9 \times 10^{-7}$	$3.2 \times 10^{-2}$	$1.4 \times 10^{-8}$	$6.6 \times 10^{-11}$
$^{93}\text{Zr}/^{244}\text{Pu}$	$1.5 \times 10^{-7}$	$2.0 \times 10^{-4}$	$1.2 \times 10^{-8}$	$3.8 \times 10^{-10}$
$^{107}\text{Pd}/^{244}\text{Pu}$	0.53	$1.3 \times 10^3$	$7.6 \times 10^{-2}$	$6.9 \times 10^{-3}$
$^{129}\text{I}/^{244}\text{Pu}$	60	$3.3 \times 10^5$	17	3.5
$^{135}\text{Cs}/^{244}\text{Pu}$	$2.0 \times 10^{-10}$	$4.5 \times 10^{-6}$	$1.2 \times 10^{-11}$	$5.4 \times 10^{-11}$
$^{182}\text{Hf}/^{244}\text{Pu}$	0.12	$1.7 \times 10^2$	0.028	$4.4 \times 10^{-3}$
$^{232}\text{Th}/^{244}\text{Pu}$	4.6	28	4.2	2.1
$^{235}\text{U}/^{244}\text{Pu}$	2.9	11	3.4	2.0
$^{236}\text{U}/^{244}\text{Pu}$	0.93	3.8	1.0	0.68
$^{238}\text{U}/^{244}\text{Pu}$	3.2	8.1	3.8	2.6
$^{247}\text{Cm}/^{244}\text{Pu}$	$9.3 \times 10^{-2}$	$8.4 \times 10^{-2}$	$9.2 \times 10^{-2}$	$8.5 \times 10^{-2}$

**Table 6.** *r*-Process Isotope Ratios after 360 Mya, corresponding to the time since the end-Devonian mass extinction(s).

Radioisotope Ratio	Supernova Model		Kilonova Model	
	SA	SB	KA	KB
$^{129}\text{I}/^{244}\text{Pu}$	$4.1 \times 10^{-3}$	30	$1.3 \times 10^{-3}$	$2.3 \times 10^{-4}$
$^{232}\text{Th}/^{244}\text{Pu}$	85	$4.4 \times 10^2$	81	49
$^{235}\text{U}/^{244}\text{Pu}$	30	$1.1 \times 10^2$	34	20
$^{236}\text{U}/^{244}\text{Pu}$	0.41	0.42	0.41	0.41
$^{238}\text{U}/^{244}\text{Pu}$	41	$1.0 \times 10^2$	48	33

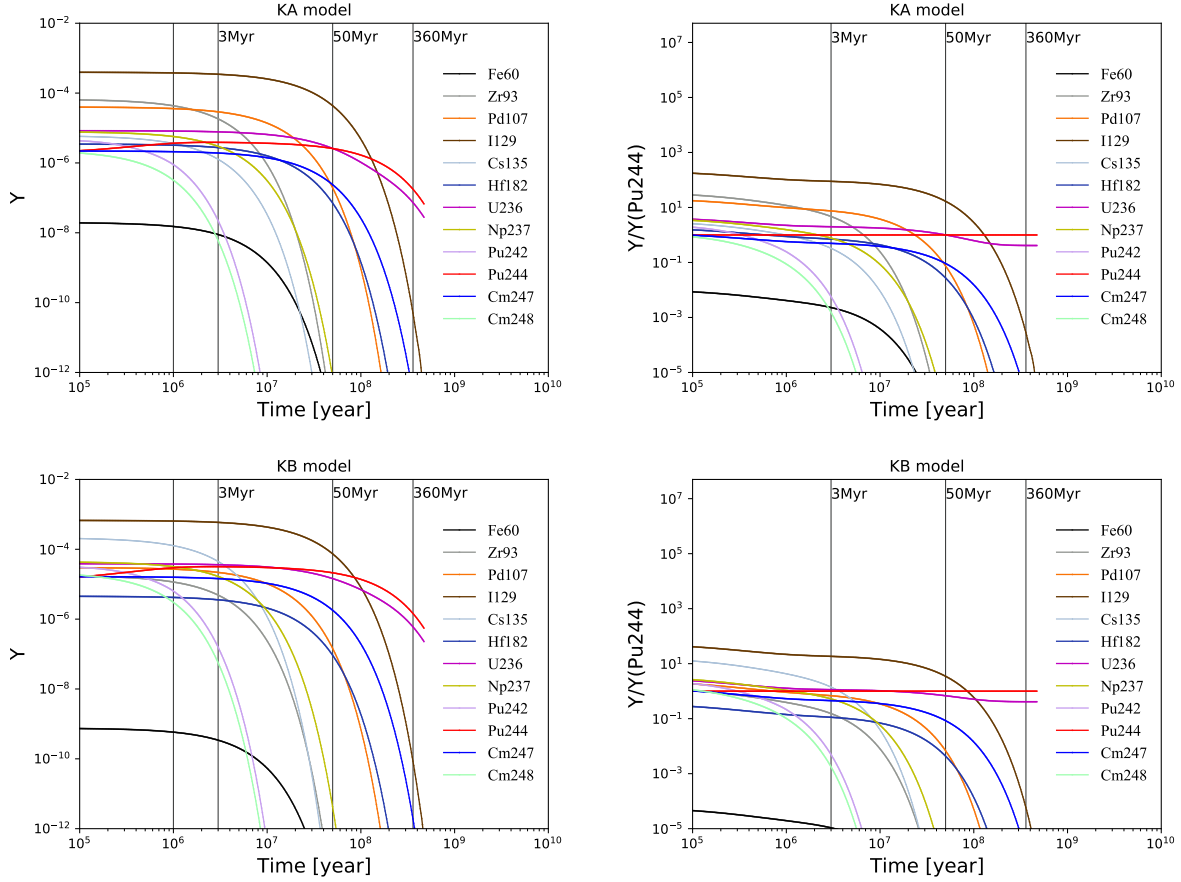
plots of the isotope abundance ratios of  $^{93}\text{Zr}$ ,  $^{107}\text{Pd}$ ,  $^{129}\text{I}$ ,  $^{135}\text{Cs}$ ,  $^{182}\text{Hf}$ , and  $^{247}\text{Cm}$  over  $^{244}\text{Pu}$  versus  $^{60}\text{Fe}/^{244}\text{Pu}$ . The asymmetric uncertainty bars reflect the ranges of microphysics uncertainties shown in Table 4.

Figure 10 shows that the ratios of all these isotopes relative to  $^{244}\text{Pu}$  are highest in the SB SN model. However, the ordering of the abundance ratios of the other isotopes in the different models is not universal, with model SA being lowest for  $^{236}\text{U}/^{244}\text{Pu}$  and  $^{247}\text{Cm}$ , whereas KB is lowest for  $^{93}\text{Zr}$ ,  $^{107}\text{Pd}$ ,  $^{129}\text{I}$  and  $^{182}\text{Hf}/^{244}\text{Pu}$ . These and other differences between the model predictions offer prospects for distinguishing between the different *r*-process models by measurements in deposits up to 50 Myr old.

We note that the predicted ratios in Table 2 and Fig. 10 are for *r*-process production only. For the KN models, this should be indicative of the typical ejected yields for these explosions. On the other hand, for the SN models there will be additional production of some species due to other processes, as summarized in Table 1. For example,  $^{60}\text{Fe}$  production in hydrostatic and explosive burning will far exceed that made in any SN *r*-process, and  $^{93}\text{Zr}$  may also be produced through proton-rich nucleosynthesis in SNe. Thus for species like  $^{60}\text{Fe}$  and  $^{93}\text{Zr}$ , the ratios to  $^{244}\text{Pu}$  in the SN models should be viewed as *lower limits*.

The vertical shaded band in Fig. 10 shows the lower limit to the isotope ratio  $^{60}\text{Fe}/^{244}\text{Pu}$  based on  $^{60}\text{Fe}$  crust data and the  $^{244}\text{Pu}$  deep-ocean sediment measurements due to Wallner et al. (2015). Thus, as discussed in Section 5.2, comparing this lower limit to the  $^{60}\text{Fe}/^{244}\text{Pu}$  ratio from our calculations excludes the KN models, if the radioisotope delivery is a one-step process.

We comment in passing that, as reported in Côté et al. (2021), the nearby event may also be constrained by the  $^{129}\text{I}/^{247}\text{Cm}$  ratio. This ratio maintains a constant value for  $\sim$  Myr following the *r*-process event, because  $^{129}\text{I}$  and  $^{247}\text{Cm}$  have similar half-lives. Côté et al. (2021) points that the measured meteoritic value of  $^{129}\text{I}/^{247}\text{Cm}$  ( $438 \pm 184$ ) favors moderate neutron-rich conditions as in the KN disk wind over the KN dynamical ejecta or MHD SN. We find that our calculation for the MHD SN SB model is consistent with the results of Côté et al. (2021) and Reichert et al. (2021), which are orders of magnitude higher than the meteoritic value of  $^{129}\text{I}/^{247}\text{Cm}$ , while our calculations for the combined KN model KA and SN model SA are quite consistent with the measured data (within a factor of 2).



**Figure 9.** Time evolutions of the abundances  $Y$  (left) and ratios  $Y/Y(^{244}\text{Pu})$  (right) of  $r$ -process nuclei of interest from kilonovae models KA (top) and KB (bottom). The vertical lines correspond to the age of the supernova explosion  $\sim 3$  Mya attested by discoveries of deposits of  $^{60}\text{Fe}$ ,  $\sim 50$  Mya comparable with the half-life of  $^{244}\text{Pu}$ , and the time since the end-Devonian extinction(s)  $\sim 360$  Mya.

Having surveyed  $r$ -process radioisotope production in SNe and KNe, we now turn to the prospects for searches in deep-ocean deposits and in the lunar regolith.

## 5. OBSERVABLES: SEARCHING FOR EXPLOSION EJECTA ON THE EARTH AND MOON

The Earth and Moon serve as natural archives that store any debris from nearby explosions that reach within 1 au from the Sun. This provides a great opportunity to bring samples of ejecta to the laboratory and analyze their content, which can be realized after finding suitable deposition sites and favorable samples by then identifying the signals within them. Live radioisotopes have the advantage of minimizing the natural background, which may render the search possible, even if the measurements remain difficult. As noted in Eqs. (1) - (3) and the surrounding discussion, the three timescales of particular interest are  $\sim (3, 50, 360)$  Mya, corresponding to the observed  $^{60}\text{Fe}$  pulse, the  $^{244}\text{Pu}$  half-life (approximately), and the end of the Devonian epoch.

A challenge common to terrestrial and lunar searches is the tiny abundance of any radioisotope that we seek. As discussed above, the  $r$ -process components of any reasonable signal are expected to have fluences smaller than the established  $^{60}\text{Fe}$  signal, implying that only accelerator mass spectrometry (AMS) techniques may have the needed sensitivity. At present,  $^{60}\text{Fe}$  measurements can find isotope fractions with a sensitivity down to  $^{60}\text{Fe}/\text{Fe} \sim (0.3 - 1) \times 10^{-16}$  (Wallner et al. 2020). However, this sensitivity may be impaired in the cases of isotopes with a significant cosmic-ray-induced background. For example, in the case of the recently-reported evidence for terrestrial deposition of  $^{53}\text{Mn}$ , the apparent excess of the signal over background is  $^{53}\text{Mn}/\text{Mn} \sim 1.5 \times 10^{-14}$  (Korschinek et al. 2020).

When a natural terrestrial background is absent or small, AMS sensitivities are often limited by the ability to remove an interfering stable isobar with the same  $A$  and thus nearly the same mass as the species of interest; this is important for many of the  $r$ -process radioactivities that have stable isotopes. Recent advances suggest that it is possible to

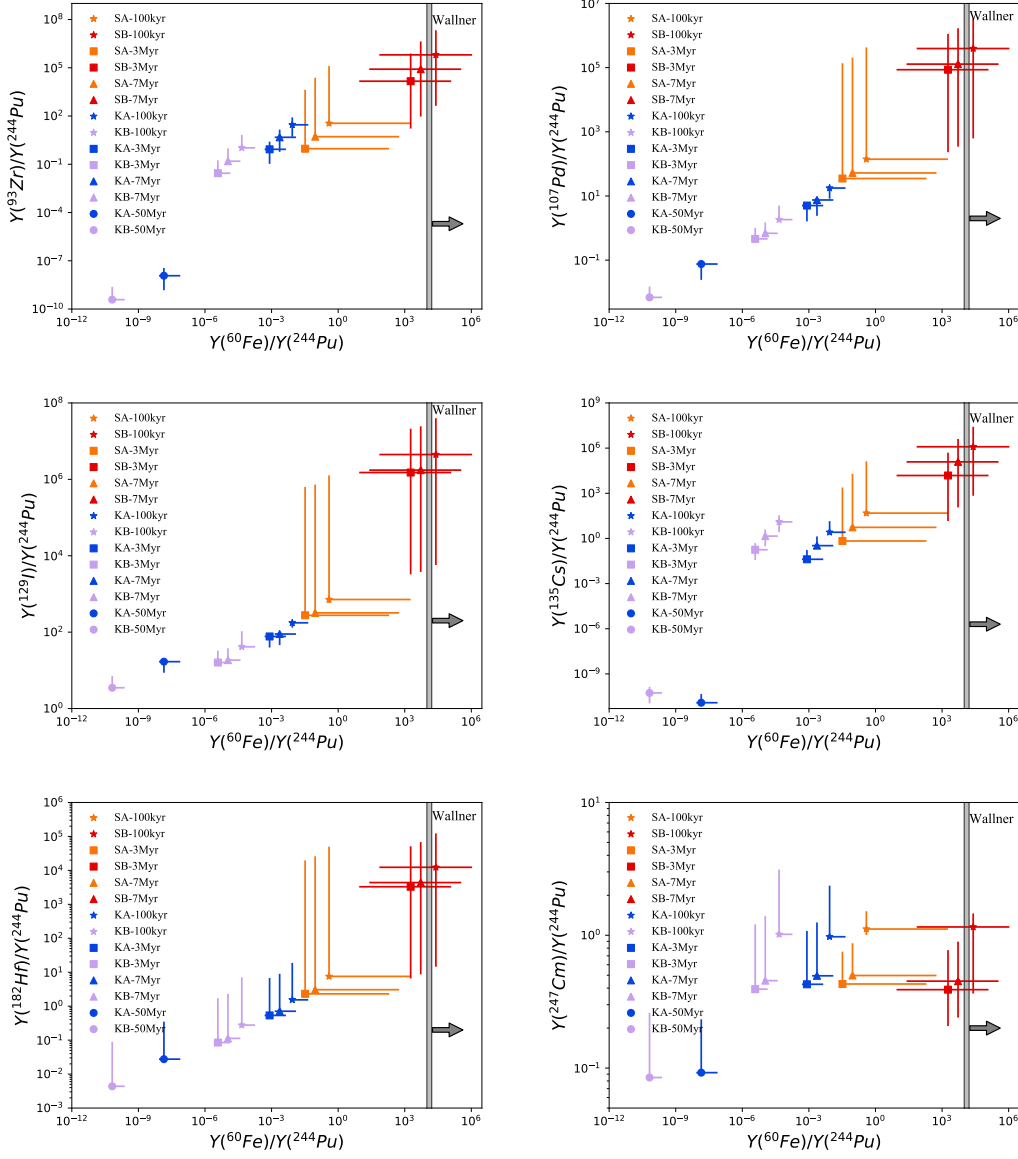


**Figure 10.** Scatter plots of the isotope abundance ratios of  $^{93}\text{Zr}$ ,  $^{107}\text{Pd}$ ,  $^{129}\text{I}$ ,  $^{135}\text{Cs}$ ,  $^{182}\text{Hf}$ , and  $^{247}\text{Cm}/^{244}\text{Pu}$  versus  $^{60}\text{Fe}/^{244}\text{Pu}$  after times 100 kyr, 3 Myr and 7 Myr (also 50 Myr for the kilonovae models KA and KB), as calculated with the different astrophysical r-process models described in Table 2. The points are the isotope ratios obtained from the baseline r-process calculations, the error bars denote the variations due to the different set of nuclear models (HFB masses from Goriely et al. (2009) or  $\beta$ -decay rates from Marketin et al. (2016) for both SN and KN models, or fission yields from Kodama & Takahashi (1975) for KN models, in addition to the baseline nuclear data) adopted in r-process. Note that the isotope ratios presented here are only from the r-process nucleosynthesis, for supernovae,  $^{60}\text{Fe}$  is mainly produced in the pre-SN stage and through explosive nucleosynthesis, thus the isotope ratios of  $^{60}\text{Fe}/^{244}\text{Pu}$  in the plot are actually the lower limit for SN models SA and SB. The shaded band is the lower limit of the measured isotope ratio of  $^{60}\text{Fe}/^{244}\text{Pu}$  from Wallner et al. (2015).

reach  $^{93}\text{Zr}/^{92}\text{Zr} \sim 6 \times 10^{-11}$  (Pavetich et al. 2019; Hain et al. 2018); this hinges on successful removal of the stable isobar  $^{93}\text{Nb}$ . In the case of  $^{107}\text{Pd}$ , Korschinek et al. (1994) report an AMS sensitivity  $^{107}\text{Pd}/^{106}\text{Pd} \sim 10^{-8}$ ; here the interfering stable isobar is  $^{107}\text{Ag}$ . In the case of  $^{129}\text{I}$  there is a natural background level  $^{129}\text{I}/^{127}\text{I} \sim 1.5 \times 10^{-12}$  (Ji et al. 2015b). Sensitivities down to  $^{129}\text{I}/^{127}\text{I} \lesssim 10^{-14}$  are possible (Vockenhuber et al. 2015) since the interfering stable isobar  $^{129}\text{Xe}$  is an inert gas, fortuitously, and does not form negative ions, and so will not interfere. In the case of  $^{135}\text{Cs}$ , Yin et al. (2015) are able to reduce stable isobar contamination to  $^{135}\text{Ba}/^{133}\text{Cs} \sim 9 \times 10^{-12}$ , and we will adopt the same value for the prospective sensitivity to  $^{135}\text{Cs}$ , namely  $^{135}\text{Cs}/^{133}\text{Cs} \sim 9 \times 10^{-12}$ . In the case of  $^{182}\text{Hf}$ , Vockenhuber et al. (2004) report a sensitivity  $^{182}\text{Hf} + ^{182}\text{W}/^{180}\text{Hf} \sim 10^{-11}$ ; the ability to measure  $^{182}\text{Hf}/^{180}\text{Hf}$  to this

precision or better requires that techniques be developed to suppress further the stable isobar  $^{182}\text{W}$ . In the case of  $^{236}\text{U}$ , there are no isobaric contaminants, and the detection limits are set by the ability to discriminate the neighboring abundant uranium isotopes  $^{235}\text{U}$  and  $^{238}\text{U}$ . Efforts by [Wilcken et al. \(2008\)](#) estimate a detection limit of  $^{236}\text{U}/^{238}\text{U} \sim 10^{-13}$ .

In the cases of  $^{237}\text{Np}$ ,  $^{244}\text{Pu}$ , and  $^{247}\text{Cm}$ , there are no stable isotopes nor isobars, so searches can first focus simply on extracting the element, guarding against anthropogenic contamination. In addition, AMS samples must be spiked with shorter-lived isotopes of each species in order to calibrate the response. Both  $^{236}\text{Pu}$  and  $^{242}\text{Pu}$  have been used as calibration standards for  $^{244}\text{Pu}$  ([Wallner et al. 2004](#); [Raisbeck et al. 2007](#); [Wallner et al. 2015](#)). The other species have been studied less. In the case of  $^{237}\text{Np}$ , sector field Inductively Coupled Plasma Mass Spectrometry (ICP-MS) studies have sensitivities down to a mass fraction  $10^{-15}$  g/g within soil and sediment samples ([Röllin et al. 2009](#)), while systematic AMS studies suggest sub fg per sample detection limits as long as the  $^{238}\text{U}$  content remains sufficiently low ([Fifield et al. 1997](#); [López-Lora & Chamizo 2019](#)). Initial AMS studies of  $^{247}\text{Cm}$  made by [Christl et al. \(2014\)](#) suggest a detection limit of  $<0.1$  fg in a typical sample where limits were set by the impurities of the  $^{244}\text{Cm}$  spike added for reference.

### 5.1. Plutonium Measurements

We anchor our predictions for prospective  $r$ -process radioisotopes using the results of geological searches for  $^{244}\text{Pu}$  in deep-ocean crusts and sediments that are displayed in [Fig. 11](#) and are summarized in [Table 7](#).<sup>7</sup> An upper limit of  $0.2$   $^{244}\text{Pu}$  atoms/cm<sup>2</sup>/y on the rate of extraterrestrial deposition in young sediment was set by [Paul et al. \(2001\)](#). Subsequently, AMS measurements of crust VA13-2 by [Wallner et al. \(2004\)](#) and of sediment MD90-0940 by [Raisbeck et al. \(2007\)](#) each yielded one event, dated to 1 – 14 Mya and 2.4 – 2.7 Mya, respectively. [Raisbeck et al. \(2007\)](#) do not attribute their single event to a signal, but derive upper limits on the fluence assuming one count in each of three time bins. We follow this practice, noting that the flux inferred from the nonzero bin would vastly exceed the other limits and detections overlapping this time period. More recently, a search for  $^{244}\text{Pu}$  by [Wallner et al. \(2015\)](#) yielded a possible signal in three samples corresponding to three different epochs: sediments spanning 0.53 – 2.17 Mya, and crust layers at 5 – 12 Mya and 12 – 25 Mya.

In each of these samples, at most only a single  $^{244}\text{Pu}$  count was found in each time bin, so these results must be treated with great caution. On the other hand, there is no stable isobar at mass 244, and both [Wallner et al. \(2015\)](#) and ([Paul et al. 2001](#)) find that the anthropogenic  $^{244}\text{Pu}$  abundance in the top layers of ocean sediments is small. Moreover, it is remarkable that four different groups have searched for  $^{244}\text{Pu}$ , and two independent studies have found events they regard as detections. This may represent sort of consistency check, or could indicate an as-yet unknown systematic common to all measurements.

The detections reported in [Fig. 11](#) and [Table 7](#) are not significant individually, but they amount cumulatively to intriguing evidence of  $^{244}\text{Pu}$  deposition by one or more astrophysical explosions. Taking the measurements at face value, it would seem that the  $^{244}\text{Pu}$  flux history differs from that of  $^{60}\text{Fe}$ . The  $^{244}\text{Pu}$  flux extends from nearly the present back to at least 12 to 25 Mya and, within the large uncertainties, it is unclear if the flux varies over this time. The data could accommodate—but within uncertainties do not demand—a larger flux around the time of the  $^{60}\text{Fe}$  pulse(s) at  $\sim 3$  (and  $\sim 7$  Mya). In contrast, the established  $^{60}\text{Fe}$  pulse is confined to a time window  $< 3$  Mya, though there are indications of  $^{60}\text{Fe}$  deposition both before and after this peak. The difference between the  $^{60}\text{Fe}$  and  $^{244}\text{Pu}$  deposition histories suggests a different origin for at least some of the  $^{244}\text{Pu}$ , a point also made in previous studies, e.g., [Wallner et al. \(2015\)](#).

It is nevertheless interesting to focus on the window at roughly 1.6 – 3.2 Mya shown in [Fig. 11](#), which overlaps with the peak in  $^{60}\text{Fe}$  crust detections. We interpret the  $^{244}\text{Pu}$  data from this epoch as corresponding to a flux

$$\Phi^{\text{interstellar}}(^{244}\text{Pu}) = 3000 \text{ atoms cm}^{-2} \text{ Mya}^{-1}, \quad (7)$$

namely the level reported in sediments by [Wallner et al. \(2015\)](#), which is consistent with the detection by [Wallner et al. \(2004\)](#).

In order to make predictions for measurements of radioisotopes  $i$  like  $^{244}\text{Pu}$  we need, in addition to  $Y_i(t)$  obtained from the network calculation, estimates of the total  $r$ -process yields or ejected mass  $M_{\text{ej}}$  from our SN and KN models,

<sup>7</sup> We note that also [Hoffman et al. \(1971\)](#) reported a signal in Precambrian bastnäsite, but this claim was not confirmed subsequently by [Lachner et al. \(2012\)](#).

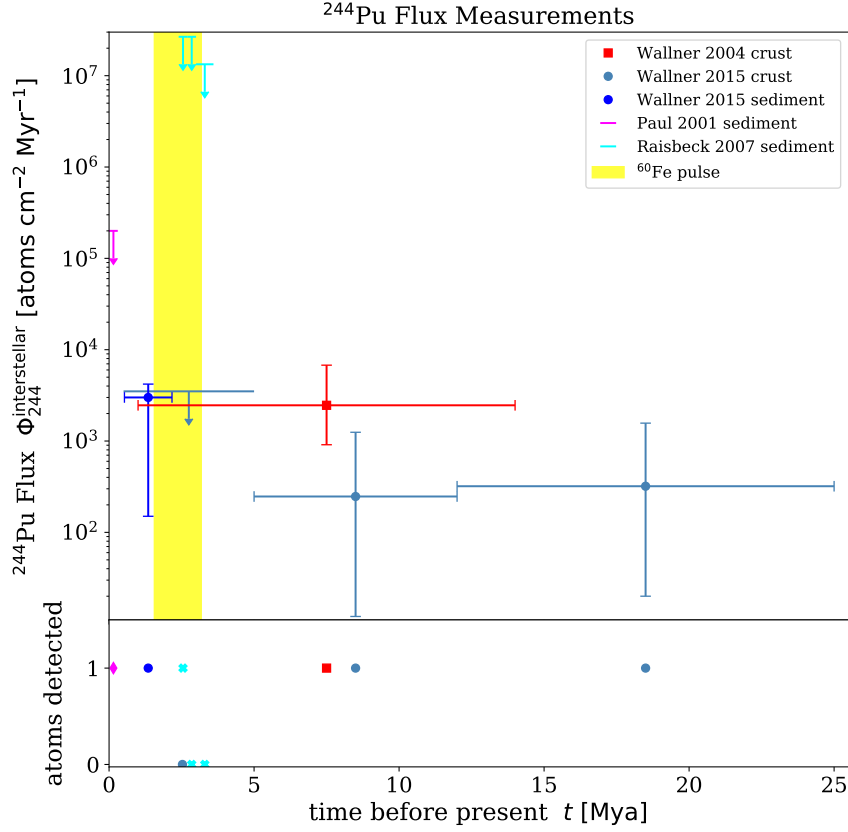


**Figure 11.** Geological searches for  $^{244}\text{Pu}$ , in deep-ocean crusts (Wallner et al. 2004, 2015) and sediments (Paul et al. 2001; Raisbeck et al. 2007; Wallner et al. 2015). Bottom panel:  $^{244}\text{Pu}$  counts, either one or zero. Top panel: Interstellar  $^{244}\text{Pu}$  flux, expressed as a measurement when count is nonzero, and a limit for zero counts and for the first (Raisbeck et al. 2007) time bin as described in the text.

**Table 7.** Geological Searches for Natural  $^{244}\text{Pu}$

Study	Sample	Time [Mya]	$^{244}\text{Pu}$ Counts [atoms]	Flux $\Phi_{244}^{\text{interstellar}}$ [atoms $\text{cm}^{-2} \text{Myr}^{-1}$ ]	Fluence $\mathcal{F}_{244}^{\text{interstellar}}$ [atoms $\text{cm}^{-2}$ ]
Paul et al. (2001)	Sediment 92SAD01	0 – 0.3	1*	$< 2 \times 10^5$	$< 2 \times 10^4$
Wallner et al. (2004)	Crust VA13-2	1–14	1	2500	$1.6 \times 10^4$
Raisbeck et al. (2007)	Sediment MD90-0940	2.4–2.7	1	$< 3 \times 10^7$	$< 3 \times 10^6$
Wallner et al. (2015)	Crust 273KD	0.5–5	0	$< 3500$	$< 800$
		5–12	1	$247_{-235}^{+1000}$	
		12–25	1	$320_{-300}^{+1250}$	
	Sediment TR149-217	0.53–2.17	1	$3000_{-850}^{+12000}$	

\*Paul et al. (2001) argue that their detection could be due to anthropogenic contamination.

from which we can obtain the absolute yield for the radioisotope  $i$  at time  $t$ , namely  $M_i(t) = M_{\text{ej}} \times X_i(t)$ . The nucleosynthetic outcome of our SA model is similar to the  $2.2 M_{\odot}$  neutrino-driven wind model from Wanajo (2013), where a total yield of  $1.37 \times 10^{-5} M_{\odot}$  is reported; estimates of the mass ejected in SN neutrino-driven winds vary from  $1 \times 10^{-5}$  to  $5 \times 10^{-4} M_{\odot}$  (see, e.g., Wanajo et al. 2001; Argast et al. 2004). The yield from the MHD supernova

simulation we adopt for our SB model is  $\sim 0.03M_{\odot}$  (Mösta et al. 2018b), while a wide range of MHD SN yields are found in the literature, from  $6.72 \times 10^{-3}M_{\odot}$  in Winteler et al. (2012) to  $\sim 0.389M_{\odot}$  in Reichert et al. (2021). For the KN models, the yield from our chosen Bovard et al. (2017) dynamical ejecta simulation is about  $3.53 \times 10^{-3}M_{\odot}$ , which is roughly consistent with the yields in, e.g., Radice et al. (2018) of  $\sim 2 \times 10^{-3}M_{\odot}$ . The disk wind yields from Just et al. (2015) range from  $\sim 7 \times 10^{-3}$  to  $6.68 \times 10^{-2}M_{\odot}$ , similar to the range found in, e.g. (Fernández et al. 2015), of  $\sim 0.03$  to  $0.22M_{\odot}$ . For our KB model, the disk and dynamical ejecta masses are similar, giving a total yield of  $7 \times 10^{-3}M_{\odot}$ , while for our KA model the disk wind mass is roughly four times that of the dynamical ejecta for a total yield of  $1.7 \times 10^{-2}M_{\odot}$ . The theoretical estimates quoted above give ranges for  $r$ -process yields of  $\sim 5 \times 10^{-3} - 0.1M_{\odot}$ , consistent with the values suggested by the observations of GW170817 (Côté et al. 2018).

### 5.2. $^{244}\text{Pu}$ Radioactivity Distance Constraints on an Event 3 Myr Ago

We first consider the possibility that the  $^{244}\text{Pu}$  flux coincident with the  $^{60}\text{Fe}$  pulse is due to the same event. Thus, any  $^{244}\text{Pu}$  flux outside of this timespan must come from another process, such as that explored in the following Section. We also assume that the radioisotope delivery is a *one-step* process, i.e., the terrestrial and lunar deposition of these species is a direct consequence of the propagation of the explosion ejecta.

Within this picture we can infer the  $^{244}\text{Pu}$  yield for a given explosion distance. Integrating over the  $^{60}\text{Fe}$  pulse length  $\Delta t \sim 1$  Myr we find an interstellar fluence  $\mathcal{F}_{60} = 4800$  atoms  $\text{cm}^{-2}$ . For an explosion with isotropic ejecta, we can recover the yield by inverting eq. (4), to find

$$M_{\text{ej}}(^{244}\text{Pu}) = \frac{1}{f_{\text{Pu}}} 4\pi A_{244} m_{\text{u}} r^2 \mathcal{F}_{244} = 10^{-9} M_{\odot} \left( \frac{r}{100 \text{ pc}} \right)^2 \left( \frac{\mathcal{F}_{244}}{4800 \text{ atoms cm}^{-2}} \right). \quad (8)$$

Models of  $^{244}\text{Pu}$  production via the  $r$ -process in a SN explosion suggest a yield of  $\sim 10^{-9}$  solar mass of  $^{244}\text{Pu}$ , with an uncertainty of an order of magnitude. If we assume that the estimated  $^{244}\text{Pu}$  flux is due to a single nearby SN, we can estimate the likely distance of the explosion from Earth, as seen in Fig. 12.

The horizontal orange bands represent the  $^{244}\text{Pu}$  yield found in representative SN calculations with and without MHD effects, cf, models SB and SA above, and the diagonal gray line represents the yield that would be inferred from the estimated  $^{244}\text{Pu}$  flux, which increases as the square of the explosion distance.

Consistency between the two calculations provides an estimate of the SN distance represented by the vertical yellow bands. The resulting estimate is sometimes known as a “radioactivity distance” in recognition of the formal similarity to the luminosity distance. Assuming that most of the  $^{244}\text{Pu}$  is incorporated into dust,  $f_{\text{dust}}^{\text{Pu}} \simeq 1$ , the central value of the estimate in the MHD model is  $\sim 100$  pc, with an uncertainty of about an order of magnitude in either direction. The *modified* neutrino-driven wind model has somewhat larger yields and thus requires larger distances, but within uncertainties the distance range overlaps with the MHD model. These are quite consistent with the explosion distance inferred for a SN that could have generated the well-established  $^{60}\text{Fe}$  pulse  $\sim 3$  Mya, which is represented by the horizontal double-headed arrow. Within the uncertainties, this distance estimate is also compatible with the distances to the Tucana-Horologium (Tuc-Hor) and Scorpio-Centaurus (Sco-Cen) stellar associations, which have been proposed as possible locations of the SN that generated the  $^{60}\text{Fe}$  pulse. Note that these results assume  $f_{\text{dust}}^{\text{Pu}} \simeq 1$ . Smaller distances follow if we have a smaller value for dust efficiency, as illustrated by the intersection of the dotted diagonal gray and horizontal blue lines.

We now turn to the possibility of a KN as the source of  $^{244}\text{Pu}$  3 Mya. Fig. 12 shows the yields for our KA and KB models, which are  $\sim 6$  orders of magnitude larger than in the supernova models. As a result, they correspond to much larger radioactivity distances  $\gg 1$  kpc. This would place the explosions implausibly far for any ejecta to reach the Earth. Indeed, the upper range of the distance extends beyond the size of our Galactic disk. This suggests a different scenario is needed for the kilonova case, to which we now turn.

### 5.3. $^{244}\text{Pu}$ Constraints on a Kilonova Enrichment of the Local Bubble

We have seen that a KN scenario requires that the  $^{244}\text{Pu}$  was not injected directly from a single event, but instead suggest some form of dilution occurred between the explosion and injection in the solar system. Moreover, we have seen that  $^{244}\text{Pu}$  shows a persistent flux extending over back to as much as 25 Mya, rather than the impulsive signal seen in  $^{60}\text{Fe}$ . This also leads one to consider an  $r$ -process event much earlier than the  $^{60}\text{Fe}$  supernova. The requirements of early  $r$ -process creation and subsequent dilution are both met naturally if a KN exploded prior to or during the early

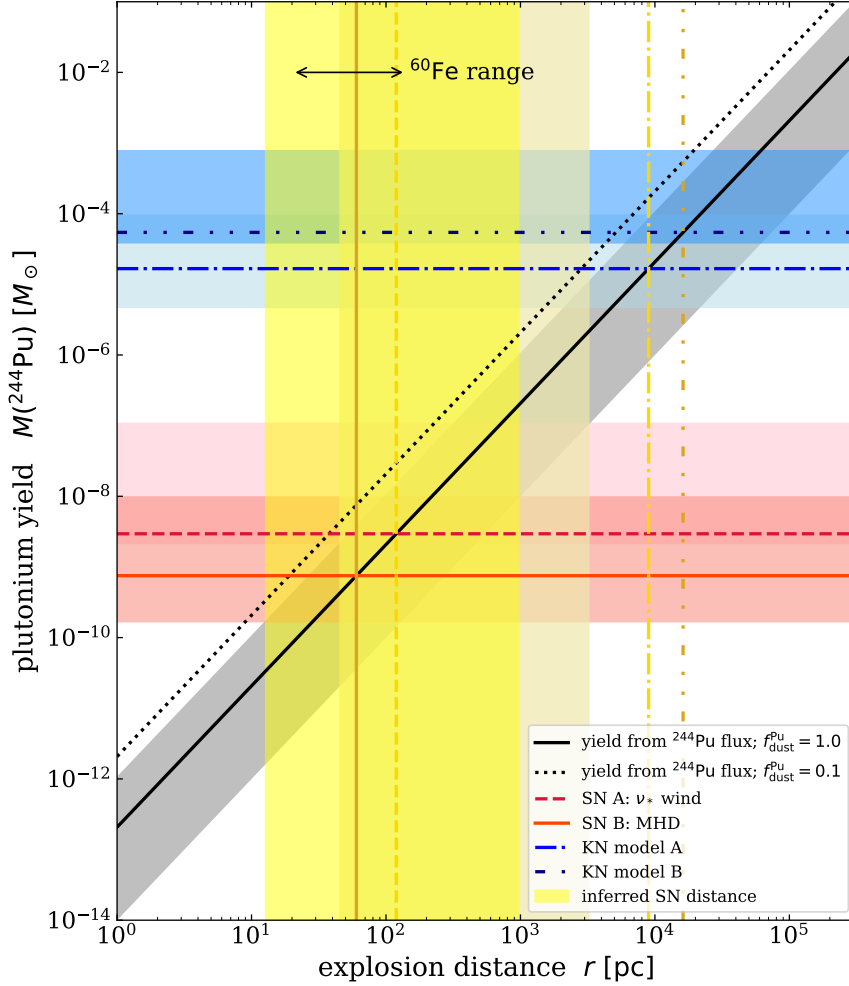


**Figure 12.** Estimation of the explosion distance of a SN 3 Mya that could have generated the  $^{244}\text{Pu}$  flux inferred from the measurements in Table 7, based on calculations of the  $^{244}\text{Pu}$  yield in a SN via the *r*-process. The  $^{244}\text{Pu}$  yield inferred from observations scales with the dust fraction as  $1/f_{\text{dust}}^{\text{Pu}}$ ; we show results for  $f_{\text{dust}}^{\text{Pu}} = 0.1$  and 1. The colored shades represent the uncertainty ranges: those due to the uncertainties in the total ejected masses adopted for SN and KN models are light red for SA, red for SB, light blue for KA and blue for KB; uncertainty in the  $^{244}\text{Pu}$  flux measurement is in grey; yellows indicate the resulting uncertainty ranges in the indicated SN distance for SA and SB.

formation of the Local Bubble, enriching the entire star-forming cloud that gave rise to the bubble. Indeed, Wallner et al. (2015) proposed such a scenario, and here we build on their analysis.

We thus envision a *two-step* process in which the propagation of the kilonova ejecta is followed by mixing in the proto-Local Bubble, and then deposition on Earth. Specifically, we envision the following sequence of events. (a) More than  $\sim 25$  Mya, a KN exploded, ejecting  $^{244}\text{Pu}$ -bearing *r*-process material. (b) Some of the KN ejecta collided with and was mixed into the molecular cloud giving rise to the Local Bubble. (c) Some of the  $^{244}\text{Pu}$  was incorporated into dust grains. (d) The  $^{244}\text{Pu}$ -bearing dust subsequently bombarded the Earth.

A simplified model allows us to estimate the mass  $M_{244}^{\text{LB,dust}}$  of  $^{244}\text{Pu}$  in Local Bubble dust grains. We describe the Local Bubble crudely, as a sphere of radius  $R_{\text{LB}}$ , so that the  $^{244}\text{Pu}$  average number density is  $n_{244} =$

$M_{244}^{\text{LB,dust}}/(4\pi A_{244} m_u R_{\text{LB}}^3/3)$ . Let  $v_{\text{rel}}$  be the speed of the Local Bubble gas relative to the Sun<sup>8</sup>, so that the interstellar <sup>244</sup>Pu number flux is  $\Phi_{244} = n_{244} v_{\text{rel}} \propto M_{244}^{\text{LB,dust}}/R_{\text{LB}}^3$ . Then, given the measured flux  $\Phi_{244}$ , we can infer the mass

$$\begin{aligned} M_{244}^{\text{LB,dust}} &= \frac{4\pi}{3} A_{244} m_u R_{\text{LB}}^3 \frac{\Phi_{244}^{\text{obs}}}{v_{\text{rel}}} \\ &= 10^{-10} M_{\odot} \left( \frac{\Phi_{244}^{\text{obs}}}{3000 \text{ cm}^{-2} \text{ Myr}^{-1}} \right) \left( \frac{R_{\text{LB}}}{50 \text{ pc}} \right)^3 \left( \frac{30 \text{ km/s}}{v_{\text{rel}}} \right). \end{aligned} \quad (9)$$

We see that the <sup>244</sup>Pu inventory is far below the levels of KN yields. This implies that the explosion was not contained in the Local Bubble, but occurred outside it with only a fraction of the yield intercepted by the Local Bubble.

We note that it is likely that kilonova ejecta are unable to form significant amounts of dust, due to their high velocities (Takami et al. 2014; Gall et al. 2017). This is expected as a continuation of the trend in which Type Ia supernovae have smaller or no dust formation compared to core-collapse explosions, which have slower ejecta speeds (Gomez et al. 2012; Nozawa et al. 2011). In light of the need for dust grains to deliver ejecta to Earth, the lack of kilonova dust production argues against direct, one-step deposition of ejecta from these explosions. However, in the two-step model the kilonova ejecta are stopped and mixed into the proto-Local Bubble material and can then be incorporated into dust grains.

We can go further and estimate the distance from the kilonova to the Local Bubble. This is a variant of the radioactivity distance calculation, similar to the Looney et al. (2006) calculation of the supernova injection of radioisotopes into the presolar nebula (see, e.g., Ouellette et al. 2009). Let the kilonova explode at distance  $r_{\text{KN}}$  from the bubble, ejecting a yield  $M_{\text{ej}}(^{244}\text{Pu})$ . If the molecular cloud progenitor of the bubble has radius  $R_{\text{MC}}$ , then the mass intercepted by the bubble and becoming dust is

$$M_{244}^{\text{LB,dust}} = \frac{\pi R_{\text{MC}}^2}{4\pi r_{\text{KN}}^2} f_{244} M_{\text{ej}}(^{244}\text{Pu}), \quad (10)$$

with  $f_{244} < 1$  accounting for the fraction of incident <sup>244</sup>Pu stopped by the bubble and ultimately incorporated into grains. We can then solve for the kilonova distance, finding

$$r_{\text{KN}} = \sqrt{\frac{f_{244} M_{\text{ej}}(^{244}\text{Pu})}{4M_{244}^{\text{LB,dust}}}} R_{\text{MC}} \quad (11)$$

$$= 1500 \text{ pc } f_{244}^{1/2} \left( \frac{M_{\text{ej}}(^{244}\text{Pu})}{10^{-4} M_{\odot}} \right)^{1/2} \left( \frac{10^{-10} M_{\odot}}{M_{244}^{\text{LB,dust}}} \right)^{1/2} \left( \frac{R_{\text{MC}}}{3 \text{ pc}} \right). \quad (12)$$

This places the KN explosion at a more plausible distance, in view of the expectation that KNe are rarer and further between than SNe.<sup>9</sup> We note that a KN is likely to be so distant that its ejecta blast would be weak when arriving in the solar neighbourhood, and hence unlikely to destroy the local molecular cloud.

Estimates of kilonova and neutron star merger rates place consistency checks on our distance calculations (Scalo & Wheeler 2002; Hartmann et al. 2002). The average rate for a KN within distance  $r_{\text{KN}}$  is  $\Gamma(r_{\text{KN}}) \approx \pi r_{\text{KN}}^2 Q_{\text{local}}$  where  $Q_{\text{local}} = dN_{\text{KN}}/dA dt$  is the KN rate per unit area of the Galactic disk at the solar location; we assume  $r_{\text{KN}} > h$ , the scale height of KN progenitors, so that the problem is reduced to two dimensions. Using the usual approximation of an exponential disk with scale radius  $R_0 = 2.9 \text{ kpc}$  (see, e.g., Murphey et al. 2020; Girardi et al. 2005), we have  $Q(R) = \mathcal{R}_{\text{KN}} e^{-R/R_0}/2\pi R_0^2$ , where the total Galactic KN rate sets the normalization via the surface integral  $\mathcal{R}_{\text{KN}} = 2\pi \int Q(R) R dR$ . We estimate the Galactic KN rate assuming the ratio to the Galactic core-collapse SN rate  $\mathcal{R}_{\text{CC}}$  is the same as ratio of the local cosmic rate densities:  $\mathcal{R}_{\text{KN}}/\mathcal{R}_{\text{CC}} = \dot{\rho}_{\text{KN}}/\dot{\rho}_{\text{CC}}$ . Using  $\mathcal{R}_{\text{CC}} \approx 0.032 \text{ yr}^{-1}$  (Adams et al. 2013),  $\dot{\rho}_{\text{CC}} = 1.1 \times 10^{-4} \text{ Mpc}^{-3} \text{ yr}^{-1}$  (Lien & Fields 2009), and a binary neutron star merger rate as a measure of the underlying  $r$ -process source rate  $\dot{\rho}_{\text{BNS}} \gtrsim \dot{\rho}_{\text{KN}} \sim 1500 \text{ Mpc}^{-3} \text{ yr}^{-1}$  (consistent with estimates from Andreoni et al. 2020; Della Valle et al. 2018; Jin et al. 2018; Chruslinska et al. 2018; Andreoni et al. 2021), we find

<sup>8</sup> Note that this relative speed encodes not only the Sun's motion with respect to the cloud's center of mass, but also turbulent motions within the cloud, which have dispersion  $\sigma_v \sim 1 - 10 \text{ km/s}$  for clouds of size  $R_{\text{MC}} \gtrsim 10 \text{ pc}$ .

<sup>9</sup> An incorporation efficiency as small as  $f_{244} \sim 10^{-3}$  can be accommodated and still give a distance comparable to that estimated above for a supernova remnant.

$R_{\text{KN}} \sim 1.4 \times 10^{-2} \mathcal{R}_{\text{SN}} \sim 440 \text{ Myr}^{-1}$ . Finally

$$\Gamma_{\text{KN}} \sim 1.3 \text{ events Myr}^{-1} \left( \frac{r_{\text{KN}}}{1 \text{ kpc}} \right)^2 \quad (13)$$

for the solar location  $R_{\odot} = 8.7 \text{ kpc}$ . We see that the typical KN recurrence time is  $\Gamma_{\text{KN}}^{-1} \sim 0.8 \text{ Myr} (1 \text{ kpc}/r_{\text{KN}})^2$ . Thus KN explosion times of  $t_{\text{KN}} = (10, 50) \text{ Myr}$  correspond to mean distances of  $r_{\text{KN}} = (280, 120) \text{ pc}$ . Our two-step  $^{244}\text{Pu}$ -based radioactivity distances lie comfortably within this range, demonstrating overall consistency.

Two other issues constrain the timing of the KN explosion and subsequent *r*-process rain. One is the timescale for the Local Bubble to assemble and form stars; this timescale plus the  $\lesssim 10 \text{ Myr}$  massive star lifetimes sets an upper limit to the KN injection time. Estimates of lifetimes of molecular clouds span a significant range from local solar neighborhood values of a few Myr (Hartmann et al. 2001) to  $\sim 30 \text{ Myr}$  (Murray 2011). Finally, the *r*-process bombardment on Earth begins only when the Sun enters the Local Bubble. This time is uncertain and depends on the evolving bubble morphology, but also sets an upper limit on the injection time.

We observe that this two-step process incurs larger uncertainties overall than the one-step SN mechanism. One of them is the timing of the KN: the further in the past the greater the losses of shorter-lived species. If the  $^{244}\text{Pu}$  event in the 12.5–25 Mya crust layer is real, it sets a lower limit on this time. The longest-lived *r*-process radioisotopes of interest, apart from  $^{244}\text{Pu}$ , are  $^{129}\text{I}$ ,  $^{182}\text{Hf}$ , and  $^{247}\text{Cm}$ . These live long enough for their production in a KN to be potentially observable in this layer; also the secular equilibrium abundance of  $^{236}\text{U}$  potentially provides a check on anthropogenic sources of actinides.

#### 5.4. Predicting *r*-Process Radioisotope Signatures in Terrestrial Archives

The previous two subsections show that it is possible to construct both SN and KN scenarios for some or all of the  $^{244}\text{Pu}$  signal. We conclude that the  $^{244}\text{Pu}$  flux in eq. (7) could have an astrophysical origin, and use it to normalize our subsequent predictions for possible live isotope searches using AMS techniques. In this Section we compute terrestrial signals for *r*-process radioisotopes, with a particular focus on Fe-Mn crusts.

The available natural terrestrial archives that accumulate gradually over the longest periods of time, and thereby give the most complete dating information, are deep-ocean crusts and sediments. In natural archives of interest, radioisotope abundances are usually presented as isotope fractions  $(N_i/N_j)_{\text{obs}}$ , the ratio of a radioisotope *i* to a stable isotope or element *j*. Here we derive predictions for the ratio  $N_i^{\text{astro}}/N_j^{\text{bg}}$ , i.e., the astrophysical signal relative to a stable “background” isotope.

The astrophysical signal can be expressed as the incident interstellar number flux  $\Phi_i^{\text{interstellar}} = dN_i/dAdt$ , usually given without decay losses included. The measurable flux onto a terrestrial sample is

$$\Phi_i^{\text{sample}} = \frac{f_i U_i}{4} \Phi_i^{\text{interstellar}} e^{-t/\tau_i}, \quad (14)$$

where the factor of 4 accounts for the ratio of the Earth’s cross section to its surface area,  $f_i$  is the fraction of *i* in dust arriving at Earth, and  $U_i$  accounts for “uptake” into the sample. We have also accounted for radioactive decay. If the flux is measured for time  $\Delta t$ , the corresponding surface density in the sample is  $N_i^{\text{astro}} = \Phi_i^{\text{sample}} \Delta t$ .

During this time interval, the sample accumulates a surface mass density  $\rho \dot{h} \Delta t$ , where  $\rho$  is the total density, and  $\dot{h} = dh/dt$  is the rate of growth of the thickness. Let the background species *j* have mass fraction  $X_j = \rho_j/\rho$  in the sample, and mass number  $A_j$ . Then the background atoms *j* have surface density  $N_j = X_j \rho \dot{h} \Delta t / A_j m_u$ , with  $m_u = 1/N_{\text{Avo}}$  the atomic mass unit. Thus

$$\frac{N_i^{\text{astro}}}{N_j^{\text{bg}}} = U_i f_i \frac{\Phi_i^{\text{interstellar}}}{4 X_j \rho \dot{h} / A_j m_u} e^{-t/\tau_i} \quad (15)$$

is the desired isotopic ratio.

We anchor our predictions to the reported detections of  $^{244}\text{Pu}$  discussed above. In this case we have

$$\frac{N_i^{\text{astro}}}{N_j^{\text{bg}}} = U_i \frac{f_i}{f_{\text{Pu}}} \left( \frac{N_i}{N_{244}} \right)_{\text{astro}} \frac{\Phi_{244, \text{astro}}^{\text{interstellar}}}{4 X_j \rho \dot{h} / A_j m_u} e^{-t/\tau_i}, \quad (16)$$

where we use the fact that the interstellar flux of a species is proportional to its (number) yield,  $\Phi_i^{\text{interstellar}} \propto \mathcal{N}_i$ . Using values typical for crusts, we have

$$\frac{N_i^{\text{astro}}}{N_j^{\text{bg}}} = 3 \times 10^{-13} U_i \frac{f_i}{f_{\text{Pu}}} \left( \frac{\mathcal{N}_i}{\mathcal{N}_{244}} \right)_{\text{astro}} e^{-t/\tau_i} \quad (17)$$

$$\times \left( \frac{\Phi_{244}^{\text{interstellar}}}{3000 \text{ cm}^{-2} \text{ Myr}^{-1}} \right) \left( \frac{1 \text{ ppm}}{X_j} \right) \left( \frac{A_j}{150} \right) \left( \frac{2 \text{ g/cm}^3}{\rho} \right) \left( \frac{3 \text{ mm/Myr}}{\dot{h}} \right). \quad (18)$$

Note that the signal is inversely proportional to both the growth rate and the background abundance in the sample:  $N_i^{\text{astro}}/N_j^{\text{bg}} \propto (X_j \dot{h})^{-1}$ . This favors samples with small growth rates and hence Fe-Mn crusts. It also favors elements that are rare in crusts (so long as the uptake is not too small).

**Table 8.** Predicted Interstellar Fluences for  $r$ -Process Radioisotopes based on  $^{244}\text{Pu}$

Isotope	$\mathcal{F}(3 \text{ Myr})$				$\mathcal{F}(10 \text{ Myr})$		$\mathcal{F}(20 \text{ Myr})$		$\mathcal{F}(50 \text{ Myr})$	
	SA	SB	KA	KB	KA	KB	KA	KB	KA	KB
$^{93}\text{Zr}$	1.6(4)	2.5(8)	1.4(4)	4.7(2)	7.1(3)	2.3(2)	2.2(2)	7.1(0)	1.8(-3)	5.8(-5)
$^{107}\text{Pd}$	1.6(5)	3.9(8)	2.3(4)	2.1(3)	1.1(5)	1.0(4)	8.5(4)	7.8(3)	1.1(4)	1.0(3)
$^{129}\text{I}$	9.6(5)	5.2(9)	2.7(5)	5.6(4)	2.1(6)	4.3(5)	2.9(6)	6.1(5)	2.5(6)	5.3(5)
$^{135}\text{Cs}$	1.6(4)	3.7(8)	1.0(3)	4.3(3)	2.6(2)	1.1(3)	3.3(0)	1.4(1)	1.8(-6)	8.2(-6)
$^{182}\text{Hf}$	9.2(3)	1.3(7)	2.1(3)	3.4(2)	1.3(4)	2.1(3)	1.3(4)	2.1(3)	4.1(3)	6.6(2)
$^{236}\text{U}$	5.4(3)	2.8(4)	6.0(3)	3.4(3)	5.3(4)	3.1(4)	9.1(4)	5.5(4)	1.5(5)	1.0(5)
$^{237}\text{Np}$	2.0(3)	4.7(3)	2.3(3)	1.6(3)	2.5(3)	1.7(3)	2.2(2)	1.5(2)	4.5(-2)	3.0(-2)
$^{247}\text{Cm}$	1.5(3)	1.4(3)	1.5(3)	1.4(3)	1.2(4)	1.1(4)	1.6(4)	1.5(4)	1.4(4)	1.3(4)

The interstellar fluences  $\mathcal{F}^{\text{interstellar}}$  are scaled from  $^{244}\text{Pu}$ , and are expressed units of [atoms  $\text{cm}^{-2}$ ], using the notation  $A(B) \equiv A \times 10^B$ . All results are for the present day, and include the effects of decay. the signal at 3 Mya assumes a flux duration of 1 Myr, and the others assume a constant flux after the event.

**Table 9.** Predictions for  $r$ -Process Radioisotopes in Fe-Mn Crusts based on  $^{244}\text{Pu}$  after 3 Myr

Isotope	Concentration [atoms/g]				Ratio $N_i^{\text{astro}}/N_j^{\text{bg}}$	Measurement Limit	Crust Elemental Abundance $X_j$	Predicted Signal Ratio			
	SA	SB	KA	KB				SA	SB	KA	KB
$^{93}\text{Zr}$	6.5(2)	1.0(7)	5.9(2)	1.9(1)	$^{93}\text{Zr}/^{92}\text{Zr}$	$6 \times 10^{-11}$	$6.5 \times 10^{-4}$	8.9(-16)	1.4(-11)	8.2(-16)	2.7(-17)
$^{107}\text{Pd}$	6.5(3)	1.6(7)	9.4(2)	8.6(1)	$^{107}\text{Pd}/^{106}\text{Pd}$	$10^{-8}$	$1.7 \times 10^{-9}$	2.5(-9)	6.1(-6)	3.6(-10)	3.3(-11)
$^{129}\text{I}$	4.0(4)	2.2(8)	1.1(4)	2.3(3)	$^{129}\text{I}/^{127}\text{I}$	$10^{-14}$	$5 \times 10^{-6}$	1.7(-11)	9.2(-8)	4.7(-12)	9.8(-13)
$^{135}\text{Cs}$	6.8(2)	1.5(7)	4.2(1)	1.8(2)	$^{135}\text{Cs}/^{133}\text{Cs}$	$9 \times 10^{-12}$	$1.5 \times 10^{-6}$	1.0(-13)	2.2(-9)	6.1(-15)	2.6(-14)
$^{182}\text{Hf}$	3.8(2)	5.5(5)	8.9(1)	1.4(1)	$^{182}\text{Hf}/^{180}\text{Hf}$	$10^{-11}$	$8 \times 10^{-6}$	4.5(-14)	6.4(-11)	1.0(-14)	1.7(-15)
$^{236}\text{U}$	2.2(2)	1.2(3)	2.5(2)	1.4(2)	$^{236}\text{U}/^{238}\text{U}$	$10^{-13}$	$10^{-5}$	8.9(-15)	4.7(-14)	1.0(-14)	5.7(-15)
$^{237}\text{Np}$	8.2(1)	2.0(2)	9.7(1)	6.6(1)	$^{237}\text{Np}/^{238}\text{U}$	$5 \times 10^{-11}$	$10^{-5}$	3.3(-15)	7.8(-15)	3.9(-15)	2.6(-15)
$^{247}\text{Cm}$	6.2(1)	5.6(1)	6.2(1)	5.7(1)	$^{247}\text{Cm}/^{238}\text{U}$	-	$10^{-5}$	2.5(-15)	2.3(-15)	2.5(-15)	2.3(-15)

The values are expressed as  $A(B) \equiv A \times 10^B$ . The crust abundances are taken from *Hein et al. (2000)*, and we assume  $\Phi^{\text{interstellar}}(^{244}\text{Pu}) = 3000 \text{ atoms cm}^{-2} \text{ Myr}^{-1}$  (*Waltner et al. 2015*). The uptake is assumed to be  $U = 0.10$  in all cases. The isotopic concentration  $n_i^{\text{astro}}/\rho$  is the number of atoms of isotope  $i$  per gram of crust. The crust elemental abundances  $X_j$  are mass fractions; for  $^{237}\text{Np}$  and  $^{247}\text{Cm}$ , the uranium abundance is given. The measurement limits are the AMS sensitivities for  $^{93}\text{Zr}$  (*Pavetich et al. 2019; Hain et al. 2018*),  $^{107}\text{Pd}$  (*Korschinek et al. 1994*),  $^{129}\text{I}$  (*Vockenhuber et al. 2015*),  $^{135}\text{Cs}$  (*Yin et al. 2015*) and  $^{182}\text{Hf}$  (*Vockenhuber et al. 2004*).

Tables 4-6 give the number ratios for various isotopes of interest  $(\mathcal{N}_i/\mathcal{N}_{244})_{\text{astro}} e^{-t/\tau_i}$ , where we incorporate the decay factors corresponding to different time scales of interest. For the lighter species with stable isotopes, the candidates of particular interest are those with large ratios to  $^{244}\text{Pu}$ .

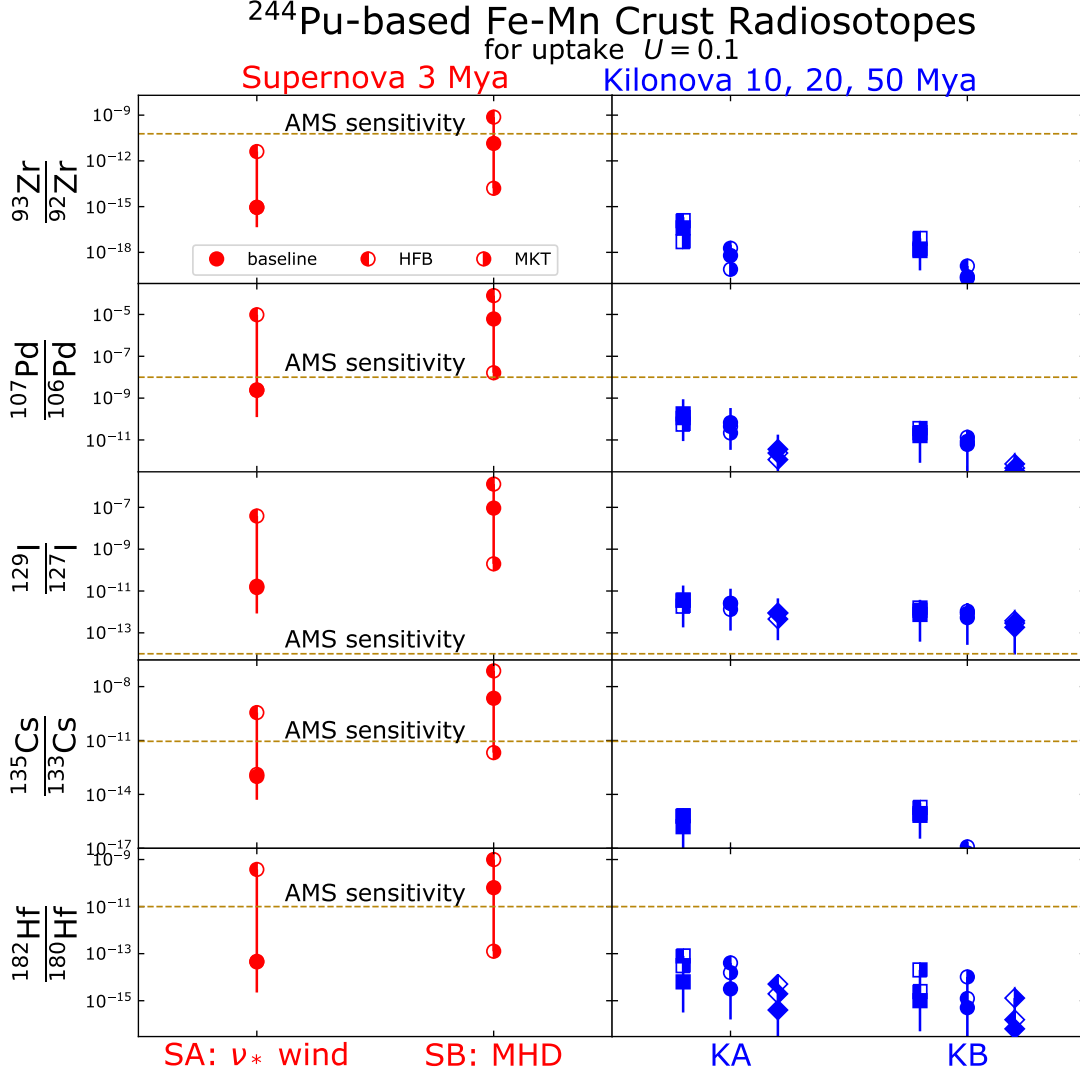


**Figure 13.** Radioisotope predictions normalized to the Wallner et al. (2015)  $^{244}\text{Pu}$  flux from Eq. (7). The predictions are normalized to 10% uptake, and assume dust efficiency equal to that of Pu; for other values multiply by  $U_i f_i / f_{\text{Pu}}$ . The uncertainties are only those due to the  $^{244}\text{Pu}$  flux, and the measurement limits are those in Table 9. The predictions are from (left panels) supernova  $r$ -process models after 3 Myr and (right panels) kilonova  $r$ -process models after 10, 20, 50 Myr. The results from our baseline calculations are shown as full symbols, and the half-filled symbols are results from HFB and MKT calculations.

Table 8 shows the time-integrated interstellar flux or *fluence*, as defined in eq. (4), for selected  $r$ -process radioisotopes in specific scenarios. The values are for the present day, and include the effects of decay. For the 3 Mya signal associated with a supernova, the duration is 1 Myr. For the kilonova signal at 10 Myr, the duration is assumed to be 10 Myr. The fluences are the most direct results from the astrophysical calculations, but to connect to geological and lunar measurements requires one specify abundances in particular samples.

Table 9 shows our predictions for selected radioisotope ratios following deposition in Fe-Mn crusts 3 Mya, normalized to 10% uptake and  $f_i / f_{\text{Pu}} = 1$ . These results also appear in Fig. 13, where we have used the  $^{244}\text{Pu}$  flux inferred from sediments 0.5 – 2.2 Myr old (Wallner et al. 2015) for normalization. In general we see that the supernova predictions are as large and sometimes much larger than those of kilonova models. This reflects the difficulty of making actinides in supernova models, which means that lower-mass species are more abundant relative to the  $^{244}\text{Pu}$  isotope that anchors our results. Variations between the kilonova model predictions are generally within a factor of 10. In contrast, the supernova predictions can span several orders of magnitude, with the SB model generally leading to larger low-mass

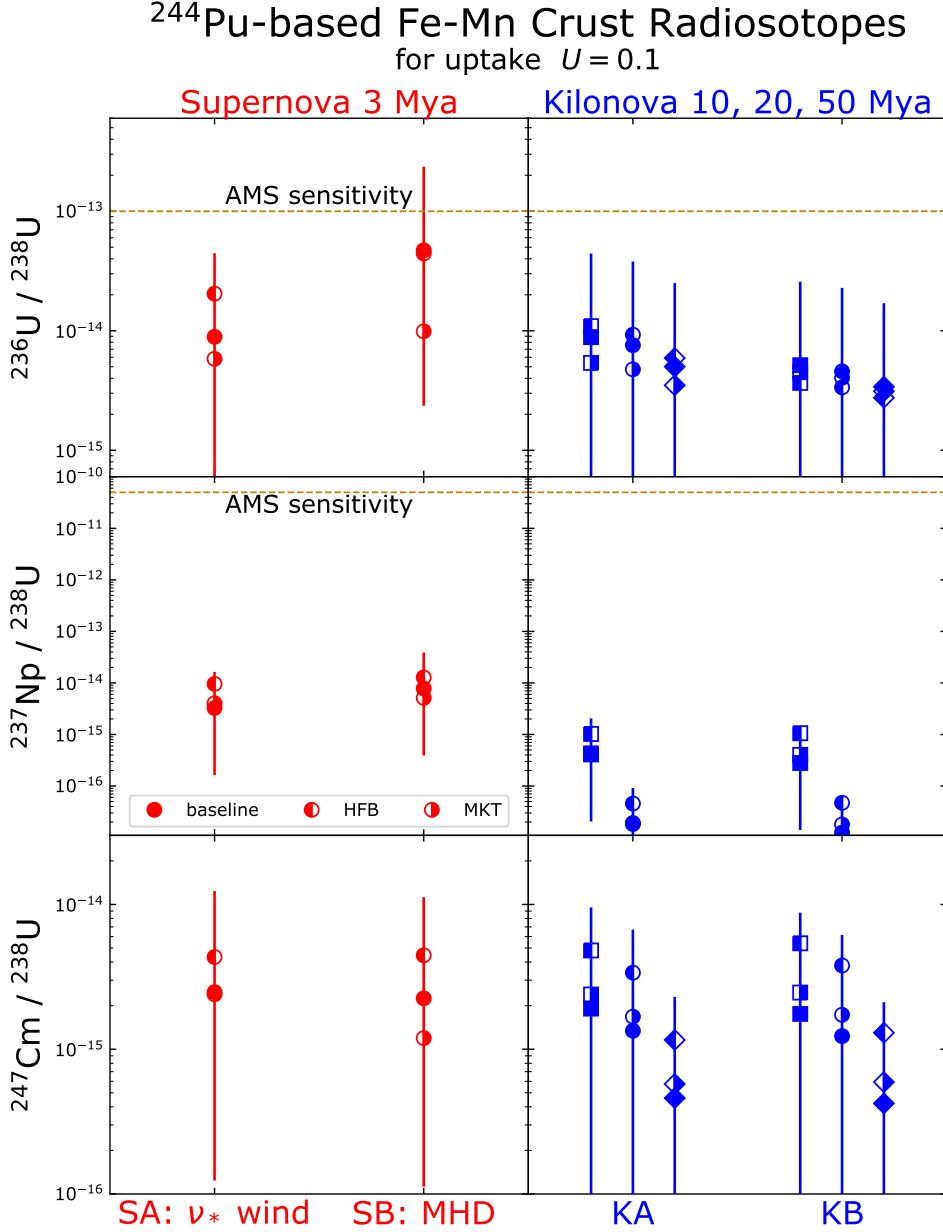


**Figure 14.** Predicted abundances of the actinides  $^{236}\text{U}$ ,  $^{237}\text{Np}$ , and  $^{247}\text{Cm}$  in Fe-Mn crusts, shown for the same SN and KN models as in Fig. 13. We use  $^{238}\text{U}$  as the reference standard for all three species. The results from our baseline calculations are shown as full symbols, and the half-filled symbols are results from HFB and MKT calculations.

abundances due to its particularly low  $^{244}\text{Pu}$  output. Also shown in Table 9 and Fig. 13 are the prospective AMS sensitivities for  $^{93}\text{Zr}$  (Pavetich et al. 2019; Hain et al. 2018),  $^{107}\text{Pd}$  (Korschinek et al. 1994),  $^{129}\text{I}$  (Vockenhuber et al. 2015),  $^{135}\text{Cs}$  (Yin et al. 2015) and  $^{182}\text{Hf}$  (Vockenhuber et al. 2004). We see that, whereas predictions for the  $^{93}\text{Zr}$  signal generally lie below the AMS sensitivity, those for  $^{107}\text{Pd}$ ,  $^{135}\text{Cs}$  and possibly  $^{182}\text{Hf}$  in model SB lie above the AMS sensitivity, the predictions for the  $^{129}\text{I}$  signal lie above the AMS sensitivity in both SN scenarios and possibly also in the KN scenarios.

Figure 14 shows Fe-Mn crust abundances for the actinides  $^{236}\text{U}$ ,  $^{237}\text{Np}$ , and  $^{247}\text{Cm}$ , for the same models as in Fig. 13. These are all elements with no stable isotopes, so we use  $^{238}\text{U}$  as a reference standard for the ratios presented;

we note that  $^{238}\text{U}$  is also the source of  $^{236}\text{U}$  background. We recall that natural uranium will far overwhelm any astrophysical contribution. For this reason, the  $^{236}\text{U}$  signal may be masked by other production mechanisms. For  $^{237}\text{Np}$ , suppression of the  $^{238}\text{U}$  signal may be necessary before a signal can be seen. We thus conclude that  $^{236}\text{U}$  and  $^{237}\text{Np}$  detections likely await improvements in measurement techniques. For  $^{247}\text{Cm}$ , uranium is not anticipated to be a limitation, but detection will require establishing a pure curium reference spike. We urge further study of the experimental possibilities for all of these species.

To summarize, we have found that the  $^{244}\text{Pu}$  evidence, if real, implies that the geological record should contain other *r*-process radioisotope signals. The abundances are in some cases within or close to the reach of existing AMS techniques, whereas improvements in the AMS sensitivity to key species is necessary in other cases. We now turn to considerations of sample collection for each of the radioisotopes of interest.

### 5.5. Terrestrial Searches

In order to detect and preserve these signals, we emphasize that samples must be collected from well-chosen sites and suitable media. The samples should have maintained a detectable abundance of the supernova debris from the initial deposit to the present. Moreover, it is of course also necessary that the samples be accessible for collection and delivery to the laboratory. We consider these issues for the Earth in this section, and for the Moon in the next Section.

Marine samples are the primary focus of interest as natural terrestrial archives, since continental material is subject to erosion, and radioisotope studies in ice cores do not extend so far into the past.<sup>10</sup> In general, deep-ocean deposits are essentially undisturbed, with very little bioturbation to blur the time structure, and are largely free of anthropogenic contamination from nuclear debris, as well as backgrounds from cosmic-ray spallation in the atmosphere. Debris at the sea floor accumulates in sediments that stretch back beyond the  $\sim 10$  Myr that have been studied so far, rendering them suitable for exploring possible astrophysical triggers of mass extinctions that occurred  $\gtrsim 10^8$  ya ago in addition to the well-attested  $^{60}\text{Fe}$  signal and evidence for  $^{53}\text{Mn}$  from  $\sim 3$  Mya and evidence for  $^{244}\text{Pu}$  deposition over the past 25 Myr. Ultimately, deep-ocean sediments may harden to make sedimentary rock in geological strata reaching back to much longer timescales. In this Section we highlight some of the key considerations from chemical oceanography that determine which astrophysical radioisotopes may have geologically favorable conditions for detection. We make heavy use in the following discussion of Broecker et al. (1982), Nozaki (2001), and the Geotraces database<sup>11</sup> and private communications with Craig Lundstrom and Tom Johnson (2021).

In considering the prospects for detecting marine deposits of radionuclides, one must consider the sedimentation rates of the radionuclides of interest, focusing on those with a short residence time and discarding those that remain dissolved in seawater. Table 9 lists the elements discussed earlier in this paper, together with their mean oceanic concentrations and characteristics of their distributions, which provide the basis for our discussion of the possibilities for detecting their radioisotopes in view of the SN and KN model calculations above.

- Among the *r*-process elements identified in the previous Section as being of interest, we note that zirconium sinks in the ocean, attaches to solid particles, and may be scavenged at the water/sediment interface, similarly to iron. The half-life of  $^{93}\text{Zr}$  ( $1.53 \times 10^6$  yr) is somewhat less than those of the isotopes  $^{60}\text{Fe}$  and  $^{53}\text{Mn}$  that have been reported in layers  $\sim 2.5 \times 10^6$  yr old. Figs. 8 and 9, and Table 4, indicate that its *r*-process production rate, which is quite model-dependent, may be orders of magnitude larger or rather smaller than that of  $^{60}\text{Fe}$ . However, Table 9 and Fig. 13 indicate that the  $^{93}\text{Zr}$  signal in 3 myr-old samples may lie below the estimated AMS sensitivity.

- Palladium has a distribution that increases with depth, but is not expected to bind to particles or be concentrated at the water/sediment interface. It has been detected in Fe-Mn crusts, but with low abundances (see Table 9) which is advantageous for our purposes. As a consequence, as seen in Table 9 and Fig. 13, some *r*-process models predict that the abundance of  $^{107}\text{Pd}$  may be within reach of the AMS technique if a suitable 3 myr-old sample can be found.

- Most iodine is in the form of the  $\text{IO}_3^-$  ion that is distributed conservatively, but a small fraction is in the form of the  $\text{I}^-$  ion that may be scavenged, preferentially in anoxic basins such as the Black Sea. Fitoussi & Raisbeck (2007) attempted to measure  $^{129}\text{I}$  in a relatively recent but pre-anthropogenic sediment, and found that care is needed to

<sup>10</sup> Though we recall that Antarctic ice dating back to 2.7 Mya has been recovered (Yan et al. 2019), potentially opening prospects for the future.

<sup>11</sup> <https://www.geotraces.org/>

**Table 10.** Estimated mean oceanic concentrations of selected elements, adapted from [Nozaki \(2001\)](#)

Element	Mean oceanic mass fraction ( $\times 10^{-12}$ )	Type of Distribution	Leaves Solution Rapidly
Mn	20	s	yes
Fe	30	s + n	yes
Zr	15	s + n	yes
Pd	0.06	n	yes
I ( $\text{IO}_3^-$ )	$5.8 \times 10^4$	c	no
I ( $\text{I}^-$ )	4.4	r + s	yes
Cs	310	c	no
Hf	0.07	s + n	yes
U	$3.2 \times 10^3$	c	no
Np	$\sim 10^{-5}$	c	no
Pu	-	r + s	yes
Cm	-	s?	?

Notes: In this Table *c* denotes a conservative element whose distribution follows salinity, *n* denotes a nutrient-like distribution that increases with depth, *s* denotes an element that attaches to particulate matter and may be scavenged at the water/sediment interface, and *r* denotes an element whose distribution is redox-controlled and may be formed in anoxic basins ([Nozaki 2001](#)).  $^{237}\text{Np}$  results are from [Lindahl et al. \(2005\)](#). We note also that there may be other geochemical and biological processes that affect the rates of uptake of different radionuclides in various materials. For example, magnetotactic bacteria secrete iron and therefore concentrate  $^{60}\text{Fe}$ , as discussed in [Ludwig et al. \(2016\)](#), and certain sorts of organic matter may absorb plutonium effectively ([J. Marshall, private communication, 2021](#)), specifically in anoxic environments. [Schneider & Livingston \(1984\)](#) measured anthropogenic  $^{242}\text{Cm}$  and  $^{244}\text{Cm}$  in Scottish coastal sediments, and summarized data indicating that  $^{244}\text{Cm}$  has also been detected in fish and seaweed but not in seawater; we also note that curium adheres very tightly to soil particles.

avoid anthropogenic contamination. [Ji et al. \(2015a\)](#) have presented the first AMS measurements of  $^{129}\text{I}$  in Fe-Mn crusts. These data already reveal the power of  $^{129}\text{I}$  to probe near-Earth explosions, particularly the possible kilonova enrichment of the Local Bubble, and the corresponding constraints are discussed in detail in the following Section 5.6.

- **Cesium** dissolves in water and has a conservative oceanic distribution, so  $^{135}\text{Cs}$  offers poor prospects for deep-ocean detection. Moreover, as seen in Table 9 and Fig. 13, most of the models studied indicate that the fraction of  $^{135}\text{Cs}$  may lie below the AMS sensitivity.

- **Hafnium** is an interesting target, particularly if production occurred more than 3 Mya, thanks to the  $^{182}\text{Hf}$  half-life of 8.9 Myr. Most of our *r*-process models produce less  $^{182}\text{Hf}$  than  $^{93}\text{Zr}$ , and the oceanic distribution of hafnium is similar to that of zirconium. In a sediment, [Vockenhuber et al. \(2004\)](#) have established the upper limit  $^{182}\text{Hf}/^{180}\text{Hf} < 10^{-6}$  using a 45g sample, and quote a total hafnium elemental abundance by dry weight of 8 ppm. Combining these numbers, we find an upper limit on the fraction by weight of  $^{182}\text{Hf}$  of  $8 \times 10^{-12}$ . [Martschini et al. \(2020\)](#) showed that these limits could in principle be improved dramatically using a laser technique to remove stable isobars. They find  $^{182}\text{Hf}/^{180}\text{Hf} = (3.4 \pm 2.1) \times 10^{-14}$ , on the basis of which they estimate a sensitivity of  $(^{182}\text{Hf}/^{180}\text{Hf})_{\min} \approx 6 \times 10^{-14}$ . This would correspond to a mass fraction of  $\sim 4 \times 10^{-18}$ , which could be achieved if the stable tungsten isobar  $^{182}\text{W}$  is absent or can be removed.

For comparison, [Wallner et al. \(2015\)](#) set an upper limit of  $< 6.7$   $^{244}\text{Pu}$  events in 1909g of deep-ocean crust. Since their efficiency for detecting  $^{244}\text{Pu}$  is  $1 \times 10^{-4}$ , this upper limit corresponding to a sensitivity to the fraction by weight of  $\sim 10^{-20}$  for  $^{244}\text{Pu}$ . (Their sensitivity in deep-ocean sediment is an order of magnitude worse.) In Table 4 we see ratios  $^{182}\text{Hf}/^{244}\text{Pu} < 8.7 \times 10^4$  (reached in model SB), suggesting that the sensitivity to models of the  $^{244}\text{Pu}$  search by [Wallner et al. \(2015\)](#) is better than that of the  $^{182}\text{Hf}$  search by [Vockenhuber et al. \(2004\)](#), though a more sensitive  $^{182}\text{Hf}$  search may have interesting prospects. [Vockenhuber et al. \(2004\)](#) use their data to quote an upper limit on the  $^{182}\text{Hf}$  flux into the sediment of  $2 \times 10^5/\text{cm}^2\text{y}$ , to be compared with the estimated ISM flux of  $0.05/\text{cm}^2\text{y}$ , assuming a global distribution of the in-falling ISM and that all of the material is deposited in the sediment. Thus there is considerable scope for a more sensitive measurement to observe a signal above the expected background. Table 9 and

**Table 11.** Ferromanganese Crusts with Measured  $^{129}\text{I}$  Profiles (Ji et al. 2015a,b)

Crust Name	Crust Location	Elemental Mass Fractions		$^{129}\text{I}/^{127}\text{I}$ Ratio/ $10^{-12}$	$^{129}\text{I}/\text{Fe}$
		X(Fe)	X(I)		
CDX80-1	(19°57.9' N, 172°55.1' E)	0.05 – 0.20	$(2.7 - 7.7) \times 10^{-5}$	$\leq 1.27$	$\leq 10^{-15}$
MDP5D44	(10°20.24' N, 167°26.5' W)	0.10 – 0.20	$(3.8 - 10.9) \times 10^{-5}$	$\leq 0.48$	$\leq 10^{-15}$

The ranges of the iron and iodine fractions in the crust samples CDX80-1 (MDP5D44) shown are for depths  $\in (0.5, 4)$  cm ( $\in (1.6.5)$  cm) and the iodine isotope ratios shown are for depths  $> 0.5$  cm ( $> 1$  cm).

Fig. 13 indicate that the fraction of  $^{182}\text{Hf}$  may be within the AMS sensitivity range in model SB.

- Uranium has a natural background of  $^{235}\text{U}$  and  $^{238}\text{U}$  that far overwhelms any astrophysical perturbations we might hope to detect. The shorter-lived  $^{236}\text{U}$  has no remaining proto-solar component, and so potentially could serve as an astrophysical signature. However, significant obstacles exist. In uranium ores, neutrons from fission can capture on  $^{235}\text{U}$  to create  $^{236}\text{U}$ . The resulting  $^{236}\text{U}/^{235}\text{U}$  ratio will be strongly sensitive to local conditions, making this background challenging to estimate. Anthropogenic  $^{236}\text{U}$  contamination is also a concern. Finally, uranium has a conservative oceanic distribution, so  $^{236}\text{U}$  is likely difficult to use in sediments and crusts would be preferred.

- Neptunium is poorly studied compared to other trans-uranic elements—indeed, it has been called the “neglected actinide” (Thompson 1982). Table 4 shows it is produced in abundances comparable to  $^{244}\text{Pu}$  and thus is of great interest to search for as a cross-check on  $^{244}\text{Pu}$  and potentially as a probe of the details of actinide synthesis. As for other trans-uranic elements, there are no stable isotopes, so elemental searches are viable. However, anthropogenic contamination is an issue. Lindahl et al. (2005) find that  $^{237}\text{Np}$  has a conservative oceanic distribution, and so does not readily precipitate. Thus, Fe-Mn crusts would seem to be a preferred terrestrial target. Future lunar measurements are also of interest; unfortunately, the initial report of  $^{237}\text{Np}$  evidence in *Apollo* return samples (Fields et al. 1972) was subsequently found to be compromised by airborne anthropogenic contamination (Fields et al. 1976).

- Like iodine, plutonium may be scavenged, and it is encouraging that  $^{244}\text{Pu}$  detection has been reported by multiple experiments, as seen in Table 7 and Fig. 7.<sup>12</sup> A confirmation of these putative signals is of the highest priority, and would impel further study. Measurements with higher sensitivity using deep-ocean deposits stretching back to ages comparable to the half-life of  $^{244}\text{Pu}$  ( $t_{1/2} = 81$  Myr) or further, would be very interesting, as would sufficient time resolution to distinguish a possible  $^{244}\text{Pu}$  pulse coincident with that observed for  $^{60}\text{Fe}$ , and/or any earlier similar pulses. We encourage searches in anoxic basins where the concentration of  $^{244}\text{Pu}$  may be higher.

- The model calculations in Table 4 indicate that a SN  $\sim 3$  Mya could deposit curium on Earth, with  $^{247}\text{Cm}$  at levels comparable to those for  $^{244}\text{Pu}$ , whereas most of the shorter-lived  $^{248}\text{Cm}$  would have decayed. This isotope thus makes an important target for geological and lunar searches.<sup>13</sup>

### 5.6. $^{129}\text{I}$ in Fe-Mn Crusts and Near-Earth Kilonovae: Present Constraints and Future Opportunities

The AMS measurements of  $^{129}\text{I}$  by Ji et al. (2015a) and Ji et al. (2015b) are from three ferromanganese crusts. For two of these, Ji et al. (2015a) tabulate  $^{129}\text{I}$  profiles to depths of 8 cm. Table 11 gives the locations and elemental compositions of these crusts, which are both in the mid-Pacific, at locations separated by about 2300 km. Natural production of  $^{129}\text{I}$  includes uranium fission products, as well as the daughters of spallation events between cosmic rays and atmospheric xenon. These give rise to a persistent flux of  $^{129}\text{I}$  into the crusts, which represents an irreducible background.

Ji et al. (2015a) and Ji et al. (2015b) find that the crusts show an  $^{129}\text{I}/^{127}\text{I}$  isotopic profile that drops with depth in a manner consistent with a background component undergoing radioactive decay, as seen in Fig. 15. Moreover, the most recent layer has an abundance consistent with the pre-bomb level found in sediments (Moran et al. 1998). Ji

<sup>12</sup> We note, however, that most of the shorter-lived isotope  $^{242}\text{Pu}$  would have decayed on the time-scales discussed here.

<sup>13</sup> Human Health Fact Sheet, <http://www.ead.anl.gov/pub/doc/curium.pdf>.

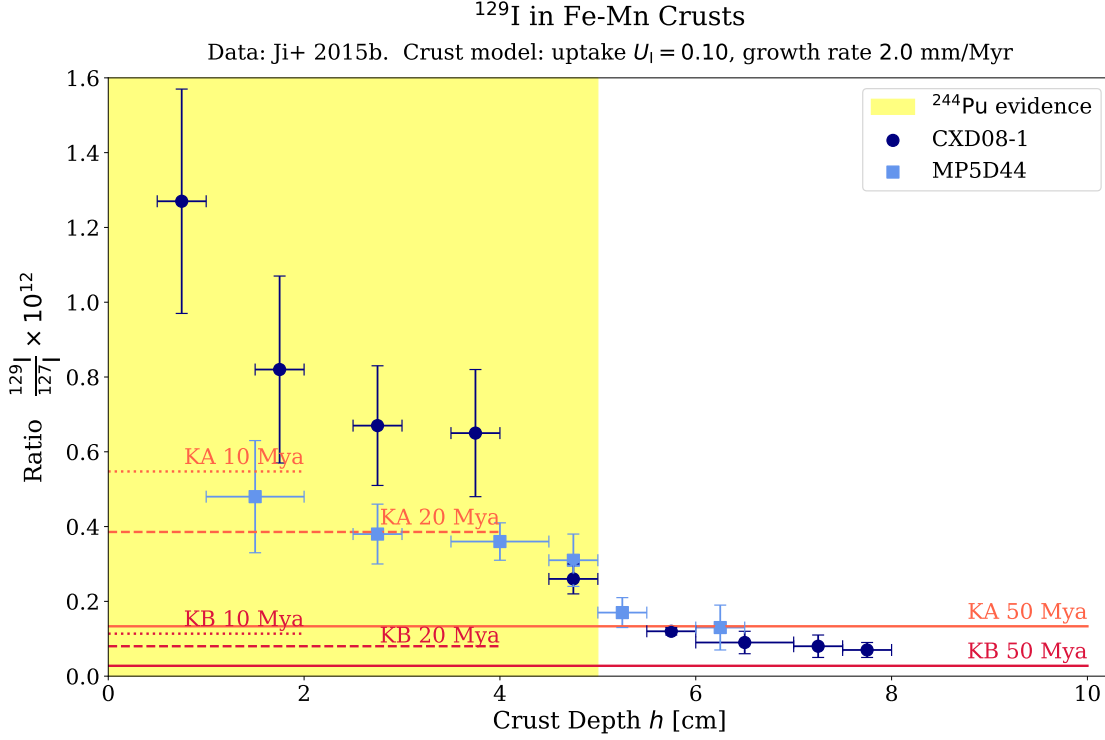


**Figure 15.** The evolution with depth of the  $^{129}\text{I}/^{127}\text{I}$  isotope ratio, based on the AMS data of Ji et al. (2015b). The horizontal lines represent the ratio  $^{129}\text{I}/^{127}\text{I}$  that would be generated within the KA and KB models occurring at the indicated times  $t_{\text{KN}}$  in the past; these represent a floor below which the natural  $^{129}\text{I}$  background cannot fall. KA curves for  $t_{\text{KN}} = (10, 20)$  Myr are offscale. These model lines assume a crust iodine uptake  $U_I = 0.1$  and a constant growth rate  $\dot{h}_0 = 2$  mm/Myr. Their heights scale as  $U_I \exp(-t_{\text{KN}}/\tau_{129})$ , and maximum depth scales as  $h_{\text{max}} = \dot{h}_0 t_{\text{KN}}$ . The yellow band shows the extent of  $^{244}\text{Pu}$  evidence using the assumed  $\dot{h}_0$ .

et al. (2015a) argue that this dropoff with depth suggests that the results are free of anthropogenic contamination. We note that the crust data show no strong evidence for a “floor” of  $^{129}\text{I}$  that persists as the background diminishes at increasing depth

The crusts in which Ji et al. (2015a) measured  $^{129}\text{I}$  lack independent measures of their growth rates, without which the depth profile cannot be transformed into a precise time history. Nonetheless we can use typical Fe-Mn growth rates to estimate the epochs probed: for a low growth rate  $\dot{h} = 1$  mm/Myr, the crusts span 5–80 Myr, while a high growth rate  $\dot{h} = 6$  mm/Myr would correspond to a range 1–13 Myr. It is therefore not clear that these data include the 2–3 Mya range of the  $^{60}\text{Fe}$  pulse, so that the supernova (one-step) scenario may not be probed directly by these data. However, as seen in Fig. 13 and Table 6, the SB model predicts  $^{129}\text{I}$  many orders of magnitude above the natural background, so that such a signal could be easily ruled out (or detected!) in a search within the  $^{60}\text{Fe}$  pulse in a crust.

On the other hand, it is clear that these data cover the timespan probed by the extended  $^{244}\text{Pu}$  flux, and thus probe the two-step scenario of kilonova enrichment of the proto-Local Bubble. We illustrate the power of  $^{129}\text{I}$  data in Fe-Mn crusts using the Ji et al. (2015a) data while emphasizing that, due to the lack of information on growth rate and uptake, our quantitative results are only crude estimates. Nevertheless, we hope that such order-of-magnitude estimates may stimulate further experimental work. In this spirit, we again assume a constant growth rate  $\dot{h}_0$ , so that a time  $t$  in the past corresponds to a depth  $h(t) = \dot{h}_0 t$ . If the kilonova event occurred at a time  $t_{\text{KN}}$  ago, the signal can extend to a maximum depth  $h_{\text{max}} = \dot{h}_0 t_{\text{KN}}$ .

All kilonova-produced radioisotopes will have decayed for the (unknown)  $t_{\text{KN}}$  duration since the explosion, regardless of the time history of their flux on Earth. Thus any kilonova-created flux will *not* show a radioactive decay pattern versus depth. This is in contrast to the natural  $^{129}\text{I}$  background, which is due to ongoing production and so should show the effects of decay versus depth. Just such a pattern is evident in Fig. 15; any kilonova-produced signal would

represent a “floor” underneath this natural background. Thus the deepest measurements have the most constraining power.

The kilonova signal in the crust is straightforward to calculate in the case where the growth rate and *r*-process flux are both constant. In this case the  $^{129}\text{I}$  profile versus depth  $h$  for kilonova model  $\alpha = (\text{KA}, \text{KB})$  has a step-like structure:

$$\frac{^{129}\text{I}}{^{127}\text{I}}(h)_\alpha = \begin{cases} (^{129}\text{I}/^{127}\text{I})_{\alpha,0} e^{-t_{\text{KN}}/\tau_{129}} & , \quad h \leq h_{\text{max}} = t_{\text{KN}}\dot{h}_0, \\ 0 & , \quad h > h_{\text{max}}, \end{cases} \quad (19)$$

where  $(^{129}\text{I}/^{127}\text{I})_{\alpha,0} = N_{129}^\alpha/N_{127}^{\text{bg}}$  from Eq. (17), which includes a factor  $f_{\text{I}}$  for dust formation and transport, and the uptake factor  $U_{\text{I}}$ . We see that the isotope ratio is constant with depth, and for increasing  $t_{\text{KN}}$  the level is progressively smaller but extends to greater depths.

In Fig. 15 we confront the data of Ji et al. (2015a,b) with some results from calculations based on the kilonova models KA and KB. For each of these, we show predictions for kilonova explosion time  $t_{\text{KN}} = (10, 20, 50)$  Myr, corresponding to a scenario in which an explosion at this time enriches and stirs the proto-Local Bubble, initiating a flux of *r*-process dust onto the Earth. The  $^{244}\text{Pu}$  data in Fig. 7 shows that this flux extended at least to the earliest measured bin 12 – 25 Mya, but neither excludes nor requires an earlier flux. Thus our constraints should apply only within this time window, though the explosion would have occurred earlier.

To predict the  $^{129}\text{I}/^{127}\text{I}$  ratio in the crust, we assume a constant growth rate  $\dot{h}_0 = 2$  mm/Myr and a value  $U_{\text{I}} = 0.1$  of the uptake factor for iodine.<sup>14</sup> With these  $(\dot{h}_0, U_{\text{I}})$  values, model KA would be excluded if the kilonova occurred  $\lesssim 50$  Mya, whereas model KB would be allowed for explosions  $\gtrsim 20$  Mya. There are clearly many uncertainties in this analysis: the line heights scale as  $(f_i/f_{\text{Pu}})U_{\text{I}} \exp(-t_{\text{KN}}/\tau_{129})$  and they reach to maximum depths that scale as  $h_{\text{max}} = \dot{h}_0 t_{\text{KN}}$ . Thus KA models can be accommodated with, for example, smaller uptake values.

The larger lesson is that it is of great interest to make additional  $^{129}\text{I}$  measurements in Fe-Mn crusts, which could offer an important new probe of possible sources of *r*-process isotopes. Also, it would be of considerable interest to search at even greater depths and thus earlier times than those shown in Fig. 19, to see if the  $^{129}\text{I}$  signal continues to drop as expected from a natural background, or whether a “floor” reveals itself and thus indicates a scenario with an early injection time and thus distant production epoch  $t_{\text{KN}}$ . It would be of particular interest to measure  $^{129}\text{I}$  in crusts with  $^{60}\text{Fe}$  data, searching both inside and beyond the  $^{60}\text{Fe}$  pulse; similarly, it would be useful to search for  $^{129}\text{I}$  in the same crusts that show  $^{244}\text{Pu}$  signals. Finally, we stress that independent measures of the growth rate, and of the iodine uptake, are as important as the additional  $^{129}\text{I}$  data themselves. The ability to limit astrophysical perturbations to  $^{129}\text{I}$  hinges upon the precision and reliability of the  $^{129}\text{I}$  profiles with time.

### 5.7. Lunar Searches

A great advantage of lunar material is that it avoids geological and oceanographic effects that transport, mix and dilute the signal. Moreover, the rate of uptake is likely to be high, so that all of the favoured *r*-process radioisotopes  $^{93}\text{Zr}$ ,  $^{107}\text{Pd}$ ,  $^{129}\text{I}$ ,  $^{135}\text{Cs}$ ,  $^{182}\text{Hf}$ ,  $^{236}\text{U}$ ,  $^{237}\text{Np}$ ,  $^{244}\text{Pu}$  and  $^{247}\text{Cm}$  are *a priori* interesting targets for searches in the lunar regolith. Fry et al. (2015) cautioned that some fast dust particles could lead to vaporization and escape of some of the ejecta mass. However, the lunar detections of  $^{60}\text{Fe}$  (Fimiani et al. 2016), with a fluence that is relatively high compared to terrestrial results, suggest that these effects are small. This could imply that much of the astrophysical dust slows to lower speeds by the time the particles arrive.

Thus the surface fluences of supernova species should be close to the interstellar fluences estimated in Table 8, modulo a geometric factor of the cosine of the vertical angle. However, to convert these values into predictions in, say, atoms per gram, requires one understands lunar surface processes over Myr timescales. Such a detailed analysis is beyond the scope of this work; we intend to visit this issue in a separate paper. Here we summarize some important considerations.

As impactors strike the lunar surface, the regolith gets continually reworked, a process known as gardening. Gardening mixes material more deeply over time, so that deeper material is less likely to have been disturbed recently, though it would have been disturbed in the more distant past. Shallow soil is continually turned over by the large flux of very small impactors. Costello et al. (2018) show that there has been significant reworking down to  $\sim 10$  cm over

<sup>14</sup> According to Ji et al. (2015b), iodine is enriched in crusts relative to seawater, though much less so than iron. This would allow a range that includes the value of  $U_{\text{I}}$  that we assume, but with considerable uncertainty. For comparison, in Fe-Mn crusts the estimates of the iron uptake in different crusts have varied from  $U_{\text{Fe}} = 0.6\%$  (Knie et al. 2004) to 7% and 17% (Wallner et al. 2016), while Wallner et al. (2015) estimate the  $^{244}\text{Pu}$  incorporation efficiency at  $U_{\text{Pu}} = 21 \pm 5\%$ .

the past 3 Myr, and significant reworking down to  $\sim 40$  cm over the past 400 Myr. Tables 5 and 6 suggest that  $^{129}\text{I}$ ,  $^{236}\text{U}$  and  $^{244}\text{Pu}$  may be the most interesting search targets at lower depths. However, the gardening process implies that lunar samples cannot be time-stamped accurately, and we recall that the *Apollo* lunar samples (Fimiani et al. 2016) have no timing information.

On the other hand, lunar samples may provide valuable information on the possible direction of any astrophysical source of live radioisotopes. If these arrive in dust grains that travel ballistically, their distributions could depend on the lunar latitude. The *Apollo* landing sites were all relatively close to the lunar equator. Therefore, in view also of their limited statistics, they provide limited information in this regard. However, the recent *Chang'e-5* sample return mission landed at a higher latitude,  $43.1^\circ$  N, the *Artemis* programme envisions landing at the lunar South Pole, and various commercial lunar sample return missions are also planned. More information on the latitude distribution may therefore be available in the coming years, and could discriminate between origins in the Scorpio-Centaurus and Tucana-Horologium associations.

We note, however, that there is an important source of radioisotope background on the Moon, namely cosmic-ray spallation on the lunar surface. This is an irreducible background, so the signal must be found above it. Spallation is less important for the heaviest isotopes, and is most effective when only one or a few nucleons are removed from a target nucleus. Thus a key issue is whether there are relatively abundant stable isotopes that have one or a few more nucleons than the radioisotope of interest. We note also that, although there is no anthropogenic background on the Moon, care must be taken after bringing samples to Earth, so as to avoid anthropogenic contamination, which was an issue for the evidence for  $^{236}\text{U}$  and  $^{237}\text{Np}$  on the Moon reported by Fields et al. (1972).

Cosmic-ray irradiation of the lunar regolith is also produces a substantial neutron flux at depth. Neutron exposure would lead to a  $^{236}\text{U}$  background that makes any extrasolar  $^{236}\text{U}$  difficult to find, but  $^{236}\text{U}$  searches could nonetheless be useful to establish which if either of these components is present. We note also that neutron captures on  $^{236}\text{U}$  will lead to  $^{237}\text{Np}$ , creating a background for that species.

## 6. DISCUSSION

We have entered an era of multi-messenger astrophysics, with the advent of gravitational wave, cosmic ray and neutrino measurements that complement the many decades of the electromagnetic spectrum that were already being explored. To these observations may be added those of live radioisotopes, which cast light on the history of the solar neighborhood and the potential impacts of nearby astrophysical events on the terrestrial environment and life. The first observations of deep-ocean deposits of live  $^{60}\text{Fe}$  have been confirmed by many other experiments, extending to measurements of  $^{60}\text{Fe}$  in samples of the lunar regolith, Antarctic ice and cosmic rays, and have been complemented by reports of live  $^{244}\text{Pu}$  and  $^{53}\text{Mn}$  in deep-ocean deposits. Among the obvious next issues to address are the nature(s) of the astrophysical event(s) that produced the  $^{60}\text{Fe}$  and other radioisotopes measured, and the possible impacts of past such events on the biosphere.

The reported detections of live  $^{244}\text{Pu}$  are particularly interesting from both of these perspectives. Whereas there is consensus that  $^{60}\text{Fe}$  is probably produced mainly by core-collapse supernovae, the origin(s) of  $^{244}\text{Pu}$  and other isotopes produced by the  $r$ -process are subject to more debate. Neutron-star mergers (kilonovae) are thought to be prolific  $r$ -process sites, an interpretation supported by the recent multi-messenger observations of the aftermath of the GW190521 event (Abbott et al. 2017a,b). However, kilonovae are also thought to be much rarer than core-collapse supernovae. Certain classes of supernovae may be  $r$ -process sites, in which case they might well be competitive locations for the  $r$ -process, and conversely some kilonovae may produce  $^{60}\text{Fe}$ , though they are unlikely to be its dominant source. There is an extensive literature on the likely production of lighter radioisotopes by supernovae and their possible observability on Earth: here we have extended those discussions to discuss the likely production of heavier radioisotopes via the  $r$ -process in both supernovae and kilonovae.

To this end, we have considered two representative models for the  $r$ -process in supernovae, using combinations of a modified neutrino-driven wind model and an MHD model adjusted to fit the data on abundances measured in the metal-poor star HD160617, and two representative kilonova models, with different combinations of dynamical ejecta and disk wind contributions, chosen to fit the data on HD160617 and an actinide-boost star J0954+5246. We have found that radioisotopes of interest with half-lives between 1 Myr and 500 Myr include  $^{93}\text{Zr}$ ,  $^{107}\text{Pd}$ ,  $^{129}\text{I}$ ,  $^{135}\text{Cs}$  and  $^{182}\text{Hf}$ . As seen in Fig. 13, at least some of these may be detectable using AMS techniques, and their presence or non-detection could constrain significantly models of  $r$ -process nucleosynthesis. The reported observations of  $^{244}\text{Pu}$  are nicely compatible with the explosion of a supernova within  $\mathcal{O}(100)$  Mpc of Earth, as postulated to explain the

observed  $^{60}\text{Fe}$  signal. However, if the  $^{244}\text{Pu}$  is due to direct deposition by a kilonova, it would have to have been much further away. As an alternative, we have proposed a two-step scenario, in which some of the  $^{244}\text{Pu}$  produced by a more distant kilonova was absorbed into the interstellar medium within the Local Bubble, before subsequently reaching Earth.

Observations of  $^{129}\text{I}$  may be able to constrain such a scenario. As seen in Fig. 15, the estimated abundance of  $^{129}\text{I}$  in one of the kilonova models may even exceed what has been observed in deep-ocean deposits (Ji et al. 2015a,b). As we have emphasized, additional measurements of  $^{129}\text{I}$  in ferromanganese crusts in conjunction with measurements of the crust growth rates, and of the iodine uptake would be of great interest, offering potentially new insights into possible sources of *r*-process isotopes.

Probes of possible live radioisotope deposits in the more distant past would also be interesting. Palaeontology is littered with mass extinctions of unknown provenance, and nearby astrophysical explosions within  $\sim 10$  pc could have been among the culprits. A case in point concerns the end of the Devonian epoch  $\sim 360$  Mya, around which time there were at least two mass extinctions, the Kellwasser and Hangenberg events. There is ample evidence of radiation UV-B damage to spores during the Hangenberg event (Marshall et al. 2020), which could have been due to destruction of the ozone layer during cosmic-ray bombardment following a supernova explosion  $\sim 20$  pc away (Fields et al. 2020). Detectable amounts of live radioisotopes with half-lives  $\mathcal{O}(100)$  Myr might have been deposited by such an event, with candidates including  $^{129}\text{I}$ ,  $^{232}\text{Th}$ ,  $^{235}\text{U}$ ,  $^{236}\text{U}$  and  $^{238}\text{U}$  as well as  $^{244}\text{Pu}$ . The relatively short half-life of  $^{129}\text{I}$  implies that most of any produced  $\sim 360$  Mya would have decayed by now, whereas the relatively long half-lives of  $^{232}\text{Th}$ ,  $^{235}\text{U}$  and  $^{238}\text{U}$  imply that these are likely to have important backgrounds from production before the formation of the solar system. However,  $^{244}\text{Pu}$  may offer interesting prospects for discovering a live radioisotope signature of the end-Devonian mass extinction(s); with sensitivity improvements  $^{236}\text{U}$  may provide a cross-check.

The searches for deep-ocean deposits of live radioisotopes are complicated by their diverse distributions in the ocean. Whereas some attach readily to particulate matter and may be scavenged at the water/sediment interface, others have depth distributions that follow salinity, and there are other possibilities as outlined in Table 9. Moreover, there may be biological effects that could either concentrate the live radioisotope of interest (e.g., magnetotactic bacteria) or disperse it (bioturbation). No such issues arise in the deposition of live isotopes in the lunar regolith, where  $^{60}\text{Fe}$  has been measured in *Apollo* samples. It is therefore encouraging that the *Chang'e-5* mission has recently returned to Earth a new sample of lunar material, and that the future *Artemis* and other lunar missions have similar objectives. We advocate efforts to replicate the *Apollo* results of  $^{60}\text{Fe}$  and urge searches for the other radioisotopes discussed in this paper. The lunar regolith is subject to gardening by impactors striking the lunar surface, leading to reworking down to  $\sim 10$  cm over the past 3 My and down to  $\sim 40$  cm over the past 400 Myr. Longer-lived species such as  $^{129}\text{I}$ ,  $^{182}\text{Hf}$ ,  $^{244}\text{Pu}$ , and  $^{247}\text{Cm}$  may be the most interesting targets at lower depths. Moreover, if lunar radioisotopes arrive in dust grains that travel ballistically, their latitude distribution may help indicate the possible direction of the event that originated them. As we have discussed, the *Apollo* samples were gathered relatively close to the lunar equator, whereas *Chang'e-5* landed in the northern hemisphere and *Artemis* is planned to land near the South Pole. Measurements in their samples may therefore provide some indication of the possible latitude of their astrophysical sources, perhaps providing some discrimination between the Scorpio-Centaurus and Tucana-Horologium associations, which have been touted as possible hosts of the explosion that emitted a pulse of  $^{60}\text{Fe} \sim 3$  Mya. This would herald the dawn of radioisotope astronomy.

It is worth noting that our studies of live radioisotopes ejected from recent nearby explosions are closely linked with the long-studied question of now-extinct radioisotopes injected into the proto-solar nebula. As described in the excellent reviews by Meyer & Clayton (2000); Adams (2010); Lugaro et al. (2018), meteorites show evidence that more than a dozen of what we have called “medium-lived” radioisotopes (“short-lived” in the cosmochemistry literature) were present in the nascent solar system. This includes some *r*-process species (Meyer 1993; Côté et al. 2021). Our calculations can provide a new evaluation of pre-decay abundances for the early Solar System.

Finally, it is well to recall that the putative deep-ocean  $^{244}\text{Pu}$  detections are tentative, always at most one atom per bin. It remains possible that future work might show that these can be explained without recourse to extraterrestrial sources. Two possibilities are a systematic error common to the four experiments to date, or anthropogenic contamination. In such an eventuality, our analysis should be reframed but not obviated. (1) If there were no  $^{244}\text{Pu}$  during the  $^{60}\text{Fe}$  pulse, there would be strong limits on supernova production of *r*-process actinides. While feeble production is not unexpected, such a result would represent a direct measurement for a specific supernova, the first of its kind beyond meteoritic studies of the proto-solar nebula. (2) If there were no  $^{244}\text{Pu}$  outside the  $^{60}\text{Fe}$  pulse, there would be

no need to invoke a recent kilonova event to produce and inject  $r$ -process species. In principle, the *lack* of evidence for such events would constrain their frequency, but the uncertainties are large and so the limits would likely be weak.

Even in the absence of the potential  $^{244}\text{Pu}$  detections, it would still be of great interest to pursue geological and lunar searches for  $r$ -process radioisotopes within the last 10 Myr. The  $^{60}\text{Fe}$  pulse confirms a SN 3 Mya, and there are some indications of another event at  $\sim 7$  Mya; these present a unique opportunity to probe supernova nucleosynthesis in the laboratory. Neutrino-driven winds should operate at some level in supernovae, possibly only producing species out to the second peak. Thus a search for  $^{129}\text{I}$  in particular, but also  $^{93}\text{Zr}$ ,  $^{107}\text{Pd}$ , and  $^{135}\text{Cs}$ , could offer new insight into the physics of neutrino-driven winds. In this way, a detection of or even strong limits to  $^{129}\text{I}$  and these other species can give unique information about the physics of the poorly-understood region just above the proto-neutron star.

## 7. CONCLUSIONS AND FUTURE DIRECTIONS

We summarize our conclusions as follows.

- We have compiled a comprehensive list of possible signatures of near-Earth explosions in the form of “medium-lived” radioisotopes, summarizing their possible astrophysical origins and geological prospects, and assessing their detectability via AMS. Thereafter we have focused on  $r$ -process species.
- We have presented new calculations of  $r$ -process radioisotope yields and uncertainties for both supernova and kilonova scenarios. We have constrained these models to reproduce solar and actinide-boosted halo star abundance patterns.
- We find that, for both SNe and KNe,  $^{129}\text{I}$  is the most abundant product, with  $r$ -process mass fractions that are comparable in the different models we address here. Production of  $^{107}\text{Pd}$  is similarly robust, but there are progressively larger variations in the yields of  $^{93}\text{Zr}$ ,  $^{135}\text{Cs}$ , and  $^{182}\text{Hf}$ . The rates of actinide production show the largest variations between the models, but their production ratios are relatively stable. Since there are indications of live  $^{244}\text{Pu}$  in the deep ocean, we use these observations to anchor predictions for other actinide radioisotopes.
- For supernovae, we have studied  $r$ -process radioisotope production in both a modified neutrino-driven wind scenario and a magnetohydrodynamic model. These supernova scenarios struggle to make actinides at all unless neutrino processes are able to create low  $Y_e$  conditions. Thus the SN models, and particularly the unmodified MHD SN model, give high ratios of the lighter  $r$ -process radioisotopes relative to  $^{244}\text{Pu}$ .
- Kilonovae resulting from neutron star mergers show robust  $r$ -process actinide synthesis, and therefore have lower ratios of the lighter  $r$ -process radioisotopes relative to  $^{244}\text{Pu}$ .
- Turning to geological data, we reviewed data on deep-ocean  $^{244}\text{Pu}$  in Fe-Mn crusts and sediments, combining searches by four groups. The published indications are tentative but intriguing: the published evidence for  $^{244}\text{Pu}$  deposits spans an extended time period from 1 to 25 Mya. The largest fluxes overlap the time of supernova  $^{60}\text{Fe}$  deposition, but the sustained flux over a much longer interval (if real) points towards a separate mechanism for  $r$ -process deposition on Earth.
- We have studied the delivery to Earth by a nearby SN 3 Mya of  $^{244}\text{Pu}$  and other  $r$ -process radioisotopes along with  $^{60}\text{Fe}$ . In this “one-step” model, the inferred  $^{244}\text{Pu}$  yields can be accommodated in both the neutrino-driven wind and MHD models. By contrast, such a “one-step” direct deposition of KN products is strongly inconsistent with both  $^{60}\text{Fe}$  and  $^{244}\text{Pu}$  data.
- We therefore constructed a “two-step” model for  $r$ -process delivery to Earth in which a KN explosion  $\sim 10$  to  $\sim 50$  Mya enriched the molecular cloud that gave rise to the Local Bubble. Dust grains seeded thereby with  $r$ -process radioisotopes would have bombarded the Earth thereafter. This model can account for the observed  $^{244}\text{Pu}$  with plausible KN distances and rates.
- We have presented predictions for AMS searches for  $r$ -process radioisotopes in deep-ocean Fe-Mn crusts, in both the one-step SN and two-step KN scenarios. With current AMS sensitivities,  $^{129}\text{I}$  is the most promising. Proposed AMS advances could make  $^{182}\text{Hf}$  another very interesting target. Additional AMS improvements would

be needed to detect  $^{93}\text{Zr}$ ,  $^{107}\text{Pd}$ , and  $^{135}\text{Cs}$ . Whilst alternative production mechanisms may elevate the  $^{236}\text{U}$  background, measurements of  $^{236}\text{U}$ ,  $^{237}\text{Np}$ , and  $^{247}\text{Cm}$  may serve as important complementary measurements to the  $^{244}\text{Pu}$  data.

- We have also reviewed the Moon’s fossil record of radioisotopes, where the systematics are very different from, and complementary to, geological searches. We recall that  $^{60}\text{Fe}$  has already been discovered in the *Apollo* samples of the lunar regolith, and have discussed opportunities for the new generation of lunar sample return missions to yield evidence for *r*-process radioisotopes.
- We note that, even in the absence of the potential  $^{244}\text{Pu}$  detection, the geological and lunar searches for  $^{129}\text{I}$  in particular, but also  $^{93}\text{Zr}$ ,  $^{107}\text{Pd}$ , and  $^{135}\text{Cs}$ , would still be interesting to explore the nature of the *r*-process sites.

Our work and its larger context suggest many directions for future work, which we summarize here.

- We urge geological searches for *r*-process radioisotopes in deep-ocean Fe-Mn crusts, most pressingly  $^{129}\text{I}$ . There is also a clear need for more sensitive searches in deep-ocean sediments for other live radioisotopes, coincident with the  $^{60}\text{Fe}$  pulse and the putative  $^{244}\text{Pu}$  signals in sediments.
- We urge searches for *r*-process isotopes in the regolith samples brought to Earth recently by the *Chang’e-5* lunar mission and upcoming missions including *Artemis*.
- We urge efforts to improve the AMS sensitivities for *r*-process radioisotopes, especially for  $^{93}\text{Zr}$ ,  $^{107}\text{Pd}$ , and  $^{244}\text{Pu}$ .
- We look forward to new data on unstable, neutron-rich nuclides whose properties set the abundance ratios described here, from experiments at current and upcoming radioactive beam facilities such as CARIBU (Savard et al. 2008) and the  $N = 126$  factory (Savard et al. 2020) at ATLAS, RIBF at RIKEN (Motobayashi & Sakurai 2012), ISAC/ARIEL at TRIUMF (Dilling et al. 2014; Willing et al. 2014), FAIR at GSI (Kester et al. 2016), and FRIB (Gade & Sherrill 2016; Horowitz et al. 2019).<sup>15</sup>
- Explosion models remain essential, and we urge that radioisotope yields be reported for calculations within models of both SNe and KNe and in studies of their *r*-process output.
- We urge continued work on models of supernova dust formation, propagation, and injection into the heliosphere.
- Astrophysical models of the Local Bubble are critical, and it would be of particular interest to study the effects of injection of debris from a nearby KN.
- To establish the broader context of the Local Bubble and recent radioisotope production, we urge continued studies of chemical evolution models for the larger solar neighborhood. Of particular importance is the distribution of radioisotopes including *r*-process species, as well as their variation.

The discovery of  $^{60}\text{Fe}$  in deep-ocean deposits heralded a new era of laboratory astrophysics using relic live radioisotopes to explore events in the solar neighborhood, using them to understand quantitatively their contributions to nucleosynthesis. Previous studies have focused on nearby supernovae and their roles in forming the Local Bubble. The hints of discovery of  $^{244}\text{Pu}$  carry these studies to a new level, including the possibility of gathering experimental information about sites of the *r*-process, extending the catalogue of events of interest to include kilonovae, possibly within a larger range surrounding the Local Bubble. This development also extends and expands the investigation of the potential repercussions on Earth of astrophysical events, including possible impacts on the biosphere. The longer half-life of  $^{244}\text{Pu}$  (81 Myr) compared to  $^{60}\text{Fe}$  (2.5 Myr) offers the possibility of studying the implications of such events in the more distant past, and exploring directly possible links to mass terrestrial extinctions, opening a new frontier in astrobiology.

<sup>15</sup> See also <https://groups.nsl.msu.edu/frib/rates/fribrates.html>.

## ACKNOWLEDGMENTS

We are particularly thankful to Brian Fry for many discussions on all aspects of this paper. We are also grateful for illuminating discussions on geological issues with Tom Johnson and Craig Lundstrom, on AMS with Philippe Collon, and on star formation with Tony Wong and Leslie Looney. The work of X.W. was supported by U.S. National Science Foundation under grant number PHY-1630782 for the Focused Research Hub in Theoretical Physics: Network for Neutrinos, Nuclear Astrophysics, and Symmetries (N3AS). The work of R.S. was supported by N3AS as well as the U.S. Department of Energy under Nuclear Theory Contract No. DE-FG02-95-ER40934. The work of J.E. was supported partly by the United Kingdom STFC Grant ST/T000759/1 and partly by the Estonian Research Council via a Mobilias Plus grant. The work of A.M.C. was supported by the U.S. Nuclear Regulatory Committee Award 31310019M0037 and the National Science Foundation under grant number PHY-1713857. The work of J.A.M. was supported by the Future Investigators in NASA Earth and Space Science and Technology (FINESST) program under grant number NNN19ZDA001N-FINESST.

*Software:*

Matplotlib (Hunter 2007, <http://dx.doi.org/10.1109/MCSE.2007.55>),  
 Numpy (Oliphant 2006; van der Walt et al. 2011, <https://doi.org/10.1109/MCSE.2011.37>),  
 Portable Routines for Integrated nucleoSynthesis Modeling (PRISM) (Mumpower et al. 2018; Sprouse et al. 2020).

## REFERENCES

- Abbott, B. P., et al. 2017a, *Astrophys. J. Lett.*, 848, L12, doi: [10.3847/2041-8213/aa91c9](https://doi.org/10.3847/2041-8213/aa91c9)
- . 2017b, *Astrophys. J. Lett.*, 848, L13, doi: [10.3847/2041-8213/aa920c](https://doi.org/10.3847/2041-8213/aa920c)
- Abbott, B. P., Abbott, R., Abbott, T. D., et al. 2017, *ApJL*, 848, L12, doi: [10.3847/2041-8213/aa91c9](https://doi.org/10.3847/2041-8213/aa91c9)
- Abbott et al., B. P. 2017, *PhRvL*, 119, 161101, doi: [10.1103/PhysRevLett.119.161101](https://doi.org/10.1103/PhysRevLett.119.161101)
- Adams, F. C. 2010, *ARA&A*, 48, 47, doi: [10.1146/annurev-astro-081309-130830](https://doi.org/10.1146/annurev-astro-081309-130830)
- Adams, S. M., Kochanek, C. S., Beacom, J. F., Vagins, M. R., & Stanek, K. Z. 2013, *ApJ*, 778, 164, doi: [10.1088/0004-637X/778/2/164](https://doi.org/10.1088/0004-637X/778/2/164)
- Aguilar, M., Cavasonza, L. A., Allen, M. S., et al. 2021, *Phys. Rev. Lett.*, 126, 041104, doi: [10.1103/PhysRevLett.126.041104](https://doi.org/10.1103/PhysRevLett.126.041104)
- Andreoni, I., Kool, E. C., Sagués Carracedo, A., et al. 2020, *ApJ*, 904, 155, doi: [10.3847/1538-4357/abbf4c](https://doi.org/10.3847/1538-4357/abbf4c)
- Andreoni, I., Coughlin, M. W., Kool, E. C., et al. 2021, *Fast-transient Searches in Real Time with ZTFReST: Identification of Three Optically-discovered Gamma-ray Burst Afterglows and New Constraints on the Kilonova Rate.* <https://arxiv.org/abs/2104.06352>
- Arcones, A., & Janka, H. T. 2011, *A&A*, 526, A160, doi: [10.1051/0004-6361/201015530](https://doi.org/10.1051/0004-6361/201015530)
- Arcones, A., Janka, H. T., & Scheck, L. 2007, *A&A*, 467, 1227, doi: [10.1051/0004-6361:20066983](https://doi.org/10.1051/0004-6361:20066983)
- Arcones, A., & Thielemann, F. K. 2013, *Journal of Physics G Nuclear Physics*, 40, 013201, doi: [10.1088/0954-3899/40/1/013201](https://doi.org/10.1088/0954-3899/40/1/013201)
- Argast, D., Samland, M., Thielemann, F. K., & Qian, Y. Z. 2004, *A&A*, 416, 997, doi: [10.1051/0004-6361:20034265](https://doi.org/10.1051/0004-6361:20034265)
- Arnould, M., Goriely, S., & Takahashi, K. 2007, *PhR*, 450, 97, doi: [10.1016/j.physrep.2007.06.002](https://doi.org/10.1016/j.physrep.2007.06.002)
- Athanassiadou, T., & Fields, B. D. 2011, *NewA*, 16, 229, doi: [10.1016/j.newast.2010.09.007](https://doi.org/10.1016/j.newast.2010.09.007)
- Audi, G., Kondev, F. G., Wang, M., Huang, W., & Naimi, S. 2017, *Chinese Physics C*, 41, 030001, doi: [10.1088/1674-1137/41/3/030001](https://doi.org/10.1088/1674-1137/41/3/030001)
- Balantekin, A. B., & Yüksel, H. 2005, *New Journal of Physics*, 7, 51, doi: [10.1088/1367-2630/7/1/051](https://doi.org/10.1088/1367-2630/7/1/051)
- Barnes, J., Zhu, Y. L., Lund, K. A., et al. 2020, *arXiv e-prints*, arXiv:2010.11182. <https://arxiv.org/abs/2010.11182>
- Bauswein, A., Goriely, S., & Janka, H. T. 2013, *ApJ*, 773, 78, doi: [10.1088/0004-637X/773/1/78](https://doi.org/10.1088/0004-637X/773/1/78)
- Beniamini, P., & Hotokezaka, K. 2020, *MNRAS*, 496, 1891, doi: [10.1093/mnras/staa1690](https://doi.org/10.1093/mnras/staa1690)
- Binns, W., et al. 2016, *Science*, 352, 677, doi: [10.1126/science.aad6004](https://doi.org/10.1126/science.aad6004)
- Blake, J. B., & Schramm, D. N. 1973, *Nature Physical Science*, 243, 138, doi: [10.1038/physci243138a0](https://doi.org/10.1038/physci243138a0)
- Bliss, J., Witt, M., Arcones, A., Montes, F., & Pereira, J. 2018, *ApJ*, 855, 135, doi: [10.3847/1538-4357/aaadbe](https://doi.org/10.3847/1538-4357/aaadbe)
- Boschini, M. J., Della Torre, S., Gervasi, M., et al. 2021, *arXiv e-prints*, arXiv:2101.12735. <https://arxiv.org/abs/2101.12735>
- Bovard, L., Martin, D., Guercilena, F., et al. 2017, *PhRvD*, 96, 124005, doi: [10.1103/PhysRevD.96.124005](https://doi.org/10.1103/PhysRevD.96.124005)

- Broecker, W. S., Peng, T.-H., et al. 1982, Tracers in the Sea (Lamont-Doherty Geological Observatory, Columbia University Palisades, New York)
- Burbidge, E. M., Burbidge, G. R., Fowler, W. A., & Hoyle, F. 1957, *Reviews of Modern Physics*, 29, 547, doi: [10.1103/RevModPhys.29.547](https://doi.org/10.1103/RevModPhys.29.547)
- Caballero, O. L., McLaughlin, G. C., & Surman, R. 2012, *ApJ*, 745, 170, doi: [10.1088/0004-637X/745/2/170](https://doi.org/10.1088/0004-637X/745/2/170)
- Chen, W.-X., & Beloborodov, A. M. 2007, *ApJ*, 657, 383, doi: [10.1086/508923](https://doi.org/10.1086/508923)
- Choplin, A., Tominaga, N., & Meyer, B. S. 2020, *A&A*, 639, A126, doi: [10.1051/0004-6361/202037966](https://doi.org/10.1051/0004-6361/202037966)
- Christl, M., Dai, X., Lachner, J., Kramer-Tremblay, S., & Synal, H.-A. 2014, *Nuclear Instruments and Methods in Physics Research B*, 331, 225, doi: [10.1016/j.nimb.2013.11.045](https://doi.org/10.1016/j.nimb.2013.11.045)
- Chruslinska, M., Belczynski, K., Klencki, J., & Benacquista, M. 2018, *MNRAS*, 474, 2937, doi: [10.1093/mnras/stx2923](https://doi.org/10.1093/mnras/stx2923)
- Costello, E. S., Ghent, R. R., & Lucey, P. G. 2018, *Icarus*, 314, 327, doi: [10.1016/j.icarus.2018.05.023](https://doi.org/10.1016/j.icarus.2018.05.023)
- Côté, B., Fryer, C. L., Belczynski, K., et al. 2018, *ApJ*, 855, 99, doi: [10.3847/1538-4357/aaad67](https://doi.org/10.3847/1538-4357/aaad67)
- Côté, B., Eichler, M., Arcones, A., et al. 2019, *ApJ*, 875, 106, doi: [10.3847/1538-4357/ab10db](https://doi.org/10.3847/1538-4357/ab10db)
- Côté, B., Eichler, M., Yagüe López, A., et al. 2021, *Science*, 371, 945, doi: [10.1126/science.aba1111](https://doi.org/10.1126/science.aba1111)
- Cowan, J. J., Sneden, C., Lawler, J. E., et al. 2021, *Reviews of Modern Physics*, 93, 015002, doi: [10.1103/RevModPhys.93.015002](https://doi.org/10.1103/RevModPhys.93.015002)
- Cowan, J. J., Thielemann, F.-K., & Truran, J. W. 1991, *Physics Reports*, 208, 267, doi: [https://doi.org/10.1016/0370-1573\(91\)90070-3](https://doi.org/10.1016/0370-1573(91)90070-3)
- Cowperthwaite et al., P. S. 2017, *ApJL*, 848, L17. <http://stacks.iop.org/2041-8205/848/i=2/a=L17>
- Davila, N., Bojazi, M. J., & Meyer, B. S. 2019, in *American Institute of Physics Conference Series*, Vol. 2076, *Exotic Nuclei and Nuclear/particle AstroPhysics (VII)*. *Physics with Small Accelerators*, 030005, doi: [10.1063/1.5091631](https://doi.org/10.1063/1.5091631)
- Della Valle, M., Guetta, D., Cappellaro, E., et al. 2018, *MNRAS*, 481, 4355, doi: [10.1093/mnras/sty2541](https://doi.org/10.1093/mnras/sty2541)
- Dessart, L., Ott, C. D., Burrows, A., Rosswog, S., & Livne, E. 2009, *ApJ*, 690, 1681, doi: [10.1088/0004-637X/690/2/1681](https://doi.org/10.1088/0004-637X/690/2/1681)
- Dilling, J., Krücken, R., & Ball, G. 2014, *Hyperfine Interactions*, 225, 1, doi: [10.1007/s10751-013-0877-7](https://doi.org/10.1007/s10751-013-0877-7)
- Dillmann, I. 2008, *AIP Conf. Proc.*, 1016, 143, doi: [10.1063/1.2943564](https://doi.org/10.1063/1.2943564)
- Duan, H., Friedland, A., McLaughlin, G. C., & Surman, R. 2011, *Journal of Physics G Nuclear Physics*, 38, 035201, doi: [10.1088/0954-3899/38/3/035201](https://doi.org/10.1088/0954-3899/38/3/035201)
- Eichler, M., Arcones, A., Kelic, A., et al. 2015, *ApJ*, 808, 30, doi: [10.1088/0004-637X/808/1/30](https://doi.org/10.1088/0004-637X/808/1/30)
- Ellis, J., Fields, B. D., & Schramm, D. N. 1996, *ApJ*, 470, 1227, doi: [10.1086/177945](https://doi.org/10.1086/177945)
- Ellis, J., & Schramm, D. N. 1995, *Proceedings of the National Academy of Sciences*, 92, 235, doi: [10.1073/pnas.92.1.235](https://doi.org/10.1073/pnas.92.1.235)
- Endrizzi, A., Ciolfi, R., Giacomazzo, B., Kastaun, W., & Kawamura, T. 2016, *Classical and Quantum Gravity*, 33, 164001, doi: [10.1088/0264-9381/33/16/164001](https://doi.org/10.1088/0264-9381/33/16/164001)
- Fernández, R., Kasen, D., Metzger, B. D., & Quataert, E. 2015, *MNRAS*, 446, 750, doi: [10.1093/mnras/stu2112](https://doi.org/10.1093/mnras/stu2112)
- Fields, B. D., & Ellis, J. 1999, *NewA*, 4, 419, doi: [10.1016/S1384-1076\(99\)00034-2](https://doi.org/10.1016/S1384-1076(99)00034-2)
- Fields, B. D., Hochmuth, K. A., & Ellis, J. 2005, *ApJ*, 621, 902, doi: [10.1086/427797](https://doi.org/10.1086/427797)
- Fields, B. D., Melott, A. L., Ellis, J., et al. 2020, *Proceedings of the National Academy of Science*, 117, 21008, doi: [10.1073/pnas.2013774117](https://doi.org/10.1073/pnas.2013774117)
- Fields, P. R., Diamond, H., Metta, D. N., & Rokop, D. J. 1976, in *Lunar and Planetary Science Conference*, Vol. 7, *Lunar and Planetary Science Conference*, 251
- Fields, P. R., Diamond, H., Metta, D. N., Rokop, D. J., & Stevens, C. M. 1972, *Lunar and Planetary Science Conference Proceedings*, 3, 1637
- Fifield, L., Clacher, A., Morris, K., et al. 1997, *Nuclear Instruments and Methods in Physics Research Section B: Beam Interactions with Materials and Atoms*, 123, 400, doi: [https://doi.org/10.1016/S0168-583X\(96\)00428-4](https://doi.org/10.1016/S0168-583X(96)00428-4)
- Fimiani, L., et al. 2016, *Phys. Rev. Lett.*, 116, 151104
- Fischer, T., Whitehouse, S. C., Mezzacappa, A., Thielemann, F. K., & Liebendörfer, M. 2010, *A&A*, 517, A80, doi: [10.1051/0004-6361/200913106](https://doi.org/10.1051/0004-6361/200913106)
- Fischer, T., Wu, M.-R., Wehmeyer, B., et al. 2020, *ApJ*, 894, 9, doi: [10.3847/1538-4357/ab86b0](https://doi.org/10.3847/1538-4357/ab86b0)
- Fitoussi, C., & Raisbeck, G. M. 2007, *Nuclear Instruments and Methods in Physics Research B*, 259, 351, doi: [10.1016/j.nimb.2007.01.179](https://doi.org/10.1016/j.nimb.2007.01.179)
- Fitoussi, C., et al. 2008, *Phys. Rev. Lett.*, 101, 121101, doi: [10.1103/PhysRevLett.101.121101](https://doi.org/10.1103/PhysRevLett.101.121101)
- Foucart, F., O'Connor, E., Roberts, L., et al. 2015, *Phys. Rev. D*, 91, 124021, doi: [10.1103/PhysRevD.91.124021](https://doi.org/10.1103/PhysRevD.91.124021)
- Fröhlich, C., Martínez-Pinedo, G., Liebendörfer, M., et al. 2006, *PhRvL*, 96, 142502, doi: [10.1103/PhysRevLett.96.142502](https://doi.org/10.1103/PhysRevLett.96.142502)
- Fry, B. J., Fields, B. D., & Ellis, J. R. 2015, *ApJ*, 800, 71, doi: [10.1088/0004-637X/800/1/71](https://doi.org/10.1088/0004-637X/800/1/71)
- . 2016, *ApJ*, 827, 48, doi: [10.3847/0004-637X/827/1/48](https://doi.org/10.3847/0004-637X/827/1/48)
- Fujimoto, S.-i., & Nagakura, H. 2021, *MNRAS*, 502, 2319, doi: [10.1093/mnras/stab171](https://doi.org/10.1093/mnras/stab171)

- Fujimoto, S.-i., Nishimura, N., & Hashimoto, M.-a. 2008, *ApJ*, 680, 1350, doi: [10.1086/529416](https://doi.org/10.1086/529416)
- Gade, A., & Sherrill, B. M. 2016, *Phys. Scripta*, 91, 053003, doi: [10.1088/0031-8949/91/5/053003](https://doi.org/10.1088/0031-8949/91/5/053003)
- Gall, C., Hjorth, J., Rosswog, S., Tanvir, N. R., & Levan, A. J. 2017, *ApJL*, 849, L19, doi: [10.3847/2041-8213/aa93f9](https://doi.org/10.3847/2041-8213/aa93f9)
- Girardi, L., Groenewegen, M. A. T., Hatziminaoglou, E., & da Costa, L. 2005, *A&A*, 436, 895, doi: [10.1051/0004-6361:20042352](https://doi.org/10.1051/0004-6361:20042352)
- Giuliani, S. A., Martinez-Pinedo, G., Wu, M.-R., & Robledo, L. M. 2020, *PhRvC*, 102, 045804, doi: [10.1103/PhysRevC.102.045804](https://doi.org/10.1103/PhysRevC.102.045804)
- Gomez, H. L., Clark, C. J. R., Nozawa, T., et al. 2012, *MNRAS*, 420, 3557, doi: [10.1111/j.1365-2966.2011.20272.x](https://doi.org/10.1111/j.1365-2966.2011.20272.x)
- Goriely, S., Chamel, N., & Pearson, J. M. 2009, *PhRvL*, 102, 152503, doi: [10.1103/PhysRevLett.102.152503](https://doi.org/10.1103/PhysRevLett.102.152503)
- Goriely, S., & Janka, H. T. 2016, *MNRAS*, 459, 4174, doi: [10.1093/mnras/stw946](https://doi.org/10.1093/mnras/stw946)
- Gosse, J. C., & Phillips, F. M. 2001, *Quaternary Science Reviews*, 20, 1475, doi: [10.1016/S0277-3791\(00\)00171-2](https://doi.org/10.1016/S0277-3791(00)00171-2)
- Guozhu, H., Ming, H., Zuying, Z., et al. 2013, *Nuclear Instruments and Methods in Physics Research B*, 294, 132, doi: [10.1016/j.nimb.2012.05.016](https://doi.org/10.1016/j.nimb.2012.05.016)
- Hain, K., Deneva, B., Faestermann, T., et al. 2018, *Nuclear Instruments and Methods in Physics Research B*, 423, 42, doi: [10.1016/j.nimb.2018.02.034](https://doi.org/10.1016/j.nimb.2018.02.034)
- Hartmann, D. H., Kretschmer, K., & Diehl, R. 2002, in *Nuclear Astrophysics*, ed. W. Hillebrandt & E. Müller, 154–163. <https://arxiv.org/abs/astro-ph/0205110>
- Hartmann, L., Ballesteros-Paredes, J., & Bergin, E. A. 2001, *ApJ*, 562, 852, doi: [10.1086/323863](https://doi.org/10.1086/323863)
- Haxton, W., & Johnson, C. W. 1988, *Nature*, 333, 325
- Hayakawa, T., Ko, H., Cheoun, M.-K., et al. 2018, *PhRvL*, 121, 102701, doi: [10.1103/PhysRevLett.121.102701](https://doi.org/10.1103/PhysRevLett.121.102701)
- Hein, J. R., Koschinsky, A., Bau, M., et al. 2000, *Handbook of marine mineral deposits*, 18, 239
- Hoffman, D. C., Lawrence, F. O., Mewherter, J. L., & Rourke, F. M. 1971, *Nature*, 152, 132
- Hoffman, R. D., Woosley, S. E., & Qian, Y. Z. 1997, *ApJ*, 482, 951, doi: [10.1086/304181](https://doi.org/10.1086/304181)
- Holmbeck, E. M., Beers, T. C., Roederer, I. U., et al. 2018, *ApJL*, 859, L24, doi: [10.3847/2041-8213/aac722](https://doi.org/10.3847/2041-8213/aac722)
- Horowitz, C. J., Arcones, A., Côté, B., et al. 2019, *Journal of Physics G Nuclear Physics*, 46, 083001, doi: [10.1088/1361-6471/ab0849](https://doi.org/10.1088/1361-6471/ab0849)
- Hotokezaka, K., Kiuchi, K., Kyutoku, K., et al. 2013, *Phys. Rev. D*, 87, 024001, doi: [10.1103/PhysRevD.87.024001](https://doi.org/10.1103/PhysRevD.87.024001)
- Howard, W. M. 1993, *Meteoritics*, 28, 365
- Hüdepohl, L., Müller, B., Janka, H. T., Marek, A., & Raffelt, G. G. 2010, *PhRvL*, 104, 251101, doi: [10.1103/PhysRevLett.104.251101](https://doi.org/10.1103/PhysRevLett.104.251101)
- Hunter, J. D. 2007, *Computing in Science and Engineering*, 9, 90, doi: [10.1109/MCSE.2007.55](https://doi.org/10.1109/MCSE.2007.55)
- Ji, L., Liu, G., Chen, Z., et al. 2015a, *Acta Oceanologica Sinica*, 34, 31
- Ji, L., Liu, G., Huang, Y., Xing, N., & Chen, Z. 2015b, *Acta Oceanologica Sinica*, 34, 13
- Jin, Z.-P., Li, X., Wang, H., et al. 2018, *ApJ*, 857, 128, doi: [10.3847/1538-4357/aab76d](https://doi.org/10.3847/1538-4357/aab76d)
- Johns, L., Nagakura, H., Fuller, G. M., & Burrows, A. 2020, *PhRvD*, 102, 103017, doi: [10.1103/PhysRevD.102.103017](https://doi.org/10.1103/PhysRevD.102.103017)
- Just, O., Bauswein, A., Ardevol Pulpillo, R., Goriely, S., & Janka, H. T. 2015, *MNRAS*, 448, 541, doi: [10.1093/mnras/stv009](https://doi.org/10.1093/mnras/stv009)
- Just, O., Bauswein, A., Pulpillo, R. A., Goriely, S., & Janka, H.-T. 2015, *Monthly Notices of the Royal Astronomical Society*, 448, 541, doi: [10.1093/mnras/stv009](https://doi.org/10.1093/mnras/stv009)
- Kachelrieß, M., Neronov, A., & Semikoz, D. V. 2018, *Phys. Rev. D*, 97, 063011, doi: [10.1103/PhysRevD.97.063011](https://doi.org/10.1103/PhysRevD.97.063011)
- Kajino, T., Aoki, W., Balantekin, A., et al. 2019, *Progress in Particle and Nuclear Physics*, 107, 109, doi: <https://doi.org/10.1016/j.pnpnp.2019.02.008>
- Kasen, D., Metzger, B., Barnes, J., Quataert, E., & Ramirez-Ruiz, E. 2017, *Nature*, 551, 80, doi: [10.1038/nature24453](https://doi.org/10.1038/nature24453)
- Kester, O., Spiller, P., & Stoecker, H. 2016, *FAIR project at GSI*, ed. S. Myers & O. Bruning, 611–622, doi: [10.1142/9789814436403\\_0032](https://doi.org/10.1142/9789814436403_0032)
- Knie, K., Korschinek, G., Faestermann, T., et al. 1999, *Phys. Rev. Lett.*, 83, 18, doi: [10.1103/PhysRevLett.83.18](https://doi.org/10.1103/PhysRevLett.83.18)
- Knie, K., et al. 2004, *Phys. Rev. Lett.*, 93, 171103
- Kobayashi, C., Karakas, A. I., & Lugaro, M. 2020, *ApJ*, 900, 179, doi: [10.3847/1538-4357/abae65](https://doi.org/10.3847/1538-4357/abae65)
- Kodama, T., & Takahashi, K. 1975, *Nuclear Physics A*, 239, 489, doi: [https://doi.org/10.1016/0375-9474\(75\)90381-4](https://doi.org/10.1016/0375-9474(75)90381-4)
- Koll, D., Korschinek, G., Faestermann, T., et al. 2019, *Phys. Rev. Lett.*, 123, 072701, doi: [10.1103/PhysRevLett.123.072701](https://doi.org/10.1103/PhysRevLett.123.072701)
- Kondev, F. G., Wang, M., Huang, W. J., Naimi, S., & Audi, G. 2021, *Chinese Physics C*, 45, 030001, doi: [10.1088/1674-1137/abddae](https://doi.org/10.1088/1674-1137/abddae)
- Korobkin, O., Hungerford, A. M., Fryer, C. L., et al. 2020, *ApJ*, 889, 168, doi: [10.3847/1538-4357/ab64d8](https://doi.org/10.3847/1538-4357/ab64d8)
- Korschinek, G., Faestermann, T., Kastel, S., et al. 1994, *Nuclear Instruments and Methods in Physics Research B*, 92, 146, doi: [10.1016/0168-583X\(94\)95995-1](https://doi.org/10.1016/0168-583X(94)95995-1)

- Korschinek, G., Faestermann, T., Poutivtsev, M., et al. 2020, *Phys. Rev. Lett.*, 125, 031101, doi: [10.1103/PhysRevLett.125.031101](https://doi.org/10.1103/PhysRevLett.125.031101)
- Kutschera, W. 2013, *International Journal of Mass Spectrometry*, 349-350, 203, doi: [10.1016/j.ijms.2013.05.023](https://doi.org/10.1016/j.ijms.2013.05.023)
- Kyutoku, K., Kiuchi, K., Sekiguchi, Y., Shibata, M., & Taniguchi, K. 2018, *Phys. Rev. D*, 97, 023009, doi: [10.1103/PhysRevD.97.023009](https://doi.org/10.1103/PhysRevD.97.023009)
- Lachner, J., Dillmann, I., Faestermann, T., et al. 2012, *PhRvC*, 85, 015801, doi: [10.1103/PhysRevC.85.015801](https://doi.org/10.1103/PhysRevC.85.015801)
- Lazauskas, R., Lunardini, C., & Volpe, C. 2009, *JCAP*, 04, 029, doi: [10.1088/1475-7516/2009/04/029](https://doi.org/10.1088/1475-7516/2009/04/029)
- Lehner, L., Liebling, S. L., Palenzuela, C., et al. 2016, *Classical and Quantum Gravity*, 33, 184002, doi: [10.1088/0264-9381/33/18/184002](https://doi.org/10.1088/0264-9381/33/18/184002)
- Lien, A., & Fields, B. D. 2009, *JCAP*, 2009, 047, doi: [10.1088/1475-7516/2009/01/047](https://doi.org/10.1088/1475-7516/2009/01/047)
- Lindahl, P., Roos, P., Holm, E., & Dahlgaard, H. 2005, *Journal of Environmental Radioactivity*, 82, 285, doi: <https://doi.org/10.1016/j.jenvrad.2005.01.011>
- Looney, L. W., Tobin, J. J., & Fields, B. D. 2006, *ApJ*, 652, 1755, doi: [10.1086/508407](https://doi.org/10.1086/508407)
- López-Lora, M., & Chamizo, E. 2019, *Nuclear Instruments and Methods in Physics Research B*, 455, 39, doi: [10.1016/j.nimb.2019.06.018](https://doi.org/10.1016/j.nimb.2019.06.018)
- Ludwig, P., Bishop, S., Egli, R., et al. 2016, *Proceedings of the National Academy of Sciences*, 113, 9232, doi: [10.1073/pnas.1601040113](https://doi.org/10.1073/pnas.1601040113)
- Lugaro, M., Ott, U., & Kereszturi, Á. 2018, *Progress in Particle and Nuclear Physics*, 102, 1, doi: [10.1016/j.pnpnp.2018.05.002](https://doi.org/10.1016/j.pnpnp.2018.05.002)
- Malkus, A., McLaughlin, G. C., & Surman, R. 2016, *Phys. Rev. D*, 93, 045021, doi: [10.1103/PhysRevD.93.045021](https://doi.org/10.1103/PhysRevD.93.045021)
- Marketin, T., Huther, L., & Martinez-Pinedo, G. 2016, *Phys. Rev. C*, 93, 025805, doi: [10.1103/PhysRevC.93.025805](https://doi.org/10.1103/PhysRevC.93.025805)
- Marshall, J. E., Lakin, J., Troth, I., & Wallace-Johnson, S. M. 2020, *Science Advances*, 6, eaba0768
- Martin, D., Perego, A., Arcones, A., et al. 2015, *ApJ*, 813, 2, doi: [10.1088/0004-637X/813/1/2](https://doi.org/10.1088/0004-637X/813/1/2)
- Martschini, M., Lachner, J., Merchel, S., et al. 2020, in *European Physical Journal Web of Conferences*, Vol. 232, European Physical Journal Web of Conferences, 02003, doi: [10.1051/epjconf/202023202003](https://doi.org/10.1051/epjconf/202023202003)
- McGary, V. T., & Johnson, C. W. 2007, *Astropart. Phys.*, 27, 233, doi: [10.1016/j.astropartphys.2006.10.002](https://doi.org/10.1016/j.astropartphys.2006.10.002)
- Melott, A. L., Marinho, F., & Paulucci, L. 2019, *Astrobiology*, 19, 825, doi: [10.1089/ast.2018.1902](https://doi.org/10.1089/ast.2018.1902)
- Melott, A. L., Lieberman, B. S., Laird, C. M., et al. 2004, *International Journal of Astrobiology*, 3, 55, doi: [10.1017/S1473550404001910](https://doi.org/10.1017/S1473550404001910)
- Meyer, B. S. 1993, *Meteoritics*, 28, 399
- Meyer, B. S., & Clayton, D. D. 2000, *SSRv*, 92, 133, doi: [10.1023/A:1005282825778](https://doi.org/10.1023/A:1005282825778)
- Miller, J. M., Sprouse, T. M., Fryer, C. L., et al. 2020, *ApJ*, 902, 66, doi: [10.3847/1538-4357/abb4e3](https://doi.org/10.3847/1538-4357/abb4e3)
- Moran, J. E., Fehn, U., & Teng, R. T. 1998, *Chemical Geology*, 152, 193
- Mösta, P., Roberts, L. F., Halevi, G., et al. 2018a, *ApJ*, 864, 171, doi: [10.3847/1538-4357/aad6ec](https://doi.org/10.3847/1538-4357/aad6ec)
- . 2018b, *ApJ*, 864, 171, doi: [10.3847/1538-4357/aad6ec](https://doi.org/10.3847/1538-4357/aad6ec)
- Motobayashi, T., & Sakurai, H. 2012, *Progress of Theoretical and Experimental Physics*, 2012, 03C001, doi: [10.1093/ptep/pts059](https://doi.org/10.1093/ptep/pts059)
- Mumpower, M. R., Kawano, T., Sprouse, T. M., et al. 2018, *ApJ*, 869, 14, doi: [10.3847/1538-4357/aaeaca](https://doi.org/10.3847/1538-4357/aaeaca)
- Murphey, C., Hogan, J. W., Fields, B. D., & Narayan, G. 2020, *arXiv e-prints*, arXiv:2012.06552, <https://arxiv.org/abs/2012.06552>
- Murray, N. 2011, *ApJ*, 729, 133, doi: [10.1088/0004-637X/729/2/133](https://doi.org/10.1088/0004-637X/729/2/133)
- Nishimura, N., Rauscher, T., Hirschi, R., et al. 2018, *Mon. Not. Roy. Astron. Soc.*, 474, 3133, doi: [10.1093/mnras/stx3033](https://doi.org/10.1093/mnras/stx3033)
- Nozaki, Y. 2001, *Encyclopedia of Ocean Sciences* (eds. JH Steel et al.). Vol. 2, Academic Press
- Nozawa, T., Maeda, K., Kozasa, T., et al. 2011, *ApJ*, 736, 45, doi: [10.1088/0004-637X/736/1/45](https://doi.org/10.1088/0004-637X/736/1/45)
- Oliphant, T. 2006, *NumPy: A guide to NumPy, USA*: Trelgol Publishing. <http://www.numpy.org/>
- Ouellette, N., Desch, S. J., Bizzarro, M., et al. 2009, *GeoCoA*, 73, 4946, doi: [10.1016/j.gca.2008.10.044](https://doi.org/10.1016/j.gca.2008.10.044)
- Paul, M., Valenta, A., Ahmad, I., et al. 2001, *ApJL*, 558, L133, doi: [10.1086/323617](https://doi.org/10.1086/323617)
- Pavetich, S., Carey, A., Fifield, L. K., et al. 2019, *Nuclear Instruments and Methods in Physics Research B*, 438, 77, doi: [10.1016/j.nimb.2018.07.019](https://doi.org/10.1016/j.nimb.2018.07.019)
- Perego, A., Rosswog, S., Cabezón, R. M., et al. 2014, *MNRAS*, 443, 3134, doi: [10.1093/mnras/stu1352](https://doi.org/10.1093/mnras/stu1352)
- Pruet, J., Woosley, S. E., & Hoffman, R. D. 2003, *ApJ*, 586, 1254, doi: [10.1086/367957](https://doi.org/10.1086/367957)
- Radice, D., Perego, A., Hotokezaka, K., et al. 2018, *ApJL*, 869, L35, doi: [10.3847/2041-8213/aaf053](https://doi.org/10.3847/2041-8213/aaf053)
- Raisbeck, G., Tran, T., Lunney, D., et al. 2007, *Nuclear Instruments and Methods in Physics Research B*, 259, 673, doi: [10.1016/j.nimb.2007.01.205](https://doi.org/10.1016/j.nimb.2007.01.205)

- Reichert, M., Obergaulinger, M., Eichler, M., Aloy, M. Á., & Arcones, A. 2021, *MNRAS*, 501, 5733, doi: [10.1093/mnras/stab029](https://doi.org/10.1093/mnras/stab029)
- Roederer, I. U., & Lawler, J. E. 2012, *ApJ*, 750, 76, doi: [10.1088/0004-637X/750/1/76](https://doi.org/10.1088/0004-637X/750/1/76)
- Röllin, S., Sahli, H., Holzer, R., Astner, M., & Burger, M. 2009, *Applied Radiation and Isotopes*, 67, 821, doi: <https://doi.org/10.1016/j.apradiso.2009.01.041>
- Rosswog, S., Feindt, U., Korobkin, O., et al. 2017, *Classical and Quantum Gravity*, 34, 104001, doi: [10.1088/1361-6382/aa68a9](https://doi.org/10.1088/1361-6382/aa68a9)
- Rosswog, S., Piran, T., & Nakar, E. 2013, *Monthly Notices of the Royal Astronomical Society*, 430, 2585, doi: [10.1093/mnras/sts708](https://doi.org/10.1093/mnras/sts708)
- Ruderman, M. A. 1974, *Science*, 184, 1079, doi: [10.1126/science.184.4141.1079](https://doi.org/10.1126/science.184.4141.1079)
- Savard, G., Brodeur, M., Clark, J. A., Knaack, R. A., & Valverde, A. A. 2020, *Nuclear Instruments and Methods in Physics Research B*, 463, 258, doi: [10.1016/j.nimb.2019.05.024](https://doi.org/10.1016/j.nimb.2019.05.024)
- Savard, G., Baker, S., Davids, C., et al. 2008, *Nuclear Instruments and Methods in Physics Research B*, 266, 4086, doi: [10.1016/j.nimb.2008.05.091](https://doi.org/10.1016/j.nimb.2008.05.091)
- Scalo, J., & Wheeler, J. C. 2002, *ApJ*, 566, 723, doi: [10.1086/338329](https://doi.org/10.1086/338329)
- Schneider, D., & Livingston, H. 1984, *Nuclear Instruments and Methods in Physics Research*, 223, 510, doi: [https://doi.org/10.1016/0167-5087\(84\)90700-2](https://doi.org/10.1016/0167-5087(84)90700-2)
- Seeger, P. A., & Schramm, D. N. 1970, *ApJL*, 160, L157, doi: [10.1086/180550](https://doi.org/10.1086/180550)
- Sekiguchi, Y., Kiuchi, K., Kyutoku, K., Shibata, M., & Taniguchi, K. 2016, *Phys. Rev. D*, 93, 124046, doi: [10.1103/PhysRevD.93.124046](https://doi.org/10.1103/PhysRevD.93.124046)
- Shetye, S., et al. 2020, *Astronomy & Astrophysics*, 635, L6, doi: [doi.org/10.1051/0004-6361/202037481](https://doi.org/10.1051/0004-6361/202037481)
- Siegel, D. M., Barnes, J., & Metzger, B. D. 2019, *Nature*, 569, 241, doi: [10.1038/s41586-019-1136-0](https://doi.org/10.1038/s41586-019-1136-0)
- Siegel, D. M., Barnes, J., & Metzger, B. D. 2019, *Nature*, 569, 241, doi: [10.1038/s41586-019-1136-0](https://doi.org/10.1038/s41586-019-1136-0)
- Siegel, D. M., & Metzger, B. D. 2018, *ApJ*, 858, 52, doi: [10.3847/1538-4357/aabaec](https://doi.org/10.3847/1538-4357/aabaec)
- Sprouse, T. M., Mumpower, M. R., & Surman, R. 2020, arXiv e-prints, arXiv:2008.06075. <https://arxiv.org/abs/2008.06075>
- Steier, P., Hrnccek, E., Priller, A., et al. 2013, *Nuclear Instruments and Methods in Physics Research Section B: Beam Interactions with Materials and Atoms*, 294, 160, doi: <https://doi.org/10.1016/j.nimb.2012.06.017>
- Surman, R., McLaughlin, G. C., & Hix, W. R. 2006, *ApJ*, 643, 1057, doi: [10.1086/501116](https://doi.org/10.1086/501116)
- Surman, R., McLaughlin, G. C., Ruffert, M., Janka, H.-T., & Hix, W. R. 2008, *The Astrophysical Journal*, 679, L117, doi: [10.1086/589507](https://doi.org/10.1086/589507)
- Takami, H., Nozawa, T., & Ioka, K. 2014, *ApJL*, 789, L6, doi: [10.1088/2041-8205/789/1/L6](https://doi.org/10.1088/2041-8205/789/1/L6)
- Thompson, R. C. 1982, *Radiation Research*, 90, 1. <http://www.jstor.org/stable/3575792>
- Tsujimoto, T., Yokoyama, T., & Bekki, K. 2017, *ApJL*, 835, L3, doi: [10.3847/2041-8213/835/1/L3](https://doi.org/10.3847/2041-8213/835/1/L3)
- van der Walt, S., Colbert, S. C., & Varoquaux, G. 2011, *Computing in Science and Engineering*, 13, 22, doi: [10.1109/MCSE.2011.37](https://doi.org/10.1109/MCSE.2011.37)
- Vassh, N., Mumpower, M. R., McLaughlin, G. C., Sprouse, T. M., & Surman, R. 2020, *ApJ*, 896, 28, doi: [10.3847/1538-4357/ab91a9](https://doi.org/10.3847/1538-4357/ab91a9)
- Vassh, N., Vogt, R., Surman, R., et al. 2019, *Journal of Physics G Nuclear Physics*, 46, 065202, doi: [10.1088/1361-6471/ab0bea](https://doi.org/10.1088/1361-6471/ab0bea)
- Vockenhuber, C., Casacuberta, N., Christl, M., & Synal, H.-A. 2015, *Nuclear Instruments and Methods in Physics Research B*, 361, 445, doi: [10.1016/j.nimb.2015.01.061](https://doi.org/10.1016/j.nimb.2015.01.061)
- Vockenhuber, C., Oberli, F., Bichler, M., et al. 2004, *PhRvL*, 93, 172501, doi: [10.1103/PhysRevLett.93.172501](https://doi.org/10.1103/PhysRevLett.93.172501)
- Vockenhuber, C., Feldstein, C., Paul, M., et al. 2004, *New Astronomy Reviews*, 48, 161
- Wallner, A., Faestermann, T., Feige, J., et al. 2015, *Nature Communications*, 6, 5956, doi: [10.1038/ncomms6956](https://doi.org/10.1038/ncomms6956)
- Wallner, A., et al. 2016, *Nature*, 532, 69, doi: [10.1103/PhysRevLett.125.031101](https://doi.org/10.1103/PhysRevLett.125.031101)
- Wallner, A., Feige, J., Fifield, L. K., et al. 2020, *Proceedings of the National Academy of Science*, 117, 21873, doi: [10.1073/pnas.1916769117](https://doi.org/10.1073/pnas.1916769117)
- Wallner, C., Faestermann, T., Gerstmann, U., et al. 2004, *NewAR*, 48, 145, doi: [10.1016/j.newar.2003.11.020](https://doi.org/10.1016/j.newar.2003.11.020)
- Wanajo, S. 2006, *ApJL*, 650, L79, doi: [10.1086/508568](https://doi.org/10.1086/508568)
- . 2013, *ApJL*, 770, L22, doi: [10.1088/2041-8205/770/2/L22](https://doi.org/10.1088/2041-8205/770/2/L22)
- Wanajo, S., Kajino, T., Mathews, G. J., & Otsuki, K. 2001, *ApJ*, 554, 578, doi: [10.1086/321339](https://doi.org/10.1086/321339)
- Wanajo, S., Sekiguchi, Y., Nishimura, N., et al. 2014, *ApJL*, 789, L39, doi: [10.1088/2041-8205/789/2/L39](https://doi.org/10.1088/2041-8205/789/2/L39)
- Wang, X., N3AS Collaboration, Fields, B. D., et al. 2020a, *ApJ*, 893, 92, doi: [10.3847/1538-4357/ab7ffd](https://doi.org/10.3847/1538-4357/ab7ffd)
- Wang, X., N3AS Collaboration, Vassh, N., et al. 2020b, *ApJL*, 903, L3, doi: [10.3847/2041-8213/abbe18](https://doi.org/10.3847/2041-8213/abbe18)
- Wilcken, K., Fifield, L., Barrows, T., Tims, S., & Gladkis, L. 2008, *Nuclear Instruments and Methods in Physics Research Section B: Beam Interactions with Materials and Atoms*, 266, 3614, doi: <https://doi.org/10.1016/j.nimb.2008.06.009>

- Willing, J., Krücken, R., & Meringa, L. 2014, *Hyperfine Interactions*, 225, 253, doi: [10.1007/s10751-013-0906-6](https://doi.org/10.1007/s10751-013-0906-6)
- Winkler, S., Ahmad, I., Golser, R., et al. 2004, *NewAR*, 48, 151, doi: [10.1016/j.newar.2003.11.021](https://doi.org/10.1016/j.newar.2003.11.021)
- Winteler, C., Käppeli, R., Perego, A., et al. 2012, *ApJL*, 750, L22, doi: [10.1088/2041-8205/750/1/L22](https://doi.org/10.1088/2041-8205/750/1/L22)
- Xiong, Z., Sieverding, A., Sen, M., & Qian, Y.-Z. 2020, *ApJ*, 900, 144, doi: [10.3847/1538-4357/abac5e](https://doi.org/10.3847/1538-4357/abac5e)
- Yamazaki, Y., Kajino, T., Mathews, G. J., et al. 2021, arXiv e-prints, arXiv:2102.05891. <https://arxiv.org/abs/2102.05891>
- Yan, Y., Bender, M. L., Brook, E. J., et al. 2019, *Nature*, 574, 663, doi: [10.1038/s41586-019-1692-3](https://doi.org/10.1038/s41586-019-1692-3)
- Yin, X., He, M., Dong, K., et al. 2015, *Nuclear Instruments and Methods in Physics Research B*, 361, 488, doi: [10.1016/j.nimb.2015.07.124](https://doi.org/10.1016/j.nimb.2015.07.124)
- Zhu, Y., Wollaeger, R. T., Vassh, N., et al. 2018, *ApJL*, 863, L23, doi: [10.3847/2041-8213/aad5de](https://doi.org/10.3847/2041-8213/aad5de)
- Zhu, Y. L., Lund, K. A., Barnes, J., et al. 2021, *ApJ*, 906, 94, doi: [10.3847/1538-4357/abc69e](https://doi.org/10.3847/1538-4357/abc69e)